Carbon nanoelectronic heterodyne sensors: A new paradigm for chemical and biological detection

by

Girish Shrinivas Kulkarni

A dissertation submitted in partial fulfillment
of the requirements for the degree of
Doctor of Philosophy
(Electrical Engineering)
in the University of Michigan
2015

Doctoral Committee:

Associate Professor Zhaohui Zhong, Chair
Professor Xudong Fan
Professor Yogesh B. Gianchandani
Professor L. Jay Guo

To my family.

Acknowledgements

First and foremost, I would like to thank my advisor, Professor Zhaohui Zhong for providing me the opportunity to pursue research in his laboratory. He has been an extremely supportive and dedicated research guide and mentor. I first met him in 2008 when he was setting up his laboratory, and his webpage read - 'An empty lab with ample opportunities'. Over these years, I have realized that this positive attitude of his has not only made research fun and enjoyable, but also taught me the importance of patience and perseverance. I also thank my committee members - Professor Xudong Fan, Professor Lingjie (Jay) Guo and Professor Yogesh Gianchandani, for their support and valuable suggestions on my research work.

I was very lucky to have determined and motivated colleagues around me who were full of ideas and always ready to help. I thank all the past and present members of Zhong Lab - Dr. Nanditha Dissanayake, Dr. Chung Chiang Wu, Dr. Seunghyun Lee, Dr. Chang-Hua Liu, Kyunghoon Lee, Che-Hung Liu, Kang Li, Rui Li, Wenzhe Zang and Qi Chen. I would also like to thank my collaborators in Professor Xudong Fan's laboratory for all the interactions and learnings.

The work described in this thesis would not have been complete without the kind and patient support of the staff at Lurie Nanofabrication Facility. I deeply appreciate the help of Matthew Oonk, Gregory Allion, Sandrine Martin, Nadine Wang and Pillar Herrera-Fierro on various tools and processes. I would also like to

thank my colleagues working in the cleanroom, in particular, Dr. Debashish Basu, Dr. Jae Yoong Cho, Dr. Anurag Tripathi, Dr. Trushal Chokshi, Dr. Hyun Kum, Dr. Animesh Banerjee, Dr. Ayan Das, Azadeh Ansari, Cheng Zhang, and Stacey Tang for their mentorship and company.

I am also grateful to the staff at EECS - Melanie Caughey, Deb Swartz, Frances Doman, Steven Pejuan and Beth Stalnaker for their administrative support.

I extend my thanks to my wonderful friends who have made my stay in Michigan a memorable one. A special thanks to Dr. Vikram Thakar, Dr. Siddharth Gaba, Dr. Vikrant Gokhale, Dr. Karthik Reddy, Dev Goyal, Vineet Raichur, Dr. Naveen Gupta, Deepti Joshi, Komal Kampasi, Saniya Deshpande, Patrick Sheridan, Dr. Seow Yuen Yee, Dr. Anne Itsuno, Dr. Alex Kaplan, Heidi Kaplan, Dr. Victor Lee, Ning Gulari and Paul Schmalenberg, for all the fun activities we enjoyed together.

I am grateful to Dr. Rajiv Bapuraj and Sujata aunty, who treated me as part of their family and made sure that I never missed home.

I would like to take this opportunity to acknowledge the selfless service of the doctors and nurses at PGIMER, Chandigarh who treated me and literally gave me a second life. I am deeply indebted to Dr. Subash Varma for his support and care during my treatment and after. Thank you for motivating me to pursue my dreams.

Finally, I would like to express my deepest gratitude to my family who have stood by me through all my personal and professional endeavors. Without the unconditional love, support and encouragement of my parents and my brother and his family, this journey would not have been possible.

Table of Contents

List of Figures

List of Appendices

Appendix

ABSTRACT

In 1959, in his famous talk *'There is plenty of room at the bottom'*, physicist Richard Feynman had envisaged a new era of science where one could build electronic systems which would sense and interact with a world only a few atoms in size. To build such systems we not only need new materials but also new transduction strategies. The hunt for new materials has led us back to ***carbon*** - a material which humans have known since 4000 B.C. Carbon nanotube and graphene-two allotropes of carbon, possess structural, electronic, optical and mechanical properties perfect for building fast, robust and sensitive nano-systems. However, the available sensing technologies are still incapable of high fidelity detection critical for studying nanoscale events in complex environments like ligand-receptor binding, molecular adsorption/desorption, π-π stacking, catalysis, etc.

In this thesis, I first introduce a fundamentally new nanoelectronic sensing technology based on heterodyne mixing to investigate the interaction between charge density fluctuations in a nanoelectronic sensor caused by oscillating dipole moment of molecule and an alternating current drive voltage which excites it. By detecting molecular dipole instead of associated charge, we address the limitations of conventional charge-detection based nanoelectronic sensing techniques.

In particular, using a carbon nanotube heterodyne platform, I demonstrate for the first time, biological detection in high ionic background solutions where

conventional charge-detection based techniques fail due to fundamental Debye screening effect. Next, we report the first graphene nanoelectronic heterodyne vapor sensors which can detect a plethora of vapor molecules with high speed (~ 0.1 second) and high sensitivity (< 1 part per billion) simultaneously; recording orders-of-magnitude improvement over existing nanoelectronic sensors which suffer from fundamental speed-sensitivity tradeoff issue.

Finally, we use heterodyne detection as a probe to quantify the fundamental non-covalent binding interaction between small molecules and graphene by analyzing the real-time molecular desorption kinetics. More importantly, we demonstrate for the first time, electrical tuning of molecule-graphene binding kinetics by electrostatic control of graphene work function signifying the ability to tailor chemical interactions on-demand.

Our work not only lays a foundation for the next-generation of rapid and sensitive nanoelectronic detectors, but also provides an insight into the fundamental molecule-nanomaterial interaction.

Chapter 1

Carbon nanomaterials

1.1 Introduction

Nanotechnology has been a field of intense study over the last two decades since the (re)discovery of carbon nanotubes [1] by Iijima in 1991. Coupled with the progress in top-down patterning methods, bottom-up growth techniques, and high resolution imaging low dimensional nanomaterials like nanotubes, nanowires, graphene and transition metal dichalcogenides have become a playground for fundamental research as well as technological applications. Along with small size, these nanomaterials also possess unique electronic and optical properties due to their exotic lattice band-structures [2-7]. Attributes like high surface-to-volume ratio, high electron mobility, stability in chemically diverse environments, mechanical strength, high thermal conductivity, ability to control chemical composition and compatibility with modern processing technologies makes these nanomaterials ideal candidates for fast, robust and stable miniaturized-electronics, operating in and interacting with the nanoscale world. One such area of application is the study and detection of chemical and biological processes. For such applications, carbon nanomaterials - carbon nanotube (CNT) and graphene are most promising candidates [8,9], since in these nanomaterials all the carbon atoms lie on the surface leading to maximum possible interaction with a molecule in their vicinity. Carbon nanotube can have diameter ~ 1 nanometer, which

makes it a true one-dimensional (1-D) material [10]. Similarly, graphene is just a one-atom thick sheet of carbon, making it an ideal two-dimensional (2-D) material. Such small dimensions are comparable to the size of chemical and biological species; hence these materials have the potential to detect single molecular events as well.

In this chapter, we describe the physical structures and electronic properties of graphene and carbon nanotube. Even though research on carbon nanotubes started prior to the discovery of graphene [11], one can understand and derive the properties of carbon nanotubes from graphene [4]. We therefore start with a brief introduction to graphene and then carbon nanotube (Section 1.2), followed by their electronic properties in Section 1.3. In Section 1.4, we briefly describe the growth process for both these carbon nanomaterials. In Section 1.5, we discuss the behavior of these materials as the channel of a field-effect-transistor (FET) which is the basic building block of any electronic circuit, and also derive the FET current-voltage relationship.

1.2 Graphene and carbon nanotube

Graphene is a sheet of carbon atoms arranged in a hexagonal lattice to form a honeycomb mesh structure [12] as shown in Figure 1-1. Graphene is just one atom thick which makes it a true 2-D structure. If we stack multiple layers of graphene together, we obtain graphite [13] - one of the oldest known carbon allotropes to humans. If we roll up graphene into a cylinder, we obtain a carbon nanotube. We can even obtain the 0-dimensional counterpart, Buckminsterfullerene or C_{60} by rolling up a portion of graphene sheet into a ball. Hence, graphene is the basic element from which other carbon allotropes can be derived as well as their properties understood [4,12]. Carbon nanotubes are hollow cylinders with all atoms on the surface and can have diameters as small as ~1nm. Even though graphene acts as a base for these allotropes of carbon,

C_{60} was discovered first in 1985 at Rice University [14], followed by characterization of carbon nanotubes in 1991 by Sumio Iijima [1]. Graphene was isolated only recently by Andre Geim and Konstantin Novosolev at University of Manchester [11] in 2004.

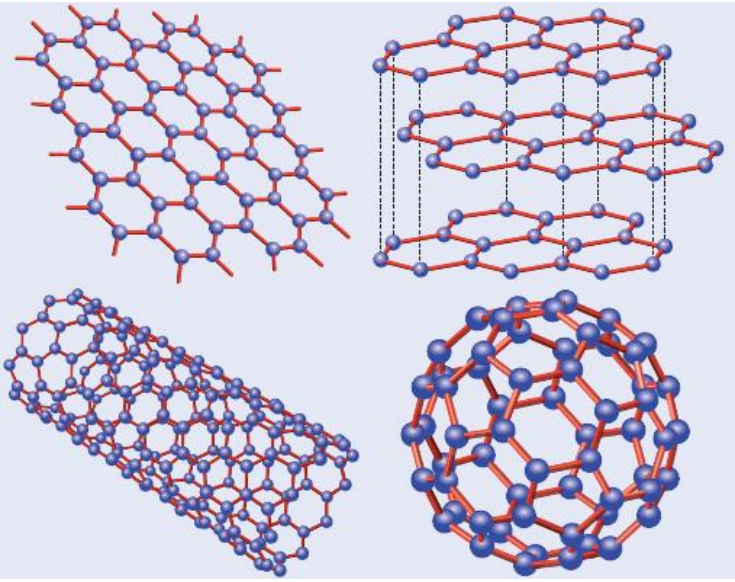

Figure 1-1. Graphene (Top Left), a 2D hexagonal lattice of carbon atoms. It is the basis of the well-known allotropes of carbon – graphite (top right), carbon nanotube (bottom left) and Buckminsterfullerene (bottom right). Reprinted from [12] with permission.

Graphene and carbon nanotubes possesses unique electronic, optical and mechanical properties and are been investigated for a variety of technological applications. Some of these include transparent conductors [15-18], single molecule sensors [19,20], GHz electronics [21,22], DNA sequencing [23,24], ultrathin leak-tight membranes [25], flexible electronics [26-29], broadband photo detectors [30,31], NEMS [32,33] and metrology applications [34].

1.3 Electronic band structure

In graphene, each carbon atom is bonded to three neighboring carbon atoms in an sp^2-hybridized state in the x-y plane (Figure 1-2). This leaves the $2p_Z$ orbital free,

perpendicular to the graphene sheet which combines with the neighboring $2p_Z$ orbitals to form π-orbitals and contribute to the high conductance observed in graphene. The carbon-carbon covalent bond is known to be one of the strongest and gives graphene its mechanical strength.

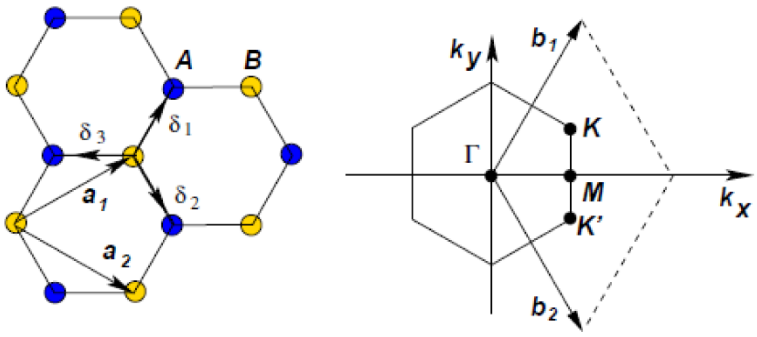

Figure 1-2. (Left) Graphene lattice in real space. The nearest neighbors are marked, $\delta_{i,\ i=1,\ 2,\ 3}$. The lattice vectors are $\vec{a}_1$ and $\vec{a}_2$. (Right) Corresponding Brillouin zone. Dirac cones are located at K and K´ [35]. Reprinted with permission.

The electrical properties of graphene and carbon nanotubes can be understood from the band structure of graphene, which was first calculated by Wallace (1947) using the tight-binding approximation [36]. The resulting energy dispersion relation is presented below,

$$E(k_x, k_y) = \pm t\sqrt{1 + 4\cos^2\frac{k_x a}{2} + 4\cos\frac{k_x a}{2}\cos\frac{k_y a\sqrt{3}}{2}}. \qquad \text{Equation 1-1}$$

Here, t = 2.5 eV is the interaction integral, a = 2.46 Å is the lattice constant of graphene, k_x and k_y are the wave vectors in the x and y directions, respectively. The band structure from this calculation is shown in Figure 1-3a, in which we see that the valence and conduction bands meet at the six points in reciprocal space [35]. However, only two of them are unique, K and K´. Because the conduction and valence bands meet at a point, graphene has no band gap.

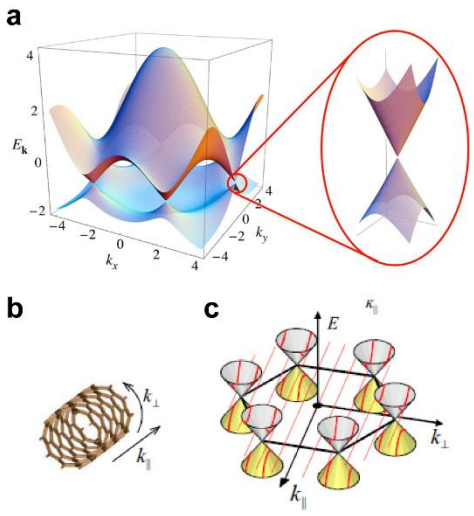

Figure 1-3. **(a)** Energy band structure for graphene plotted with the wave vectors, k_x and k_y. This can be calculated by the tight binding approximation taking into account the nearest neighbors. Reprinted from [35] with permission. **(b)** A carbon nanotube which is obtained by rolling up graphene quantizes the wave states perpendicular to the nanotube axis. **(c)** The allowed electronic states in a nanotube are determined by the intersections between the allowed wave vectors and graphene band structure. Near the Fermi energy, E_F the band structure can be approximated as conical. Adapted from [37], © Ethan Minot, 2004.

If we roll up a graphene sheet, we obtain a carbon nanotube. The real space crystal of graphene can be characterized by the lattice vectors $\vec{a}_1 = \frac{a}{2}(\sqrt{3}, 1)$ and $\vec{a}_2 = \frac{a}{2}(\sqrt{3}, -1)$, where a = 2.46 Å is the lattice constant [10]. Refer to Figure 1-2. Each nanotube is uniquely defined by the chiral vector, $\vec{C}$ that connects the two points on the graphene lattice that are rolled to touch each other when the nanotube is formed as shown in Figure 1-4. A (n, m) nanotube has $\vec{C} = n\vec{a}_1 + m\vec{a}_2$. This also imposes a periodic boundary condition on the lattice vector (Figure 1-3b) so that,

$$\vec{C} \cdot \vec{k} = 0 \; mod \; 2\pi \, . \qquad \text{Equation 1-2}$$

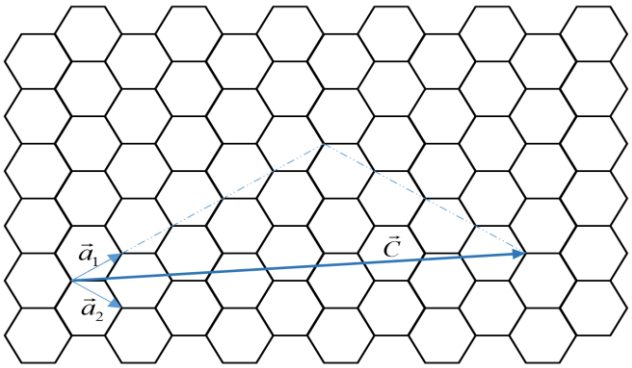

Figure 1-4. Honeycomb lattice of graphene with $\vec{a}_1$and $\vec{a}_2$ lattice vectors. The chiral vector $\vec{C}$ points from the origin to the point which is rolled up to meet the origin. Here, n = 5 and m = 4 so the nanotube is (5, 4) nanotube. Adapted from [10].

The one-dimensional energy band of a nanotube are given by cuts made through the two-dimensional band structure of graphene, as shown in Figure 1-3c. If the allowed k vector passes through the K point, then we have a 1-D metallic tube with linear band structure like graphene. In all other cases, we get a semiconducting nanotube with a band gap. From Equation 1-2, we can see that the nanotube will be metallic if the k vector of the K point satisfies the condition:

$$\vec{C} \cdot \vec{k} = (n\vec{a}_1 + m\vec{a}_2) \cdot \left(\frac{2\pi}{a\sqrt{3}}, \frac{2\pi}{3a}\right) = 0 \; mod \; 2\pi$$

$$\vec{C} \cdot \vec{k} = 2\pi\left(\frac{2}{3}n + \frac{1}{3}m\right) = 0 \; mod \; 2\pi \; . \qquad \text{Equation 1-3}$$

This is equivalent to 2n + m = 0 mod 3, or, equivalently (since 3n = 0 mod 3) n − m = 0 mod 3. Assuming that all (n, m) combinations are equally likely, we therefore expect 2/3 of nanotubes to be semiconducting, and 1/3 to be metallic. We will discuss the electronic properties of carbon nanotube and graphene in Section 1.5. One of the challenges in the nanotube community has been to control the growth process to selectively get semiconducting or metallic tubes, however, this has still not been achieved.

1.4 Carbon nanomaterial growth

1.4.1 Carbon nanotube

Carbon nanotubes can be grown using a number of different methods. The first characterization of carbon nanotubes by Iijima was done on tubes grown using the arc discharge method [38] (Figure 1-5a). Soon after, researchers demonstrated that carbon nanotubes can be grown using laser ablation [39] and chemical vapor deposition [40,41] (Figure 1-5b, c) also. However, amongst these, chemical vapor deposition (CVD) with catalyst-assistance is most commonly used method. CVD growth is known to produce low defect nanotubes. The mechanism in CVD growth is a thermal dehydrogenation reaction. At high temperature, the decomposition of a carbon containing gas produces carbon which dissolves into the metal catalysts (Fe, Co, Ni, Cu or Mo). Once the catalyst reaches the carbon-solubility limit, the dissolved carbon precipitates out and forms a crystallized CNT. This precipitation process may occur either at the top or bottom of the catalyst depending on the catalyst-substrate interaction [42]. Hence, by controlling the CVD growth condition, substrate, carbon precursor etc. one can tune the nanotube growth to obtain single walled, double walled or multi-walled nanotubes; aligned individual tubes [43] or a nanotube network [44,45]; horizontal or vertical growth [46]; and nanotubes with varying lengths some as long as centimeters [47] (see Figure 1-6).

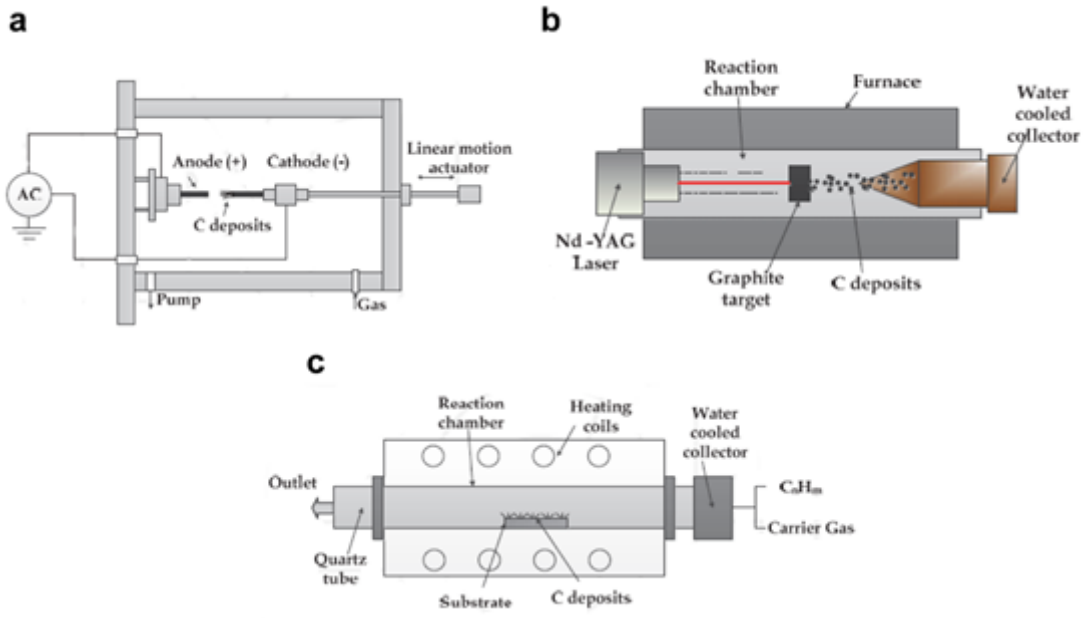

Figure 1-5. Basic setup of carbon nanotube growth process using **(a)** arc discharge method **(b)** laser ablation and **(c)** chemical vapor deposition. © S. Yellampalli, 2011 (InTech). Adapted from [48].

The biggest advantage of CVD growth is that one can grow nanotubes on a silicon substrate and carry out all the normal lithography steps on the same substrate to build electronic devices [41]. In this thesis, we use CVD grown carbon nanotubes using ethanol precursor as our carbon source. The growth condition is discussed in detail in Appendix A.

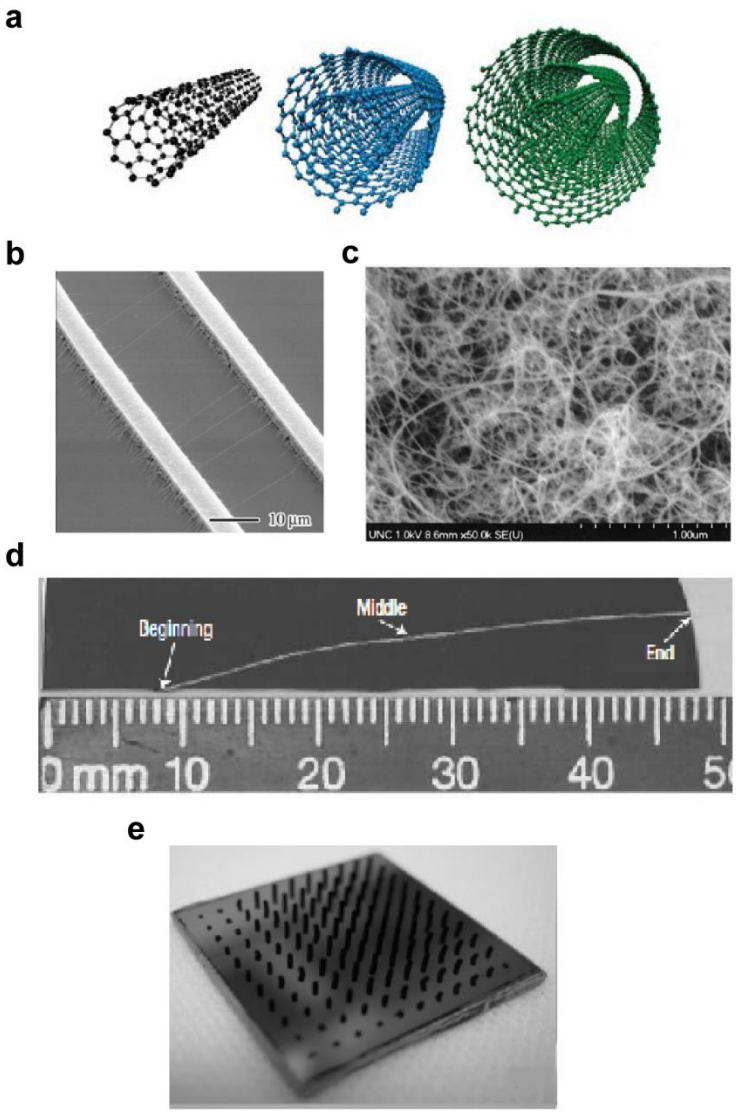

Figure 1-6. **(a)** Diagrammatic representation of a single walled, double walled and multi walled carbon nanotube. **(b)** Aligned growth of single walled nanotubes across two pillars [43]. **(c)** CVD growth of a carbon nanotube network [45]. **(d)** Ultra-long carbon nanotubes > 4cm grown on a silicon dioxide substrate [47]. **(e)** Vertical growth of carbon nanotubes [46]. Reprinted from [43, 45-47] with permission.

1.4.2 Graphene

Graphene was first synthesized [11] using what is now famous as ‘scotch-tape’ method, wherein a highly oriented pyrolytic graphite (HOPG) crystal was repeatedly peeled till only one layer of graphite i.e. graphene was left behind (Figure 1-7a, b). This

method is also called the mechanical exfoliation process which gives crystalline and defect free graphene sheets. Infact, during the exfoliation we not only obtain single layer graphene sheets, but also bilayer and multiple layer graphene. The drawbacks of exfoliation are that the samples are distributed randomly, the yield is very low and the graphene size obtained are 10-20 μm only. This makes it extremely hard to process these samples using conventional photolithography and the method is not scalable.

Graphene can also be grown epitaxially (Figure 1-7c, d) on insulating silicon carbide (SiC) substrate [49,50] at very high temperature ~1200-1600 C. The principle behind the growth is that sublimation rate of silicon is higher than that of carbon; thus excess carbon atoms are left behind on the surface and rearrange to form graphene. The third method of graphene growth is through chemical vapor deposition (CVD) on metal substrates [51,52] at high temperatures (Figure 1-7e, f). This is the most commonly used method as not only one can grow wafer size graphene sheets but also control the growth parameters to get single layer [51], bilayer [53] or multilayer graphene sheets [52]. Moreover, once the underlying metal layer is etched the graphene sheet can be solution-transferred onto any surface. In the CVD method, graphene is synthesized by injecting carbon-containing gas and hydrogen into a furnace (~1000°C) to interact with the metals, e.g., Ni, Cu, Ru and Ir. The most commonly used metal is copper as graphene growth on copper is uniform >95% coverage which is suitable for scalable processing. As the temperature is raised, first the copper domain sizes increase after which the carbon atoms from the precursor gas dissolves into copper. When temperature is lowered during the cooling phase, carbon atoms which diffuse out of copper settle into graphene honeycomb structure, which happens to be

thermodynamically the most stable state [51]. The low solubility of carbon in copper ensures that the amount of carbon available is sufficient for single or bilayer graphene growth. In this thesis, we use graphene grown on copper foils using the CVD technique with methane as the precursor. The growth parameters are discussed in Appendix B.

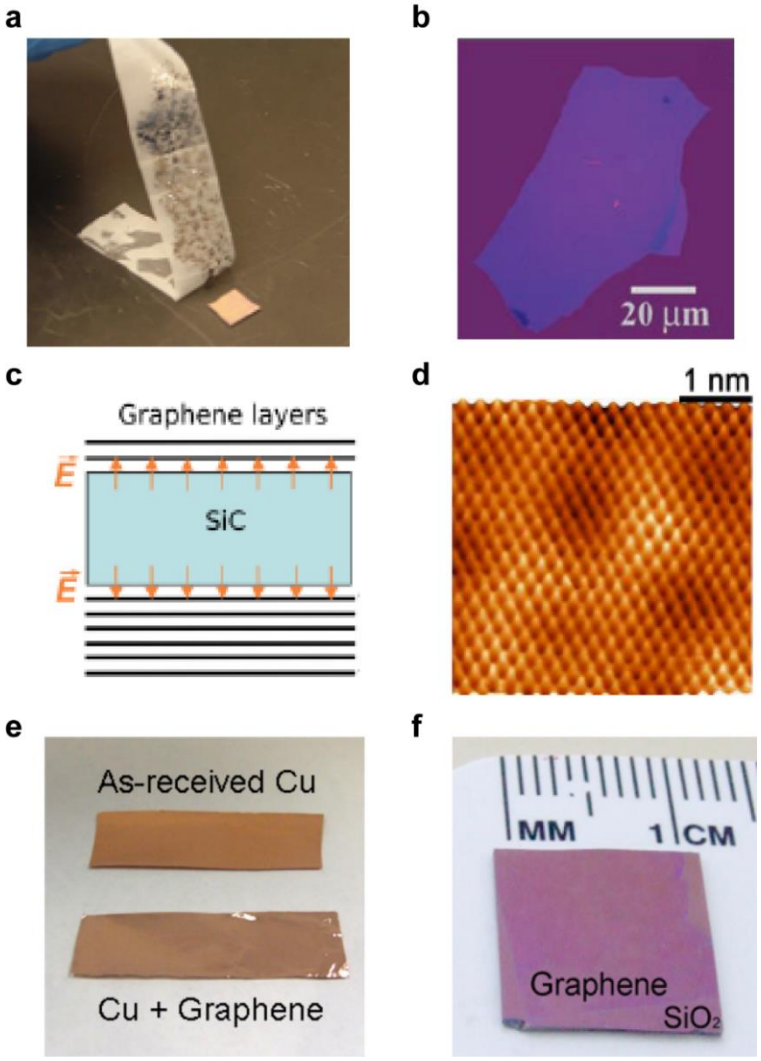

Figure 1-7 **(a)** Mechanical exfoliation of graphene using a scotch tape. **(b)** Single layer graphene left behind on a silicon dioxide substrate after exfoliation process [11]. **(c)** Epitaxial growth process on silicon carbide. **(d)** Scanning tunneling image showing the hexagonal pattern of graphene on SiC substrate [50]. **(e)** Chemical vapor deposition (CVD) grown graphene on a copper foil. A single layer of graphene on copper foil gives it a shiny look. **(f)** CVD graphene solution transferred onto a silicon dioxide substrate after copper etching. Size of graphene sheet is around 1cm × 1cm [51]. Reprinted from [11, 50, 51] with permission.

1.5 Carbon nanoelectronic devices

The unique band structure of graphene and carbon nanotube provides it with extraordinary electrical properties. In graphene, near the K points, the energy varies linearly in k, and since the effective mass of electrons/holes in a lattice is given by the curvature of band structure near the conduction/valence band edge, graphene has a zero effective mass for electrons and holes – an unusual property [35]. Theoretically, Fermi velocity of charge carriers in graphene is 10^6 m/s, which is 1/300th the speed of light. Experimentally, researchers have demonstrated charge carrier mobility values in graphene as high as 200,000 $cm^2V^{-1}s^{-1}$ [54]. The band structure of carbon nanotubes on the other hand, reveals that it can have zero band gap (metallic) or can be semiconducting with small (~10 meV) to larger band gaps, E_g. Generally, $E_g \sim 0.7\text{eV}/\boldsymbol{d}$, where $\boldsymbol{d}$ is the diameter of the carbon nanotube in nanometers [10].

Such properties make both these carbon materials promising candidates for replacing silicon in next generation nanoscale electronic devices for analog and digital applications. The basic building blocks for such devices is a transistor. In a transistor, one terminal (gate) is used to control the flow of charge carriers in the channel between the other two terminals – source and drain, as shown in Figure 1-8a. The first nanotube transistor was fabricated by Tans et al [55] in 1998, whereas graphene transistors were demonstrated in 2004 [11]. A voltage applied at the gate can tune the Fermi level of the channel from valence band to conduction band. Unlike silicon FETs, carbon materials are ambipolar in nature, i.e., one can operate in the hole-dominant region (p-type) or the electron-dominant region (n-type). In case of a semiconducting nanotube, the Fermi level can be adjusted to be within the band gap, at which point the conductance goes to zero (Figure 1-8b).

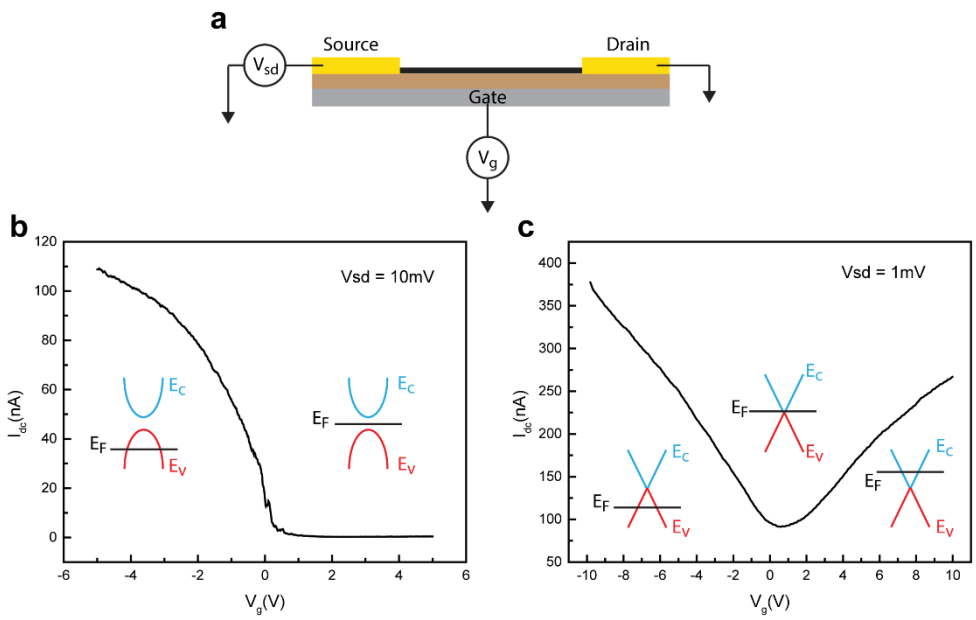

Figure 1-8. **(a)** General schematic of a field effect transistor with source, drain and gate terminals. The carbon based channel is shown in black. **(b)** Current-voltage relation, $I_{dc} - V_g$ for a semiconducting carbon nanotube FET with the Fermi levels depicted corresponding to on and off state. **(c)** Current-voltage relation, $I_{dc} - V_g$ for a graphene FET with the Fermi level alignment shown for p-type, near Dirac point and n-type operation. The conduction bands (blue) and valence bands (red) are also depicted.

Figure 1-8c shows a typical current-voltage characteristic for a back-gated graphene field-effect-transistor. The relative position of the Fermi level for each operating point is also shown. At negative gate bias, we operate in the p-type region where the carriers are holes and as we move to positive gate biases, we pass through the K point (also known as Dirac point) to enter n-type region where carriers are electrons. This picture holds true for metallic CNT's also. From the discussion in Section 1.3, one would expect that in graphene (or carbon nanotube), the transition from hole transport to electron transport should happen exactly at zero gate bias. However, experimentally this is rarely observed in measurements conducted in ambient

conditions. The Dirac point in most instances is shifted to positive gate voltages and is attributed to doping by atmospheric oxygen, presence of a layer of water dipoles in air or doping by the substrate [56]. In vacuum and with a suspended device, Dirac point close to zero volts can be obtained due to removal of water and substrate effects [54]. In the next section, we will derive the basic transistor current-voltage ($I-V$) relation for carbon nanomaterial based field-effect-transistors.

1.5.1 Carbon nanotube field-effect-transistor

It is easier to start with a carbon nanotube as it is a one-dimensional problem. We consider a p-type semiconducting nanotube (Figure 1-8b). The voltage applied at the back gate controls the number of charge carriers in the channel by adjusting the Fermi level. The voltage difference between the source and drain, V_{sd} causes a current to flow between them for $V_g < 0$. Let us assume that this voltage falls linearly across the channel, hence at a particular point, x along the channel, the voltage is $V(x)$. For a 1-D p-type carbon nanotube, the back gate induces a charge (hole) density per unit length, $n(x)$ in the channel given by

$$n(x) = \frac{C_g'\left(|V_g|+V(x)\right)}{e}. \qquad \text{Equation 1-4}$$

Here, C_g' is the gate capacitance per unit length. This is easy to understand if we consider the nanotube-gate capacitor; a positive voltage at source terminal will add more charges onto the capacitor. We are assuming that the turn-off voltage or threshold voltage is zero in the above case. However, this is rarely true as experimentally the nanotube (or graphene) is always found to be inherently (p-) doped which has been attributed to oxygen and water dipoles in the ambient atmosphere. We can treat initially

doped channel by adjusting for threshold voltage, V_{th} as $V_{g0} = |V_g - V_{th}|$ where V_{g0} is gate-overdrive voltage. The total charge in the channel per unit length is

$$q(x) = n(x)e \ . \qquad \text{Equation 1-5}$$

Using ohm's law, current density ***j*** in 1-D can be related to conductivity $\sigma(x)$ through the electric field $E(x)$ given by:

$$j(x) = \sigma(x)E(x) = \mu n(x)e\left[-\frac{dV(x)}{dx}\right], \qquad \text{Equation 1-6}$$

where μ is the hole mobility. Now, the total current flowing through the nanotube is equal to j since this is a 1D problem. Hence,

$$I = -\mu n(x)e\left[\frac{dV(x)}{dx}\right] . \qquad \text{Equation 1-7}$$

Using, Equation 1-4, and integrating along the length x = 0 to L where voltage changes from $V = V$ to 0, we have

$$I\int_0^L dx = -\mu\int_0^L C_g'\left(V_{g0} + V(x)\right)\frac{dV(x)}{dx}dx$$

$$IL = -\mu\int_V^0 C_g'\left(V_{g0} + V(x)\right)dV(x) \qquad \text{Equation 1-8}$$

$$I = \frac{\mu C_g'}{L}\left(V_{g0} + \frac{1}{2}V\right)V \ . \qquad \text{Equation 1-9}$$

We can follow similar analysis to derive the *I*-*V* relation for an n-type carbon nanotube FET, where we would be operating at positive gate voltages, hence $n(x)e = -C_g'\left(V_{g0} - V(x)\right)$ which would yield $I = \frac{\mu C_g'}{L}\left(V_{g0} - \frac{1}{2}V\right)V$.

1.5.2 Graphene field-effect-transistor

For a graphene transistor, again we can follow the above derivation, however, since graphene is 2D sheet we need to talk in terms of charge per unit area. Moreover, there are some interesting aspects of graphene. One would expect that at K point

conductance should fall to zero as the density of states is exactly zero. This is never observed experimentally in graphene and has been a topic of intense research. The potential fluctuations due to the substrate leads to electron and hole puddles in graphene and gives rise to a non-zero residual carrier density, n_0 [57]. This is accounted for by modifying the charge density equation as

$$n_{total} = \sqrt{n(x)^2 + n_0^2}\,, \qquad \text{Equation 1-10}$$

where $n(x)e = C'_{gA}\left(V_{g0} + V(x)\right)$ and C'_{gA} is the capacitance per unit area following similar argument as in section 1.5.1. In graphene, the current, I is related to current density, j as $I = j \cdot W$ where W is the graphene channel width. Hence, Equation 1-7 can be modified as:

$$I = -\mu W\sqrt{n(x)^2 + n_0^2}\, e\,\frac{dV(x)}{dx} \qquad \text{Equation 1-11}$$

$$I = \frac{\mu We}{L}\int_0^V \sqrt{n_0^2 + \left(\frac{C'_{gA}\left(V_{g0}+V(x)\right)}{e}\right)^2}\, dV(x)\,. \qquad \text{Equation 1-12}$$

This equation takes care of the ambipolar nature of a symmetric graphene ($\mu_h = \mu_e$) device. It would be much more helpful to have a simple analytical form for Equation 1-12. If we have clean samples and operate far enough from the Dirac point such that $n(x) \gg n_0$, then the above equation can be simplified to

$$I = \frac{\mu W}{L}\int_0^V C'_{gA}\left(V_{g0} + V(x)\right) dV(x) \qquad \text{Equation 1-13}$$

$$I = \frac{\mu W C'_{gA}}{L}\left(V_{g0} + \frac{1}{2}V\right)V\,. \qquad \text{Equation 1-14}$$

From the above discussion, we can write down a general equation considering the total capacitance a device, C_g which is valid for both CNT ($C_g = C'_g L$) and graphene ($C_g = C'_{gA} WL$),

$$I = \frac{\mu}{L^2} C_g \left(V_{g0} + \frac{1}{2}V\right) V \ . \qquad \text{Equation 1-15}$$

We will refer to Equation 1-9 and Equation 1-14 during the discussion on carbon nanotube and graphene based sensors in the following chapters, where we model the response of these sensors to molecules in the surrounding environment.

1.6 Summary and Outline

In this chapter, we presented the structural and electronic properties of carbon based nanomaterials. Their small size, high surface-to-volume ratio and high carrier mobility make them ideal candidates chemical and biological sensing applications. In chapter 2, we provide an overview of nanoelectronic sensors in literature. A lot of work has been done towards building robust electronic devices from nanomaterials like nanowires, nanotubes and graphene; however, the available sensing technologies are still incapable of simultaneous high-speed and high-sensitivity detection. We will discuss these limitations in chapter 2 as well. In chapter 3, we introduce a fundamentally new sensing mechanism based on the principle of heterodyne mixing to address the challenges of conventional sensing technologies. Chapter 4 discusses the application of our heterodyne mixing technique for biological detection in high ionic strength solutions using carbon nanotube field effect transistors. In chapter 5, we discuss the development and implementation of the first graphene heterodyne vapor sensors for rapid and sensitive chemical vapor analysis. Heterodyne sensing is a versatile tool and can also be used as a probe to study molecule-nanomaterial interaction dynamics. This is discussed in detail in chapter 6, where we demonstrate the first experimental estimation of binding energies of various polar vapor molecules on graphene.

References

[1] S. Iijima, Nature **354**, 56 (1991).
[2] P. L. McEuen, Phys. World **13**, 31 (2000).
[3] W. Lu and C. M. Lieber, Nature Materials **6**, 841 (2007).
[4] A. K. Geim and K. S. Novoselov, Nature Materials **6**, 183 (2007).
[5] R. H. Baughman, A. A. Zakhidov, and W. A. de Heer, Science **297**, 787 (2002).
[6] A. K. Geim and P. Kim, Scientific American **298**, 90 (2008).
[7] Q. H. Wang, K. Kalantar-Zadeh, A. Kis, J. N. Coleman, and M. S. Strano, Nat. Nanotechnol. **7**, 699 (2012).
[8] S. E. Moulton, A. I. Minett, and G. G. Wallace, Sensor Letters **3**, 183 (2005).
[9] Y. Y. Shao, J. Wang, H. Wu, J. Liu, I. A. Aksay, and Y. H. Lin, Electroanalysis **22**, 1027 (2010).
[10] G. D. R. Saito, Mildred S. Dresselhaus, *Physical properites of carbon nanotube* (Imperial College Press, 1998).
[11] K. S. Novoselov, A. K. Geim, S. V. Morozov, D. Jiang, Y. Zhang, S. V. Dubonos, I. V. Grigorieva, and A. A. Firsov, Science **306**, 666 (2004).
[12] A. C. Neto, F. Guinea, and N. M. R. Peres, Physics World **19**, 33 (2006).
[13] B. Partoens and F. M. Peeters, Physical Review B **74** (2006).
[14] H. W. Kroto, J. R. Heath, S. C. Obrien, R. F. Curl, and R. E. Smalley, Nature **318**, 162 (1985).
[15] Z. C. Wu *et al.*, Science **305**, 1273 (2004).
[16] S. Bae *et al.*, Nature Nanotechnology **5**, 574 (2010).
[17] X. Wang, L. J. Zhi, and K. Mullen, Nano Letters **8**, 323 (2008).
[18] X. S. Li, Y. W. Zhu, W. W. Cai, M. Borysiak, B. Y. Han, D. Chen, R. D. Piner, L. Colombo, and R. S. Ruoff, Nano Letters **9**, 4359 (2009).
[19] K. Besteman, J. O. Lee, F. G. M. Wiertz, H. A. Heering, and C. Dekker, Nano Letters **3**, 727 (2003).
[20] F. Schedin, A. K. Geim, S. V. Morozov, E. W. Hill, P. Blake, M. I. Katsnelson, and K. S. Novoselov, Nature Materials **6**, 652 (2007).
[21] S. D. Li, Z. Yu, S. F. Yen, W. C. Tang, and P. J. Burke, Nano Letters **4**, 753 (2004).
[22] Y. M. Lin, C. Dimitrakopoulos, K. A. Jenkins, D. B. Farmer, H. Y. Chiu, A. Grill, and P. Avouris, Science **327**, 662 (2010).
[23] S. K. Min, W. Y. Kim, Y. Cho, and K. S. Kim, Nature Nanotechnology **6**, 162 (2011).
[24] H. W. C. Postma, Nano Letters **10**, 420 (2010).
[25] R. R. Nair, H. A. Wu, P. N. Jayaram, I. V. Grigorieva, and A. K. Geim, Science **335**, 442 (2012).
[26] E. Artukovic, M. Kaempgen, D. S. Hecht, S. Roth, and G. GrUner, Nano Letters **5**, 757 (2005).
[27] T. Takenobu, T. Takahashi, T. Kanbara, K. Tsukagoshi, Y. Aoyagi, and Y. Iwasa, Applied Physics Letters **88** (2006).
[28] C. Sire, F. Ardiaca, S. Lepilliet, J. W. T. Seo, M. C. Hersam, G. Darnbrine, H. Happy, and V. Derycke, Nano Letters **12**, 1184 (2012).
[29] G. Eda, G. Fanchini, and M. Chhowalla, Nature Nanotechnology **3**, 270 (2008).
[30] P. Avouris, M. Freitag, and V. Perebeinos, Nature Photonics **2**, 341 (2008).

[31] T. Mueller, F. N. A. Xia, and P. Avouris, Nature Photonics **4**, 297 (2010).
[32] V. Sazonova, Y. Yaish, H. Ustunel, D. Roundy, T. A. Arias, and P. L. McEuen, Nature **431**, 284 (2004).
[33] J. S. Bunch, A. M. van der Zande, S. S. Verbridge, I. W. Frank, D. M. Tanenbaum, J. M. Parpia, H. G. Craighead, and P. L. McEuen, Science **315**, 490 (2007).
[34] A. Tzalenchuk *et al.*, Nature Nanotechnology **5**, 186 (2010).
[35] A. H. Castro Neto, F. Guinea, N. M. R. Peres, K. S. Novoselov, and A. K. Geim, Reviews of Modern Physics **81**, 109 (2009).
[36] P. R. Wallace, Physical Review **71**, 622 (1947).
[37] E. Minot, Cornell University, 2004.
[38] C. Journet, W. K. Maser, P. Bernier, A. Loiseau, M. L. delaChapelle, S. Lefrant, P. Deniard, R. Lee, and J. E. Fischer, Nature **388**, 756 (1997).
[39] M. Yudasaka, T. Komatsu, T. Ichihashi, and S. Iijima, Chemical Physics Letters **278**, 102 (1997).
[40] J. Kong, A. M. Cassell, and H. J. Dai, Chemical Physics Letters **292**, 567 (1998).
[41] J. Kong, H. T. Soh, A. M. Cassell, C. F. Quate, and H. J. Dai, Nature **395**, 878 (1998).
[42] M. Kumar and Y. Ando, Journal of Nanoscience and Nanotechnology **10**, 3739 (2010).
[43] Y. G. Zhang *et al.*, Applied Physics Letters **79**, 3155 (2001).
[44] J. M. Ting and C. C. Chang, Applied Physics Letters **80**, 324 (2002).
[45] D. K. Smith, D. C. Lee, and B. A. Korgel, Chemistry of Materials **18**, 3356 (2006).
[46] O. Yaglioglu, R. Martens, A. J. Hart, and A. H. Slocum, Advanced Materials **20**, 357 (2008).
[47] L. X. Zheng *et al.*, Nature Materials **3**, 673 (2004).
[48] S. Yellampalli, *Carbon Nanotubes - Synthesis, Characterization, Applications* (InTech, 2011).
[49] C. Berger *et al.*, Journal of Physical Chemistry B **108**, 19912 (2004).
[50] P. N. First, W. A. de Heer, T. Seyller, C. Berger, J. A. Stroscio, and J. S. Moon, Mrs Bulletin **35**, 296 (2010).
[51] X. S. Li *et al.*, Science **324**, 1312 (2009).
[52] K. S. Kim *et al.*, Nature **457**, 706 (2009).
[53] S. Lee, K. Lee, and Z. H. Zhong, Nano Letters **10**, 4702 (2010).
[54] K. I. Bolotin, K. J. Sikes, Z. Jiang, M. Klima, G. Fudenberg, J. Hone, P. Kim, and H. L. Stormer, Solid State Communications **146**, 351 (2008).
[55] S. J. Tans, A. R. M. Verschueren, and C. Dekker, Nature **393**, 49 (1998).
[56] M. Lafkioti, B. Krauss, T. Lohmann, U. Zschieschang, H. Klauk, K. von Klitzing, and J. H. Smet, Nano Letters **10**, 1149 (2010).
[57] S. Das Sarma, S. Adam, E. H. Hwang, and E. Rossi, Reviews of Modern Physics **83**, 407 (2011).

Chapter 2

Nanoelectronic sensors for chemical and biological detection

2.1 Introduction

Fast and reliable monitoring of chemicals and biomolecules is of utmost importance for a number of application like defense and homeland security [1,2], industrial and environmental monitoring [3,4], genomics [5], clinical screening and medical diagnosis [6-8], drug delivery [9] to name a few. The necessity to accurately monitor low concentrations of molecules in these applications, in turn places stringent requirements on speed, sensitivity, size and stability of chemical and biological sensors [10-13]. These requirements become even more critical when we move from a laboratory environment to real-time on-field applications. One class of materials which fulfil the above criteria are the 1-D and 2-D nanoscale materials like carbon nanotubes, nanowires, graphene and transition metal dichalcogenides. Consequently, a lot of exciting research has been carried out using these nanoelectronic platforms. In this chapter, we first present a brief overview of chemical and biological sensors in Section 2.2. Next, we discuss the previous work done in the area of nanoelectronic chemical sensors in Section 2.3 and nanoelectronic biological sensors in Section 2.4. In these sections we also present the key shortcomings of conventional state-of-art sensors. Finally, in Section 2.5 we introduce our approach to address the challenges of current sensing technologies, the details of which are discussed in rest of the thesis.

2.2 Overview of chemical and biological sensors

Most of the common chemical and biological sensors found in literature can be categorized broadly into: (1) optical [14-18], (2) electromechanical [19-23], and (3) electrical [24-29] sensors. Optical sensors currently outperform the other two categories of nanosensors in terms of sensitivity and reliability. However, most of the optical detection techniques whether based on surface plasmon [30] or fluorescence/dye labeling [16], require elaborate setup, and are time-consuming and complex. For example, in most biological applications multiple steps are needed starting with sample purification, fluorescent-dye tagging, followed by optical detection and then electrical amplification of the signal. Even practicality of techniques like surface plasmon are in question when one is monitoring only a few molecules which adsorb/desorb quickly from the surface for example, in gas sensing. Moreover, optical detection is prohibitive especially for real-time on-site operation because of high power, size and cost requirements.

Electromechanical and electrical devices are viable alternatives for low-cost and low-power chemical and biological sensing. Electromechanical sensors generally involve a cantilever or doubly-clamped type resonator controlled by an electronic circuit [19,22,23]. Any mechanical perturbation due to the presence of molecules on the sensor, causes a shift in the resonance frequency, which can be electrically monitored to detect the adsorbed species. Micro-fabricated electromechanical systems (MEMS) are available commercially, however, MEMS devices are single-use devices and require significant volumes of analyte to be injected leading to poor sensitivity. Similarly, label-free electrical sensors which directly convert chemical signals to electrical ones, e.g., amperometric sensors [29], solid state conductance sensors [31]

and ion-selective field-effective-transistor sensors [32] have demonstrated successful detection of small molecules and ions, but still suffer from low sensitivity (~100s of ppm) due to their large device footprint.

Here, nanosensors play an important role in addressing the issue of low sensitivity while at the same time providing low-cost, low-power and versatile detection capabilities. At the molecular level, most biological and chemical species like viruses, proteins, DNA and volatile chemicals are typically 0.2-50 nm in size. Nanomaterials like nanotubes (diameter ~1 nm), nanowires (diameter~10-20 nm), graphene (one-atom thick, nanoribbon width~5-20 nm) and molybdenum disulphide (MoS_2, thickness~0.8 nm) compare well with the length scales of these small molecules and therefore, can act as extremely sensitive chemical and biological probes.

Nano-electromechanical (NEM) sensors based on these nanomaterials have shown to possess extremely high sensitivities in gas phase sensing or dry state mass sensing [20,23]. However, high sensitivities (injected mass ~ nanograms) are achieved only through a coating of chemoselective polymer [33], which makes the sensor selective towards just one or two chemicals. Moreover, coating a suspended nanostructure is also a complex task which adds to device failure rates.

Nanoelectronic sensors on the other hand, are more practical for studying chemical and biological processes at the molecular level, due to their versatility, robustness, stability, ease-of-fabrication and integration with existing technologies. A lot of exciting research has been conducted on nanoelectronic sensors. Researchers have demonstrated parts per billion (ppb) sensitivities for gas molecules [34,35], and femto-molar [36] and single-molecule sensitivities [27,37] for biological species. A

wide range of molecules like proteins [28], viruses [37], organic [38] and inorganic molecules [39], ions [27], polar and non-polar analytes [40] etc. have been successfully detected on nanoelectronic platforms. Most of these devices are configured as field-effect-transistor structures (Figure 1.8). An interaction between the molecule and the nanomaterial leads to a change in the electrochemical potential or conductance of the nanosensor which can be monitored in real-time for sensing applications. This change can happen through a charge transfer to the nanomaterial or through a local capacitive gating effect [41]. In the following section, we discuss some of the key research conducted in this area.

2.3 Nanoelectronic chemical sensors

2.3.1 Previous work

The first gas sensing experiment on carbon nanotubes (CNT) was conducted by Kong et al [42] in 2000, who showed that NO_2 and NH_3 molecules can cause a shift in the threshold voltage of a CNT-FET as shown in Figure 2-1a. NO_2 shifted the $I-V$ characteristics to more positive voltages indicating p-doping, whereas NH_3 shifted the response curves to negative gate biases indication n-doping. NO_2 is a strong oxidizer while NH_3, with its lone electron pair is an electron donor; hence these effects were attributed to their ability to accept/donate electrons from/to the nanotube, respectively. This work was followed by other groups who showed detection of different gas analytes like DMMP [35], CO_2 [43], oxygen [44], amine-compounds [38] on CNT FETs and attributed it to charge transfer. Another important study in vapor sensing was conducted by Snow et al. using a capacitive structure [40]. In their work, carbon nanotube network was deposited on a thermal oxide on silicon substrate. The nanotube network formed

one plate of the capacitor as well as the active element with the thermal oxide acting as the dielectric. By sensing the change in capacitance, they showed detection of a large range of analytes. The effect was attributed to the molecular dipoles changing the permittivity of the dielectric leading to a change in the capacitance.

Nanowires have also been used to detect gas species. Zinc oxide [45], tin oxide [46], indium oxide [47] and silicon nanowire [48] FETs have been utilized to detect a variety of gases and chemicals like oxygen, ethanol, hexane and ammonia. McAlpine et al. prepared silicon nanowire FETs on flexible plastic substrates and demonstrated parts per billion detection limits for NO_2. Similar work has been carried out on graphene based FETs for vapor sensing applications. Schedin et al. [49] have shown extremely sensitive measurements with single gas molecule detection capabilities (Figure 2-1b). In their work, graphene hall bar structures were used to measure the hall resistance in vacuum and under a 10 T magnetic field to detect vapor molecules. Under these conditions, they were able to record single gas molecule adsorption and desorption (at 50° C). Recently, Shur et al [50] used low frequency noise spectrum measurements on graphene FETs (Figure 2-1c) to detect analytes like chloroform, acetonitrile, methanol and tetrahydrofuran. By monitoring the adsorption and desorption of these analytes on graphene in frequency domain they were able to distinguish each analyte based on it characteristic frequency. Another 2-dimensional material, MoS_2 has also been used for high sensitivity detection [51] by monitoring changes in conductance value as well (Figure 2-1d). All the above mentioned nanoelectronic sensors work on the common principle of detecting a change in

conductance of the device due to the charge transfer between a molecule and nanomaterial.

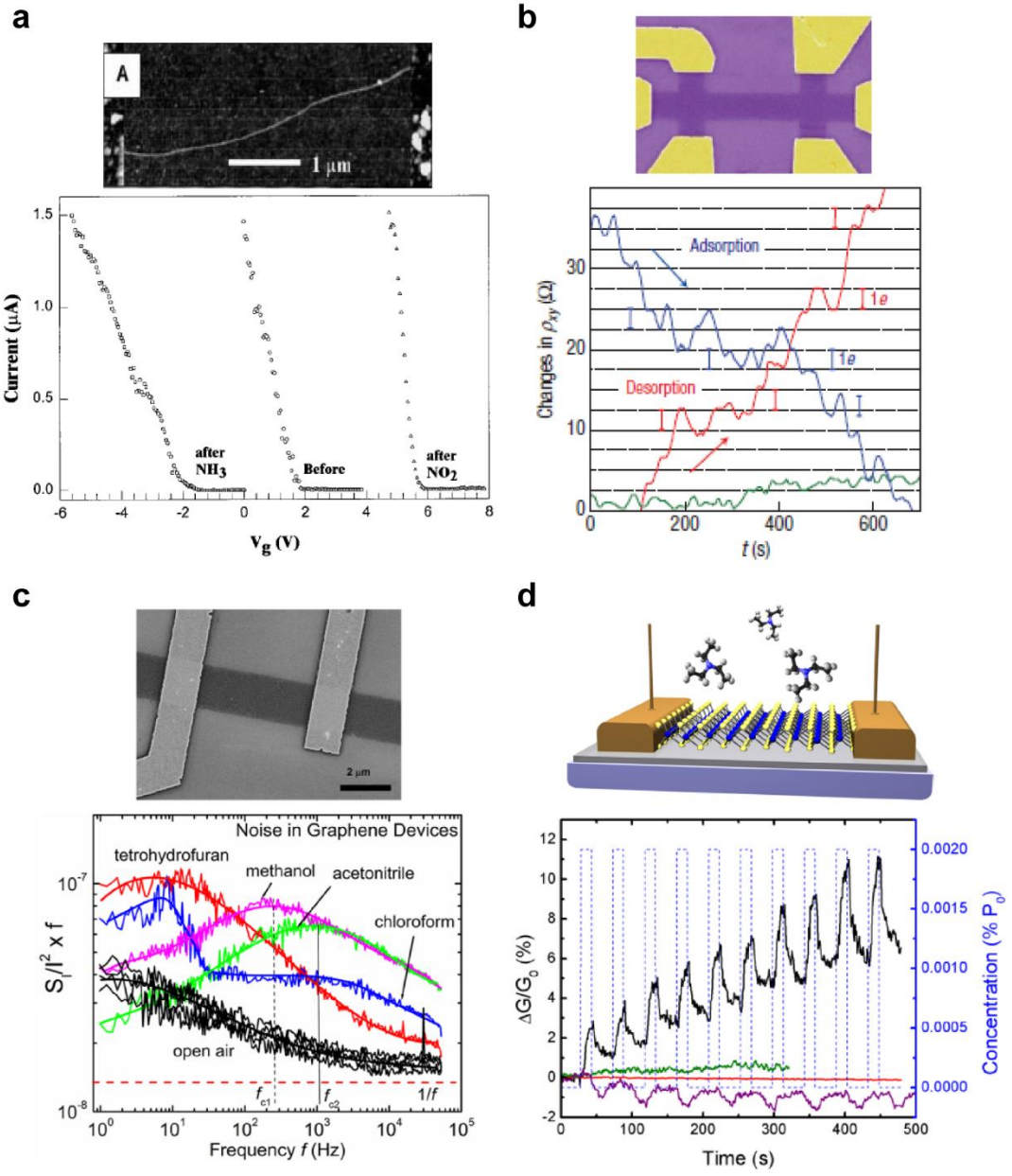

Figure 2-1. **(a)** First demonstration of a carbon nanotube gas sensor showing threshold voltage shift with NO_2 and NH_3 [42]. **(b)** Single molecule adsorption/desorption on a graphene hall bar structure [49]. **(c)** Low frequency noise measurement on graphene transistors for gas detection [50]. **(d)** MoS_2 transistors as vapor sensors for triethylamine [51]. Reprinted from [42, 49-51] with permission.

2.3.2 Limitations of conventional sensors

Presently the most common sensing mechanisms for nanoelectronic sensors, such as chemiresistors and transistor based sensors shown in Figure 2-1, rely on the detection of charges [27,42,49,51]. Charge transfer between the adsorbed molecules and the nanomaterial changes the surface charge density, thus altering the Fermi energy and conductance of the sensors. Sensing is achieved by monitoring the DC conductance change as a result of molecule-sensor interaction. To date, semiconductor nanowires, carbon nanotubes, graphene, graphene-oxide and MoS_2 have been explored as DC nanoelectronic vapor sensors, with sensitivity down to the ppb level [49,52-56]. However, the biggest challenge for such DC nanoelectronic vapor sensors is their extremely slow sensing response and recovery, typically on the order of 10s to 1000s of seconds [42,49,51-54]. For example the nanotube gas sensor shown in Figure 2-1a, has ppm sensitivity however, the response is slow and irreversible (Figure 2-2a). Similarly, graphene hall bar structures [49] of Figure 2-1b, at room temperature have ~1000 seconds response times as shown in Figure 2-2c. Even the low frequency noise spectrum [50] based measurements (Figure 2-1c) suffer from extremely poor sensitivity and slow response times (>100 seconds) as shown in Figure 2-2d. MoS_2 gas sensor shown in Figure 2-1d clearly has poor recovery and around 100 second response times [51].

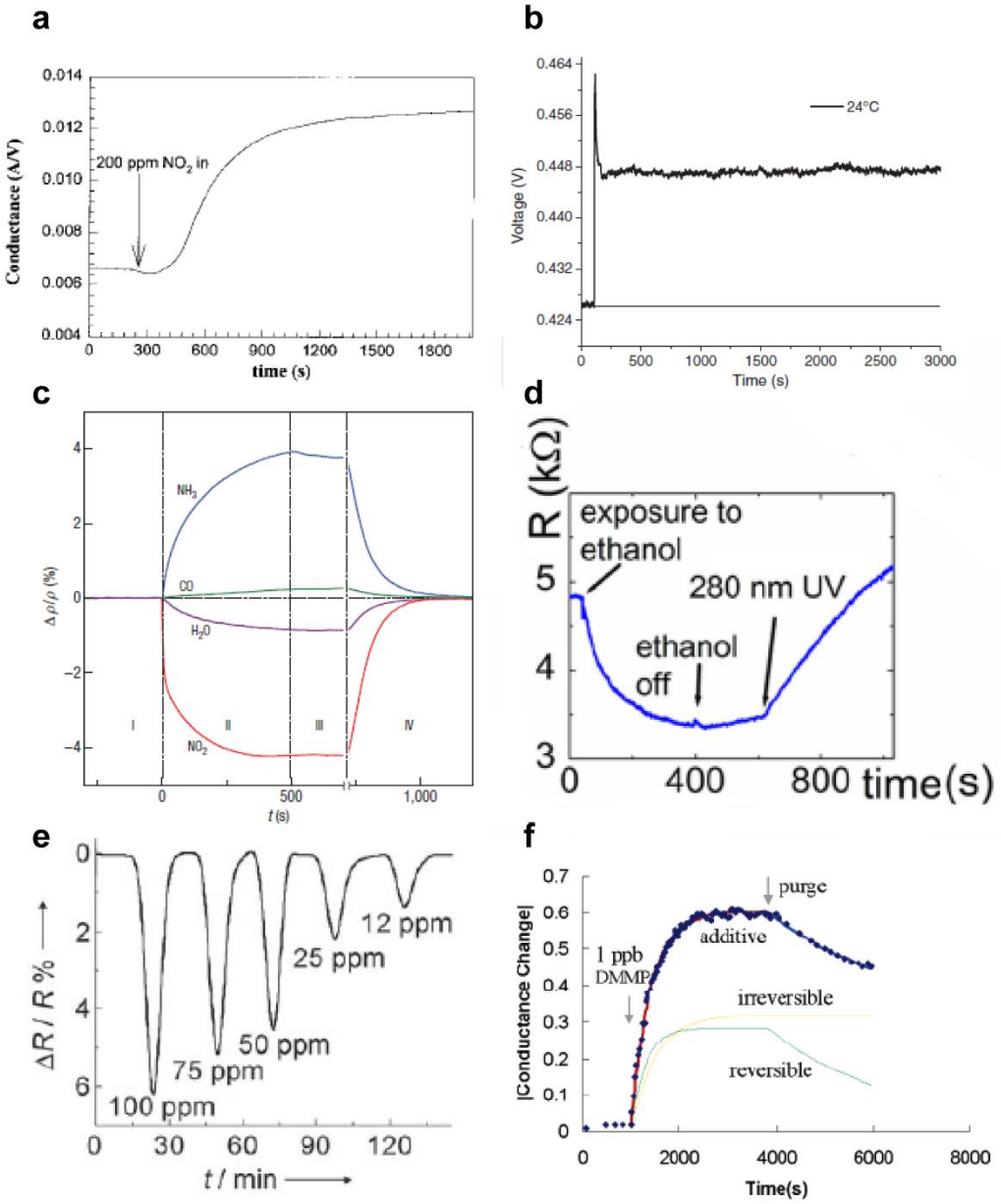

Figure 2-2. **(a)** Response time for NO_2 detection in CNT FET of Figure 2-1a is >100s and is irreversible [42]. **(b)** Nanotube network FET response to toluene is slow and irreversible at room temperature [57]. **(c)** Graphene hall bar from Figure 2-1b can measure single molecule events at low temperature under vacuum but practical operation has low sensitivity, slow response times ~1000s and requires thermal treatment to help desorption [49]. **(d)** Graphene FETs from Figure 2-1c are also slow and irreversible and require UV exposure for desorption [50]. **(e)** Graphene-oxide based FETs show high sensitivity but at the cost of long response time ~10s of minutes [53]. **(f)** Nanotube network FET response for 1ppb DMMP is defect mediated and irreversible [58]. Reprinted from [42, 49, 50, 53, 57, 58] with permission.

Unfortunately, the slow response for all existing nanoelectronic vapor sensors arises intrinsically from slow defect-mediated charge transfer processes and slow dynamics of interface trapped charges [58-60], and therefore, is difficult, if not impossible, to overcome within the current framework of available sensing mechanisms. In fact, high sensitivity in nanosensors is achieved only through the presence of defects, as charge transfer is most efficient at defect sites (Figure 2-2b, e, f). But, this leads to slow desorption as molecule binding energy at defect sites is very high. As a result, device regeneration is achieved only through prolonged heating [49], degassing [50], or ultraviolet radiation [53] (Figure 2-2), all of which are impractical for on-site vapor monitoring systems. Saleh-Khojin et al [57] utilized high-current stimulation of nanotubes to obtain fast reversible responses from defect sites however this defeats the low power operation advantage nanoelectronic sensors have. Recently, various chemoselective surface coatings have been used to reduce the response and recovery time to only a few seconds [40,56,61]. However, these coatings function only for a narrow set of vapor molecules and may possibly result in even slower response to other vapor molecules. These drawbacks significantly hinder the employment of nanoelectronic sensors in applications like gas chromatography (GC), which require detection capability for a broad range of vapor analytes with sub-second response time and ppb-level sensitivity.

2.4 Nanoelectronic biological sensors

2.4.1 Previous work

Nanomaterials are sensitive to the changes in their immediate vicinity. In fact, these materials have been shown to be extremely sensitive towards the pH [27,62,63] of surrounding environment as well.

A lot of work has been done in the area of bio-sensing using nanowires, especially at Harvard (Lieber group). In the first nanowire sensing experiment, Cui et al. (2001) modified the surface of silicon nanowires (SiNWs) to detect streptavidin and calcium ions [27], and attributed it to the change in the nanowire surface charge (Figure 2-3a). Another study by Zheng et al showed multiplexed detection of cancer markers [28] using silicon nanowire FETs. In this work, silicon nanowires were functionalized with antibody receptors for prostate specific antigen, carcinoembroyic antigen and mucin-1. In real time flow measurements, they were able to detect these proteins with detection limits of ~50 fg/ml (Figure 2-3b). Moreover, they showed detection of telomerase from as small as ten tumor cells, comparable to commercial technology which uses fluorescent labels to optically detect telomerase. In fact, using a similar setup Patolsky et al. showed detection of single virus particles [37]. The observed signal in all the above cases was attributed to a change in the nanowire surface charge. For a p-type nanowire, a more negative (positive) surface charge causes a conductance increase (decrease). All of the above studies were carried out in a low ionic strength buffer solution, however, for practical applications real-time detection needs to happen in physiological conditions, where ionic strength can be as high as 150 mM, e.g., in blood plasma. One way to address is to have a purification step built on-chip. Stern et

al. built a microfluidic purification chamber on-chip which captured biomarkers from blood, after which the chamber was flushed with buffer solution and the markers released onto a silicon nanowire FET for detection [64]. The detection time was 20 minutes and the setup required no other time-consuming pre-processing step. A lot of exciting work has been done on live neuron cells [65] as well using silicon nanowires.

Carbon nanotubes and graphene also have shown similar detection capabilities. Amazingly, biomolecules like DNA have been hypothesized to wrap around the CNT by sharing π-electrons [66]. Star et al. functionalized carbon nanotube FETs with single-strand DNA which acted as capture probes. The response of the nanotube FETs towards hybridization [67] (Figure 2-3d) with target DNA strands was monitored. They observed changes in conductance of the device with DNA hybridization which was attributed to doping of nanotube by the DNA. However, this study was conducted in a dry environment. Gruner et al later showed detection of streptavidin in dry as well as buffer solution on carbon nanotube field effect transistors [68], proving that the effect arises from the charge transfer from protein to CNT mediated by NH_2 groups (Figure 2-3e). A seminal work in the field of non-covalent functionalization was carried out by Chen et al. where they showed that a pyrene linker molecule π-stacks on the hexagonal structure of carbon nanotubes and provides a tool for label free detection [69], without degrading the electronic properties. Materially, carbon nanotube and graphene are similar and using the same functionalization technique electrical detection of glucose on carbon nanotube [70] and graphene [71] based FETs has been demonstrated (Figure 2-3f).

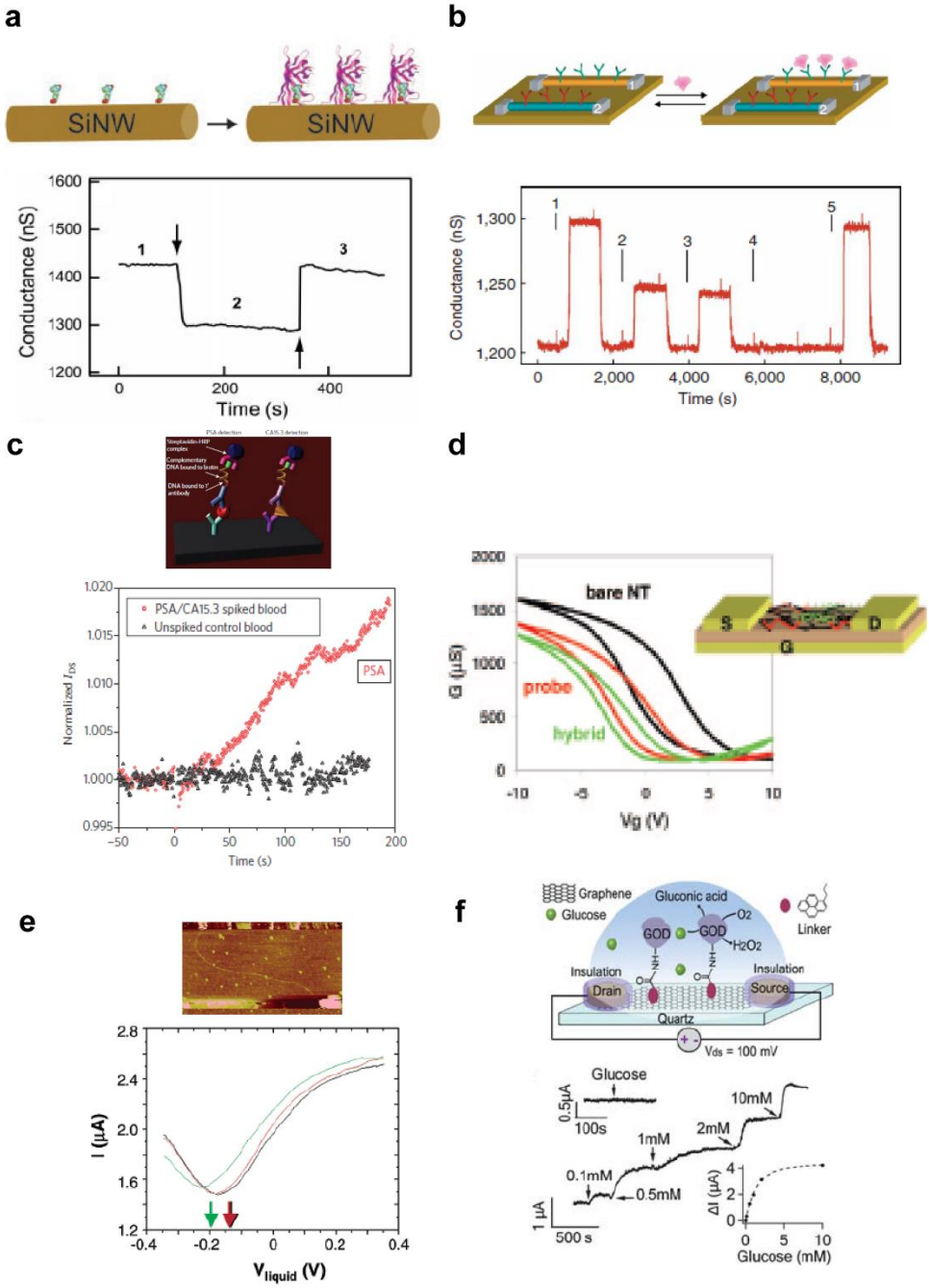

Figure 2-3. **(a)** Silicon Nanowire FET for detection of biotin-antibiotin binding [27]. **(b)** Detection of PSA antibody with lowest detection limit 0.9 pg/ml marked as 2 and 3 in bottom panel [28]. **(c)** Detection of PSA from whole blood on a SiNW FET with an on chip purification step [64]. **(d)** Detection of DNA hybridization using CNT-FET with functionalized ssDNA as a probe [67]. **(e)** Streptavidin detection on carbon nanotube in 15mM phosphate buffer after 10 hours of incubation [68]. **(f)** Graphene FET based glucose detector pyrene-linker molecule to functionalize glucose oxidase receptors [71]. Reprinted from [27, 28, 64, 67, 68, 71] with permission.

2.4.2 Limitations of conventional sensors

A lot of interesting work has been done on nanoscale biosensors and detection of a wide array of organic and inorganic molecules have been demonstrated on these devices. Almost all conventional nano sensors described in literature work on the principle of charge detection. The transfer of charge to/from the molecule or electrostatic gating due to the molecule leads to a change in the charge density of the nano sensor [41]. This manifests as a change in the DC conductance of the device which is monitored for sensing the biomolecule. Although, charge-detection based sensing mechanism has many advantages, including label-free detection [72], femto-molar sensitivity [36] and electronic read out capability [28]; it however fails in high background salt concentrations where the sensitivity of the devices suffers from the ionic screening due to mobile ions present in the solution [73-75].

A charged surface in an ionic solution attracts counter-ions from the solution, forming an electrical double layer (EDL) and effectively screening off the charges. The columbic potential due to the surface falls off exponentially as we move away from it. This ionic screening effect is characterized by the Debye screening length λ_D,

$$\lambda_D = \sqrt{\frac{\varepsilon k_B T}{q^2 c}}, \qquad \text{Equation 2-1}$$

where ε is the dielectric permittivity of the media, k_B is the Boltzmann's constant, T is the temperature, q is the electron charge, and c is the ionic strength of the electrolyte solution. For a typical 100 mM buffer solution, λ_D is around 1 nm and the surface potential will be completely screened at a distance of a few nm.

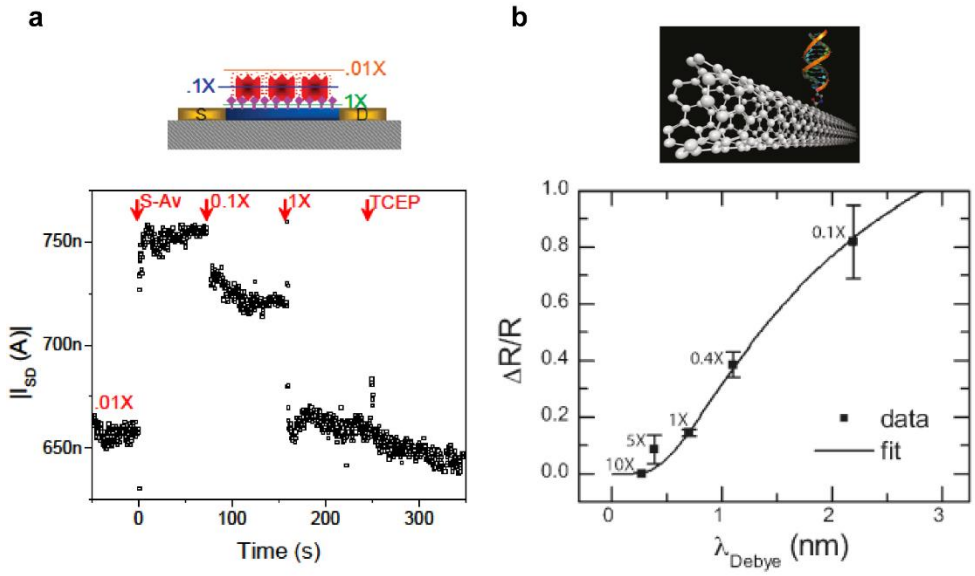

Figure 2-4. **(a)** Silicon nanowire FET with biotin receptor molecules and a diagrammatic representation of the range of influence of charges in various background concentrations. (Bottom) Signal response to streptavidin injection and the corresponding sensitivity in different PBS buffer strengths. From [75]. **(b)** Point functionalized carbon nanotube with 5´ ended amine probe DNA. (Bottom) Signal response to target DNA in different ionic strength solutions confirming Debye screening effect [74]. Reprinted from [74, 75] with permission.

In a control study, Stern et al. [75] demonstrated that as one moves towards higher background ionic concentrations, the sensitivity of the nanowire nano sensors drops (Figure 2-4a). They show that in 0.01X PBS buffer solution background (λ_D ~ 7.3 nm), 10 nM streptavidin can be easily detected on their biotinylated silicon nanowire FETs due to minimal screening. A tenfold increase in the ionic strength of the buffer (0.1X PBS, λ_D ~ 2.3 nm) partially screens streptavidin's intrinsic charge, whereas at 1X PBS (λ_D ~ 0.7 nm) the current signal $|I_{SD}|$ returns to baseline value indicating complete screening of the charges. To confirm the Debye screening effect, they add 1 μM TCEP in 0.01X PBS which removes streptavidin from the surface, and the signal still remains at baseline. A similar study [74] was carried out on carbon nanotubes which were point-functionalized with probe DNAs in order to capture target

DNAs from the solution (Figure 2-4b). By varying the buffer strength in which the target DNAs were delivered, it was shown that the sensor response depended on the background buffer's ionic strength.

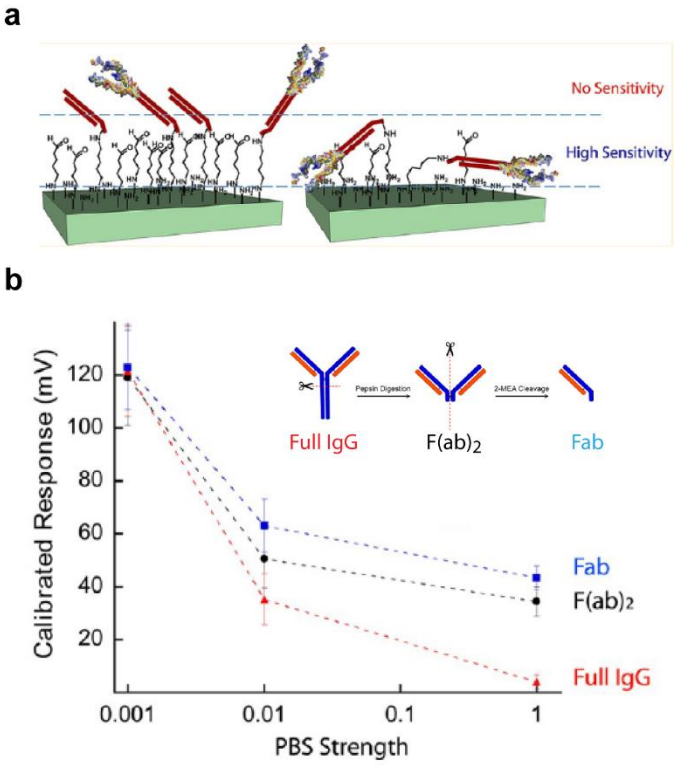

Figure 2-5. **(a)** Surface engineering with size-reduced receptor molecules to enhance detection in high ionic strength solutions. **(b)** Sensor response to full antibody IgG (12 nm in size), and two cleaved shorter antibody segments $F(ab)_2$ and Fab showing the importance of Debye screening. Reprinted from [76] with permission.

In another study Patolsky et al. modified the surface receptor molecule sizes so as to keep the receptors within 1 nm of the sensor surface [76] (Figure 2-5). They functionalized the surface with immunoglobinG (IgG) antibody as well as its shorter engineered versions, $F(ab)_2$ and Fab and monitored the change in response to antihuman cardiac Troponin T in different buffer strengths (Figure 2-5b). In 1X PBS

background, they observed that the full antibody IgG (~12-14 nm in size) complex is completely screened yielding no signal.

Due to ionic screening effect, most of the conventional nanoelectronic sensors operate either in the dry state [67] or low ionic buffer solutions [36,41,68,70,72] (<10 mM), else the sample needs to undergo a de-salting process [28]. Since physiologically relevant ionic strength are ~100 mM, mitigating ionic screening effect is critical for Point-of-Care (POC) nanoelectronic biosensors where detection needs to be carried out at patient site with limited sample processing capability.

2.5 Discussion

In this chapter, we gave a brief overview of nanoelectronic sensors and the previous work done in the area of chemical and biological sensing using nanomaterials like carbon nanotubes, nanowires, graphene and MoS_2. We highlighted that conventional nanoelectronic sensors work on the principle of detection of charges of the associated molecules. Charge transfer or electrostatic gating due to the molecules can change the surface charge density of a nanosensor leading to a conductance change, which is monitored. We also discussed in detail the challenges faced by such charge detection based measurements for both chemical and biological sensors. These challenges are inherent to the measurement technique rather than sensor's material properties. In spite of our ability to build robust electronic sensors from nanomaterials, the available sensing technologies still hinder rapid, real-time and on-site operation of these nanosensors.

In the following chapter, we introduce a new sensing technology based on heterodyne mixing to investigate the fundamental interaction between an oscillating molecular dipole and charge density fluctuation inside a nanoelectronic sensor, and to

address the challenges faced by conventional nanoelectronic sensors. Heterodyne mixing is a versatile technique and in following chapters, we will demonstrate heterodyne molecular detection both, in liquid and gas phases, and on two different platforms, carbon nanotube and graphene. Moreover, we utilize heterodyne mixing as a probe to study the behavior of small molecules near the graphene surface. Our approach not only addresses the challenges facing conventional sensing technologies but also provides a tool to study fundamental molecule-nanomaterial interactions. Further, our technique is platform independent and can be easily extended to other nanomaterials like nanowires and metal dichlacogenides as well.

References

[1] D. V. Lim, J. M. Simpson, E. A. Kearns, and M. F. Kramer, Clinical Microbiology Reviews **18**, 583 (2005).

[2] J. Carrano, DARPA, Public Release #2435, 2004.

[3] A. R. Clifford K. Ho, David R. Miller, and Mary J. Davis, Sensors for Environmental Monitoring and Long-Term Environmental Stewardship, 2004.

[4] T. Shigemori, The 14th International Meeting on Chemical Sensors (2012).

[5] R. Ketteler, Z. Sun, K. F. Kovacs, W.-W. He, and B. Seed, Genome Biology **9** (2008).

[6] D. C. Hay Burgess, J. Wasserman, and C. A. Dahl, Nature **444 Suppl 1**, 1 (2006).

[7] E. D. Dawson *et al.*, Analytical Chemistry **79**, 378 (2007).

[8] F. S. Ligler and J. S. Erickson, Nature **440**, 159 (2006).

[9] S. Deo, E. Moschou, S. Peteu, P. Eisenhardt, L. Bachas, M. Madou, and S. Daunert, Analytical Chemistry **75**, 207A (2003).

[10] M. J. Madou and R. Cubicciotti, Proceedings of the Ieee **91**, 830 (2003).

[11] D. Janasek, J. Franzke, and A. Manz, Nature **442**, 374 (2006).

[12] S. S. Iqbal, M. W. Mayo, J. G. Bruno, B. V. Bronk, C. A. Batt, and J. P. Chambers, Biosensors & Bioelectronics **15**, 549 (2000).

[13] P. L. Bergstrom, PhD Thesis, University of Michigan, 1996.

[14] J. R. Crowther, *Elisa: Theory and Practice* (Humana Press, New York, 1995).

[15] L. J. Kricka, *Nonisotoic Probing, Blotting, and Sequencing* (Academic Press, New York, 1995), 2nd Edn. edn.

[16] K. M. Marks and G. P. Nolan, Nature Methods **3**, 591 (2006).

[17] D. V. Lim, Proceedings of the Ieee **91**, 902 (2003).

[18] T. Konry, A. Novoa, S. Cosnier, and R. S. Marks, Analytical Chemistry **75**, 2633 (2003).

[19] K. M. Hansen and T. Thundat, Methods **37**, 57 (2005).

[20] A. K. Naik, M. S. Hanay, W. K. Hiebert, X. L. Feng, and M. L. Roukes, Nature Nanotechnology **4**, 445 (2009).

[21] V. Cimalla *et al.*, Sensors and Actuators B-Chemical **126**, 24 (2007).

[22] P. S. Waggoner and H. G. Craighead, Lab on a Chip **7**, 1238 (2007).

[23] Y. T. Yang, C. Callegari, X. L. Feng, K. L. Ekinci, and M. L. Roukes, Nano letters **6**, 583 (2006).

[24] H. Craighead, Nature **442**, 387 (2006).

[25] M. M. C. Cheng *et al.*, Current Opinion in Chemical Biology **10**, 11 (2006).

[26] C. D. Keating, Proceedings of the National Academy of Sciences of the United States of America **102**, 2263 (2005).

[27] Y. Cui, Q. Q. Wei, H. K. Park, and C. M. Lieber, Science **293**, 1289 (2001).

[28] G. F. Zheng, F. Patolsky, Y. Cui, W. U. Wang, and C. M. Lieber, Nature Biotechnology **23**, 1294 (2005).

[29] D. J. Caruana and A. Heller, Journal of the American Chemical Society **121**, 769 (1999).

[30] C. Boozer, G. Kim, S. Cong, H. Guan, and T. Londergan, Current Opinion in Biotechnology **17**, 400 (2006).

[31] M. J. M. Madou, S. R. , *Chemical Sensing with Solid State Devices.* (Academic Press, New York, 1989).
[32] B. H. Vanderschoot and P. Bergveld, Biosensors **3**, 161 (1987).
[33] M. Li, H. X. Tang, and M. L. Roukes, Nat. Nanotechnol. **2**, 114 (2007).
[34] D. H. Zhang, Z. Q. Liu, C. Li, T. Tang, X. L. Liu, S. Han, B. Lei, and C. W. Zhou, Nano Letters **4**, 1919 (2004).
[35] J. P. Novak, E. S. Snow, E. J. Houser, D. Park, J. L. Stepnowski, and R. A. McGill, Applied Physics Letters **83**, 4026 (2003).
[36] E. Stern, J. F. Klemic, D. A. Routenberg, P. N. Wyrembak, D. B. Turner-Evans, A. D. Hamilton, D. A. LaVan, T. M. Fahmy, and M. A. Reed, Nature **445**, 519 (2007).
[37] F. Patolsky, G. F. Zheng, O. Hayden, M. Lakadamyali, X. W. Zhuang, and C. M. Lieber, Proceedings of the National Academy of Sciences of the United States of America **101**, 14017 (2004).
[38] J. Kong and H. J. Dai, Journal of Physical Chemistry B **105**, 2890 (2001).
[39] A. Star, T. R. Han, J. C. P. Gabriel, K. Bradley, and G. Gruner, Nano Letters **3**, 1421 (2003).
[40] E. S. Snow, F. K. Perkins, E. J. Houser, S. C. Badescu, and T. L. Reinecke, Science **307**, 1942 (2005).
[41] I. Heller, A. M. Janssens, J. Mannik, E. D. Minot, S. G. Lemay, and C. Dekker, Nano Letters **8**, 591 (2008).
[42] J. Kong, N. R. Franklin, C. W. Zhou, M. G. Chapline, S. Peng, K. J. Cho, and H. J. Dai, Science **287**, 622 (2000).
[43] A. Star, T. R. Han, V. Joshi, J. C. P. Gabriel, and G. Gruner, Advanced Materials **16**, 2049 (2004).
[44] P. G. Collins, K. Bradley, M. Ishigami, and A. Zettl, Science **287**, 1801 (2000).
[45] Z. Y. Fan, D. W. Wang, P. C. Chang, W. Y. Tseng, and J. G. Lu, Applied Physics Letters **85**, 5923 (2004).
[46] Y.-J. Choi, I.-S. Hwang, J.-G. Park, K. J. Choi, J.-H. Park, and J.-H. Lee, Nanotechnology **19** (2008).
[47] D. J. Zhang, C. Li, X. L. Liu, S. Han, T. Tang, and C. W. Zhou, Applied Physics Letters **83**, 1845 (2003).
[48] M. C. McAlpine, H. Ahmad, D. Wang, and J. R. Heath, Nature Materials **6**, 379 (2007).
[49] F. Schedin, A. K. Geim, S. V. Morozov, E. W. Hill, P. Blake, M. I. Katsnelson, and K. S. Novoselov, Nature Materials **6**, 652 (2007).
[50] S. Rumyantsev, G. Liu, M. S. Shur, R. A. Potyrailo, and A. A. Balandin, Nano Letters **12**, 2294 (2012).
[51] F. K. Perkins, A. L. Friedman, E. Cobas, P. M. Campbell, G. G. Jernigan, and B. T. Jonker, Nano Letters **13**, 668 (2013).
[52] J. Li, Y. J. Lu, Q. Ye, M. Cinke, J. Han, and M. Meyyappan, Nano Letters **3**, 929 (2003).
[53] V. Dua, S. P. Surwade, S. Ammu, S. R. Agnihotra, S. Jain, K. E. Roberts, S. Park, R. S. Ruoff, and S. K. Manohar, Angewandte Chemie-International Edition **49**, 2154 (2010).
[54] Y. Dan, Y. Lu, N. J. Kybert, Z. Luo, and A. T. C. Johnson, Nano Letters **9**, 1472 (2009).

[55] C. Yu, Q. Hao, S. Saha, L. Shi, X. Y. Kong, and Z. L. Wang, Applied Physics Letters **86** (2005).
[56] C. Y. Lee, R. Sharma, A. D. Radadia, R. I. Masel, and M. S. Strano, Angewandte Chemie-International Edition **47**, 5018 (2008).
[57] A. Salehi-Khojin, K. Y. Lin, C. R. Field, and R. I. Masel, Science **329**, 1327 (2010).
[58] C. Y. Lee and M. S. Strano, Langmuir **21**, 5192 (2005).
[59] W. Kim, A. Javey, O. Vermesh, O. Wang, Y. M. Li, and H. J. Dai, Nano Letters **3**, 193 (2003).
[60] S. Kar, A. Vijayaraghavan, C. Soldano, S. Talapatra, R. Vajtai, O. Nalamasu, and P. M. Ajayan, Applied Physics Letters **89**, 132118 (2006).
[61] C. Y. Lee and M. S. Strano, Journal of the American Chemical Society **130**, 1766 (2008).
[62] P. K. Ang, W. Chen, A. T. S. Wee, and K. P. Loh, Journal of the American Chemical Society **130**, 14392 (2008).
[63] M. Kaempgen and S. Roth, Journal of Electroanalytical Chemistry **586**, 72 (2006).
[64] E. Stern, A. Vacic, N. K. Rajan, J. M. Criscione, J. Park, B. R. Ilic, D. J. Mooney, M. A. Reed, and T. M. Fahmy, Nature Nanotechnology **5**, 138 (2010).
[65] F. Patolsky, B. P. Timko, G. Yu, Y. Fang, A. B. Greytak, G. Zheng, and C. M. Lieber, Science **313**, 1100 (2006).
[66] M. Zheng *et al.*, Science **302**, 1545 (2003).
[67] A. Star, E. Tu, J. Niemann, J. C. P. Gabriel, C. S. Joiner, and C. Valcke, Proceedings of the National Academy of Sciences of the United States of America **103**, 921 (2006).
[68] K. Bradley, M. Briman, A. Star, and G. Gruner, Nano Letters **4**, 253 (2004).
[69] R. J. Chen, Y. G. Zhang, D. W. Wang, and H. J. Dai, Journal of the American Chemical Society **123**, 3838 (2001).
[70] K. Besteman, J. O. Lee, F. G. M. Wiertz, H. A. Heering, and C. Dekker, Nano Letters **3**, 727 (2003).
[71] Y. Huang, X. Dong, Y. Shi, C. M. Li, L.-J. Li, and P. Chen, Nanoscale **2**, 1485 (2010).
[72] F. Patolsky, G. F. Zheng, and C. M. Lieber, Analytical Chemistry **78**, 4260 (2006).
[73] G.-J. Zhang *et al.*, Nano Letters **8**, 1066 (2008).
[74] S. Sorgenfrei, C.-y. Chiu, M. Johnston, C. Nuckolls, and K. L. Shepard, Nano Letters **11**, 3739 (2011).
[75] E. Stern, R. Wagner, F. J. Sigworth, R. Breaker, T. M. Fahmy, and M. A. Reed, Nano Letters **7**, 3405 (2007).
[76] R. Elnathan, M. Kwiat, A. Pevzner, Y. Engel, L. Burstein, A. Khatchtourints, A. Lichtenstein, R. Kantaev, and F. Patolsky, Nano Letters **12**, 5245 (2012).

Chapter 3

Heterodyne mixing in nanoelectronic devices

3.1 Introduction

Heterodyne mixing or frequency mixing is commonly used in communication systems and signal broadcasting, most noticeable in FM/AM receivers [1,2]. It is based on the principle of mixing two different frequency signals to yield new signals at the sum and difference of the two input frequencies. In radio transmission, it is the difference or beat frequency which is locked into to read information. In order to implement frequency mixing, a non-linear electronic device e.g. diode or transistor where the output depends non-linearly on the input, is used. Generally, the output current in such devices can be represented as

$$I(V) = A_1 \cdot V + A_2 \cdot V^2 + A_1 \cdot V^3 \ldots.$$

If, $V = V_1 \cos 2\pi f_1 t + V_2 \cos 2\pi f_2 t$ where $2\pi f_{1,2} = \omega_{1,2}$, then the second term in the above equation yields an output at $f_1 \pm f_2$. In radio transmission, the advantage of heterodyning lies in the fact that once we fix the beat frequency, $f_{beat} = f_1 - f_2$ to a particular value, we need to tune only the local oscillator, f_2 to receive different stations, rather than having a different receiver for different broadcast stations at f_1.

Heterodyne mixing is widely used in optical detection [3,4], where it provides gain as well as better noise rejection. Heterodyne mixing is used to down convert the terahertz signal, so that normal electronics can be used for signal amplification and

detection. Photon absorption process is non-linear in 'square-law detectors', where energy flux scales as the square of the incident electric field. If at the input of the detector, we have the incident light and a local oscillator (LO) signal then,

$$I \propto \left(E_{light} \cos \omega_{light}\, t + E_{LO} \cos \omega_{LO}\, t\right)^2 \propto 2E_{light}E_{LO}\, (\cos \omega_{light}\, t)(\cos \omega_{LO}\, t)$$

Mixing of the two frequency components above leads to a difference frequency, which is monitored. One can, not only provide gain through the local oscillator amplitude but also detect the phase of the light signal leading to sensitive measurements. In nano-electro-mechanical systems too, frequency mixing has been employed using the non-linearity in the device response [5-8], to down convert frequencies below the detection bandwidth of the device defined by its resistance and capacitance.

In this thesis, we adopt heterodyne mixing technique to investigate the fundamental interaction between an oscillating molecular dipole and the charge density fluctuation inside a nanoelectronic sensor. Heterodyne detection has been ignored in electronic sensing techniques due mainly to the lack of gain in conventional two-terminal devices. Here, we show that heterodyne chemical and biological sensors can provide rapid, sensitive detection and overcome the challenges of conventional state-of-art sensors. In this chapter, we present the mixing current measurement technique used in our work. In our study, we use carbon nanotube and graphene based field-effect-transistors. In Section 3.2, we describe the general electrical response of a nanoelectronic sensor which covers all the conventional state-of-art sensors of chapter 2 as well. In Section 3.3, we present the theory of heterodyne sensing technique followed by the measurement setup we use to implement heterodyne detection in

Section 3.4. Finally, we compare the theoretical model with experimental results obtained in carbon based transistors in Section 3.5.

3.2 Nanoelectronic sensor response

For any nanoelectronic device, we can relate the output response of the device to a set of input parameters. In two-terminal devices like a diode, the output current is controlled by the applied voltage across the two terminals [9,10]. Similarly, for three-terminal devices like transistors (MOSFET/BJT) the output current flowing through two terminals is controlled by the voltage across them as well as the voltage at the third terminal (gate/base terminal) [9,10]. Even though, the output current also depends on the properties of semiconductor material in these devices e.g. doping, carrier mobility, width, length in a p-n diode/MOSFET or the metal-semiconductor barrier height in a Schottky diode, these values are fixed and generally independent of the input voltages especially in the small voltage bias regimes. Hence, for a small applied bias voltage[1], V one can write down a generic current-voltage equation for these devices as

$$I = G \cdot V \,, \qquad \text{Equation 3-1}$$

where I is the current through the device and G is the conductance of the device. Considering a small signal perturbation also applied to the device at frequency $\omega/2\pi$, we can modify Equation 3-1 as

$$I = (G + \tilde{G}^{\omega}) \cdot (V + \tilde{V}^{\omega}) \,, \qquad \text{Equation 3-2}$$

where $\tilde{G}^{\omega}$ is the modulated conductance and $\tilde{V}^{\omega}$ is the modulated voltage at frequency $\omega/2\pi$. Simplifying Equation 3-2 we get,

[1] For a diode $I = I_0(e^{\alpha V} - 1)$. A small signal Taylor expansion gives us $I = I_0\left(\alpha V + \frac{1}{2}(\alpha V)^2\right)$. This has a linear term as well as a quadratic term associated with the non-linearity in the device. For a transistor, $I = k\left(V_g + \frac{1}{2}V_{sd}\right)V_{sd}$ from chapter 1, which also consists of a linear and a quadratic term.

$$I = G \cdot V + G \cdot \tilde{V}^{\omega} + \tilde{G}^{\omega} \cdot V + \tilde{G}^{\omega} \cdot \tilde{V}^{\omega} \,. \qquad \text{Equation 3-3}$$

Equation 3-3 gives an insight into the various sensing methodologies that have been applied for chemical and biological detection using nanoelectronic devices till date. The first term $G \cdot V$ represents the direct current term i.e. DC detection technique. The presence of any molecule in the vicinity of a nano sensor changes the conductance *G* of the device which provides the dc sensing signal. The second term, $G \cdot \tilde{V}^{\omega}$ is the alternating current (AC) detection technique, where one monitors the ac conductance change of the sensor for an applied ac bias voltage. In principle, dc or ac conductance measurements are the same, except that one can have a better signal-to-noise ratio (SNR), and hence sensitivity by reading the output at the driving frequency, $f = \omega/2\pi$ using a lock-in amplifier. The third term in Equation 3-3 measures the modulation in the conductance $\tilde{G}^{\omega}$ at dc bias caused by the presence of a molecule in the local environment of a nano sensor. The change in sensor behavior is monitored by analyzing the low frequency noise spectrum in the device, which in the time domain appears as random telegraph noise. To date, the above three sensing mechanism have been the most commonly used techniques for electrical detection of chemical and biological species using nanoelectronic devices. In all the above techniques, one relies on the ability of a molecule to accept/donate electrons from/to the nanosensor, thereby causing a change in the conductance or electrochemical potential of the device. Such charge-detection based techniques have several limitations which have been discussed in detail in chapter 2.

In this thesis, we present a fundamentally new detection technique based on heterodyne mixing which is given by the fourth term of Equation 3-3, $\tilde{G}^{\omega} \cdot \tilde{V}^{\omega}$. To

implement this, we use a three-terminal field-effect-transistor device structure. This term arises due to the mixing of two ac signals – one from the source-drain excitation voltage and second, from the conductance modulation in the device caused by an adsorbed molecule on sensor surface. The mixing current obtained due to sinusoidal modulation of the bias voltage and device conductance can be expressed as,

$$I_{mix} = \tilde{G}^{\omega} \cdot \tilde{V}^{\omega}$$

$$I_{mix} = \left|\tilde{G}\right|\cos\omega t \cdot \left|\tilde{V}\right|\cos\omega t = \left|\tilde{G}\right|\left|\tilde{V}\right|\cos^2\omega t \qquad \text{Equation 3-4}$$

$$I_{mix} = \frac{|\tilde{G}||\tilde{V}|}{2}(1 + \cos 2\omega t) \qquad \text{Equation 3-5}$$

$$I_{mix}^{DC} = \frac{|\tilde{G}||\tilde{V}|}{2} \qquad \text{Equation 3-6}$$

The first term in Equation 3-5 is a DC term and is the sensing signal. The DC term (Equation 3-6) suggests that we can modulate the nanosensor at high frequencies, avoiding low frequency $1/f$ noise and still obtain a readout at DC, which simplifies the detection circuitry [11,12].

3.3 Theory of heterodyne sensing

Now, we derive a general expression for mixing current for a three terminal field-effect-transistor. For our carbon nanomaterial device, the conductance modulation, $\tilde{G}^{\omega}$ arises due to modulation of charge in the carbon channel. Hence,

$$\tilde{G} = \frac{dG}{dq}\tilde{q}\ . \qquad \text{Equation 3-7}$$

In a three terminal field-effect-transistor device, the modulation of charge can happen due to an external perturbation (i.e. absorbed molecule effect), a modulation of the gate capacitance or the applied gate voltage.

$$\tilde{q} = \tilde{q}_{ext} + \tilde{C}_g(\omega)V_g^{DC} + C_g\tilde{V}_g^{\omega}. \qquad \text{Equation 3-8}$$

In this thesis, all devices are lying on a silicon substrate i.e. are non-suspended and we do not have any capacitance modulation of gate. Therefore,

$$\tilde{q} = \tilde{q}_{ext} + C_g \tilde{V}_g^{\omega} \ . \qquad \text{Equation 3-9}$$

Now, using Equation 3-7 and Equation 3-9 in heterodyne term $\tilde{G}^{\omega} \cdot \tilde{V}^{\omega}$, we have

$$I_{mix} = \frac{dG}{dq}(\tilde{q}_{ext} + C_g \tilde{V}_g^{\omega})\tilde{V}^{\omega}. \qquad \text{Equation 3-10}$$

The term $\frac{dG}{dq}$ is related to the transconductance of the device which can be measured from the DC current-voltage characteristics of the device. Since, $q = CV_g$ we have

$$\frac{dG}{dq} = \frac{1}{C_g}\frac{dG}{dV_g^{DC}} \qquad \text{Equation 3-11}$$

and Equation 3-10 can be written as

$$I_{mix} = \frac{1}{C_g}\frac{dG}{dV_g^{DC}}(\tilde{q}_{ext} + C_g \tilde{V}_g^{\omega})\tilde{V}^{\omega}. \qquad \text{Equation 3-12}$$

We see that the mixing current term has two components. The first term in Equation 3-12 is of interest to us and represents modulation of charge in the nano-channel caused by external perturbation. We monitor this term to detect any adsorbed species on the sensor. The AC drive voltage causes a perturbation of adsorbed molecules' dipole which in turn induces a charge-density modulation in the nanotube or graphene channel. We will discuss and derive equations for charge-density modulation caused by adsorbed molecules on a carbon nanotube and graphene channel in chapter 4 and chapter 5, respectively.

The second term in Equation 3-12, is the background mixing current which is always present due to the non-linearity associated with the gate terminal of a transistor. We will come back to this in Section 3.5. The above results can also be derived from

the transistor current-voltage characteristic equation or using a small signal Taylor expansion [13] of current given by $I(V+\delta V) = I(V) + \frac{dI}{dV}(\delta V) + \frac{1}{2}\frac{d^2I}{dV^2}(\delta V)^2$.

3.4 'One-source' heterodyne mixing setup

The discussion here is based on the work by Sazonova [5,14] on carbon nanotube based NEMs oscillators. Generally, an FET frequency mixer is realized by using two frequency sources, f_1 and f_2 which are applied at source and gate terminals, and the output contains the mixed frequencies, $f_1 \pm f_2$ at the drain [1]. However, in our study we use a 'one source' setup [14], wherein an amplitude modulated (AM) voltage applied at the source terminal provides both the signals, one for the source drive and one for mixing down the response. To understand the 'one source' setup [5,14], let us consider a carbon nanomaterial based FET as shown in Figure 3-1 below.

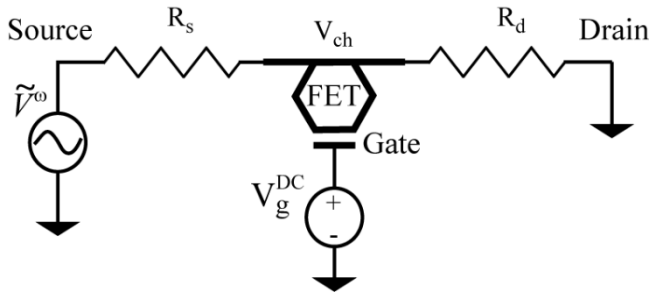

Figure 3-1. Simple 3-terminal FET model. AC voltage is applied at source and gate and drain are grounded. The contact resistance associated with source and drain are shown. © Vera Sazonova, 2006. Adapted from [14].

An AC voltage $\tilde{V}^{\omega}$ is applied to the source and the gate is provided with a DC voltage V_g^{DC}. Now, the potential at the carbon channel is $V_{ch} = \tilde{V}^{\omega}\frac{R_d}{R_s+R_d}$ using simple voltage division given that the drain is grounded. Considering $R_s = R_d$ (source and drain metal pads deposited at the same time) we have,

$$V_{ch} = \frac{1}{2}\tilde{V}^{\omega} \qquad \text{Equation 3-13}$$

The effective gate voltage which the carbon channel will feel at an applied gate voltage, V_g^{DC} with respect to the potential at the carbon channel is

$$V_g^{eff} = V_g^{DC} - V_{ch} \qquad \text{Equation 3-14}$$

$$V_g^{eff} = V_g^{DC} - \frac{1}{2}\tilde{V}^{\omega}. \qquad \text{Equation 3-15}$$

Hence, even with a 'one-source' setup, we can obtain two signals for frequency mixing, one from the source, $\tilde{V}^{\omega}$ and the other from effective gate given by Equation 3-15. If, $V_g^{DC} = 0$ then $V_g^{eff} = -\frac{1}{2}\tilde{V}^{\omega}$, and $V_{sd} = \tilde{V}^{\omega}$. In our heterodyne sensors, this inherent non-linearity associated with the gate adds to the background mixing current. Also, the effective gate voltage helps excite the dipoles of adsorbed molecules, which in turn leads to a conductance fluctuation, as will be discussed later.

We apply an AM modulated source voltage at the source terminal as shown in Figure 3-2 for better noise rejection. The AM voltage drive is provided by HP Agilent 8648B frequency generator at f_c = 100 kHz with external modulation signal from the lock-in amplifier (SR830, Stanford Research Systems) at f_m = 1.4342 kHz. The modulation index, m is generally kept at 1. The DC gate voltage, V_g^{DC} is provided via a NI-DAQ card and controlled by LabVIEW program. The output current is measured by the dc-coupled lock-in amplifier in the current mode at the modulated reference frequency. Hence, our input parameters are

$$V_s = \left|\tilde{V}^{\omega}\right|(1 + m\cos\omega_m t)\cos\omega_c t \qquad \text{Equation 3-16}$$

$$V_g = V_g^{DC}$$

$$V_d = 0\ .$$

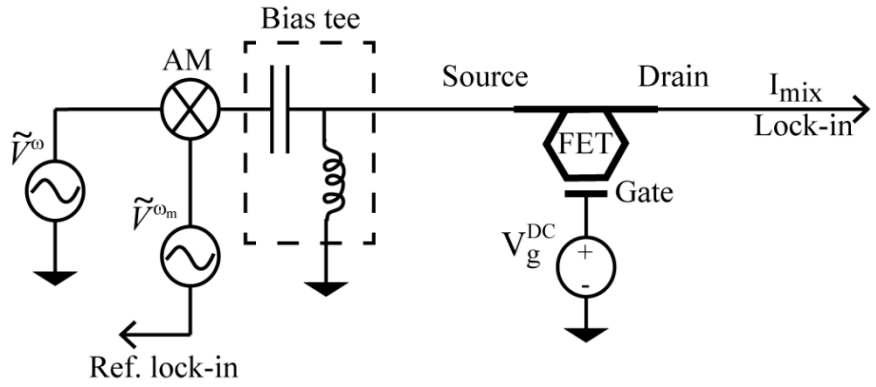

Figure 3-2. 'One-source' heterodyne mixing measurement setup [14], © Vera Sazonova, 2006. The source terminal is excited by an AM modulated frequency. The dc source and gate voltage are held at ground.

The background mixing-current term in Equation 3-12 can be further simplified using Equation 3-15 as

$$I_{mix} = \frac{dG}{dV_g^{DC}} \tilde{V}_g^{\omega} \tilde{V}^{\omega} = \frac{dG}{dV_g^{DC}} \left(-\frac{1}{2} \tilde{V}^{\omega} \right) \tilde{V}^{\omega} \, . \qquad \text{Equation 3-17}$$

The mixing current term for the setup shown in Figure 3-2 is given by Equation 3-6 except that for an AM modulated drive voltage, we measure the output at modulation frequency, ω_m instead of DC. Using Equation 3-16 for the applied AM voltage at the source terminal and using the trigonometric identity $2 \cos a \cdot \cos b = \cos(a+b) + \cos(a-b)$ we obtain a frequency mixed term at ω_m, given by

$$I_{mix}^{\omega_m} = -\frac{1}{2} m \frac{dG}{dV_g^{DC}} \left| \tilde{V}^{\omega} \right|^2 . \qquad \text{Equation 3-18}$$

From chapter 1, the $I-V$ relation for a carbon nanoelectronic FET is given by,

$$I_{sd} = \frac{\mu C_g}{L^2} \left(V_{g0} + \frac{V_{sd}}{2} \right) V_{sd} \, , \qquad \text{Equation 3-19}$$

where μ is the hole mobility, C_g is the gate capacitance, L is the channel length, V_{g0} is the gate overdrive voltage, and V_{sd} is the applied source voltage. From Equation 3-19 we have conductance G,

$$G = \frac{I_{sd}}{V_{sd}} = \frac{\mu C_g}{L^2}\left(V_g + \frac{V_{sd}}{2}\right) \qquad \text{Equation 3-20}$$

$$\therefore \frac{dG}{dV_g^{DC}} = \frac{\mu C_g}{L^2}\,. \qquad \text{Equation 3-21}$$

Now, background mixing current term from Equation 3-18 can also be written as

$$I_{mix}^{\omega_m} = -\frac{1}{2} m \frac{dG}{dV_g^{DC}} \left|\tilde{V}^{\omega}\right|^2 = -\frac{1}{2} m \frac{\mu C_g}{L^2} \left|\tilde{V}^{\omega}\right|^2 . \qquad \text{Equation 3-22}$$

In Figure 3-3, we compare experimental mixing current measurement results for a typical carbon nanotube FET to the theoretical expression of Equation 3-18. The mixing current, I_{mix} as a function of gate voltage V_g is plotted in red in Figure 3-3. Theoretical mixing current (▲, solid triangle) is also calculated using the measured DC transfer curve of nanotube FET (black). Differentiating the DC transfer curve gives us the transconductance $\frac{dG}{dV_g^{DC}}$. The measured I_{mix} trend agrees well with theory but the amplitude differs, which is attributed to dissipation due to circuit parasitics [14].

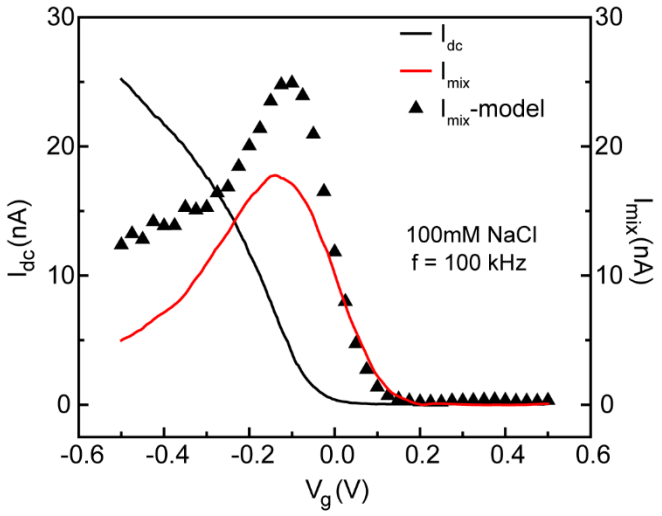

Figure 3-3. Mixing current of pristine carbon nanotube FET in 100mM NaCl background solution. The $I_{dc} - V_g$ characteristic is plotted in black for voltage V_{sd} = 10 mV. The measured I_{mix} as a function of V_g is plotted in red for drive parameters $\left|\tilde{V}^{\omega}\right|$ = 50mV, m = 0.78, $\omega_c/2\pi$ = 100 kHz and $\omega_m/2\pi$ = 1.4342 kHz. Theoretical I_{mix} obtained using Equation 3-18 is also shown (▲) for comparison.

The observed peak in Figure 3-3 is the point of maximum non-linearity in the gate response i.e. where slope $\frac{dG}{dV_g^{DC}}$ is maximum. The resistance of our device is much greater than the 50 Ω source drive impedance, therefore the actual drive amplitude is twice the applied value.

In Figure 3-4, we compare experimental mixing current measurement results for a typical graphene FET in air to the theoretical expression of Equation 3-18.

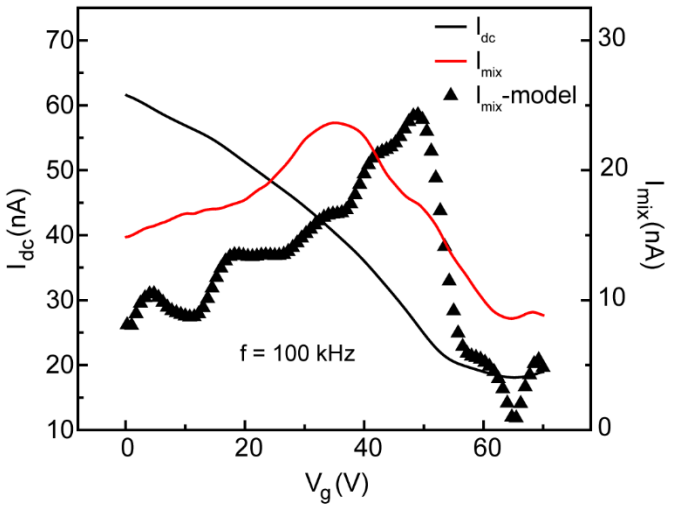

Figure 3-4. Mixing current of pristine graphene FET in air. The $I_{dc} - V_g$ characteristic is plotted in black for a source-drain voltage V_{sd} = 1 mV. The measured mixing current, I_{mix} as a function of V_g is plotted in red for drive parameters $\left|\tilde{V}^{\omega}\right|$ = 10mV, m = 1, $\omega_c/2\pi$ = 100 kHz and $\omega_m/2\pi$ = 1.4342 kHz. Theoretical I_{mix} obtained using Equation 3-18 with 40 dB amplifier gain is also shown (▲) for comparison.

In the following chapters, our focus however, will be on the first term in Equation 3-12,

$$I_{mix}^{\tilde{q}} = \frac{1}{C_g}\frac{dG}{dV_g^{DC}}\tilde{q}_{ext}\tilde{V}^{\omega}\,, \qquad \text{Equation 3-23}$$

which represents the heterodyne response of a sensor due to the presence of molecules in the immediate environment of the sensor surface.

3.5 Conclusion

In this chapter, we started with a description of the general theory behind the electrical detection techniques that are the basis of conventional chemical and biological nanoelectronic sensors. We also introduced a generic equation which describes the output response of any nanoelectronic sensor. Next, we introduced a new nanoelectronic sensing technology based on the principle of heterodyne mixing between two frequency signals; and derived the heterodyne mixing response term which compromises of both the background response from a pristine device as well as the response due to the presence of molecules near the sensor surface. Finally, we presented the measurement setup used to implement heterodyne detection in our carbon based nanoelectronic devices. In the following chapters, we will use this principle of heterodyne detection to build carbon nanotube biosensors and graphene vapor sensors.

References

[1] P. Horowitz, *The Art of Electronics* (Cambridge University Press, 1989).

[2] J. B. Hagen, *Radio-frequency electronics: circuits and applications* (Cambridge University Press, 1996).

[3] A. A. Maznev, K. A. Nelson, and T. A. Rogers, Optics Letters **23**, 1319 (1998).

[4] C. E. M. Strauss, Optics Letters **19**, 1609 (1994).

[5] V. Sazonova, Y. Yaish, H. Ustunel, D. Roundy, T. A. Arias, and P. L. McEuen, Nature **431**, 284 (2004).

[6] C. C. Wu and Z. Zhong, Nano Letters **11**, 1448 (2011).

[7] C.-C. Wu and Z. Zhong, Applied Physics Letters **99** (2011).

[8] I. Bargatin, E. B. Myers, J. Arlett, B. Gudlewski, and M. L. Roukes, Applied Physics Letters **86** (2005).

[9] R. A. Betty Anderson, *Fundamentals of Semiconductor Devices* (McGraw Hill, New York, 2005).

[10] K. K. N. Simon M. Sze, *Physics of Semiconductor Devices* (John Wiley and Sons, New Jersey, 2007).

[11] J. Appenzeller and D. J. Frank, Applied Physics Letters **84**, 1771 (2004).

[12] S. Rosenblatt, H. Lin, V. Sazonova, S. Tiwari, and P. L. McEuen, Applied Physics Letters **87**, 3, 153111 (2005).

[13] S. Rosenblatt, PhD Thesis, Cornell University, 2006.

[14] V. A. Sazonova, PhD thesis, Cornell University, 2006.

Chapter 4

Carbon nanotube heterodyne biosensor

4.1 Introduction

Carbon nanotubes, nanowires, graphene and molybdenum disulphide have dimensions which compare well with the length scales of biological species of interest for example viruses, proteins and DNA. Nanoelectronic systems based on these nanomaterials hence, provide a promising platform for extremely sensitive, real-time, point-of-care biological detection. However, one of the bottlenecks for on-field implementation of these systems is that the available nanoelectronic sensing technologies based on charge-detection fail in physiologically relevant conditions due to Debye screening effect (chapter 2). In this chapter, we demonstrate heterodyne detection of ligand-receptor binding on a carbon nanotube field-effect-transistor platform in high ionic background solutions. In heterodyne sensing, we detect biomolecular dipoles at high frequency rather than the associated charges. Further, heterodyne allows us to operate the sensor at frequencies high enough to overcome ionic screening, and yet detect the frequency mixed signals at lower frequencies.

The carbon nanotube device fabrication is described in Section 4.2. To implement solution based measurement, we sealed the devices with a microfluidic chamber, the preparation of which is detailed in Section 4.3. The electrical measurement setup for initial characterization of nanotube devices is presented in

Section 4.4. For biological detection, we first functionalized the carbon nanotube sidewalls with receptor molecules and then introduced the solution containing ligand molecules into the microfluidic chamber. The sidewall modification of the device is covered in Section 4.5. Next, we discuss the effects of high ionic strength backgrounds on conventional direct-current (DC) electrical measurements (Section 4.6) and demonstrate the heterodyne detection of ligand-receptor binding in high ionic backgrounds in Section 4.7. Finally, we theoretically estimate the heterodyne mixing contribution from biomolecules functionalized on the nanotube in Section 4.8.

4.2 Carbon nanotube field-effect-transistor fabrication

The carbon nanotube field-effect-transistors were fabricated in the Lurie Nanofabrication Facility at University of Michigan Ann Arbor. The process flow is shown in Figure 4-1. The transistors were designed to have a suspended top-gate terminal close to the nanotube. To implement this, we first grow a 500nm Si_3N_4/ 500nm SiO_2 film on a silicon wafer in a low pressure CVD furnace. Later on the nitride layer acts as the etch stop layer during wet etching to obtain suspended gate structures (Figure 4-1). For nanotube growth, we deposited a 0.5 nm thick iron (Fe) catalyst layer (particles) in an e-beam evaporation chamber, which acts the catalyst for CNT growth [1]. Ethylene gas is used as the carbon source for CVD growth of nanotubes [2]. An AFM image of as grown CNT is shown in Figure 4-2a. The nanotube growth parameters are described in detail in Appendix-A.

The source and drain electrical contacts are defined by photolithography and titanium/gold (0.5nm/50nm) metal layer is deposited in an e-beam evaporator. An atomic force microscope image of the carbon nanotube between source-drain electrodes is shown in Figure 4-2b.

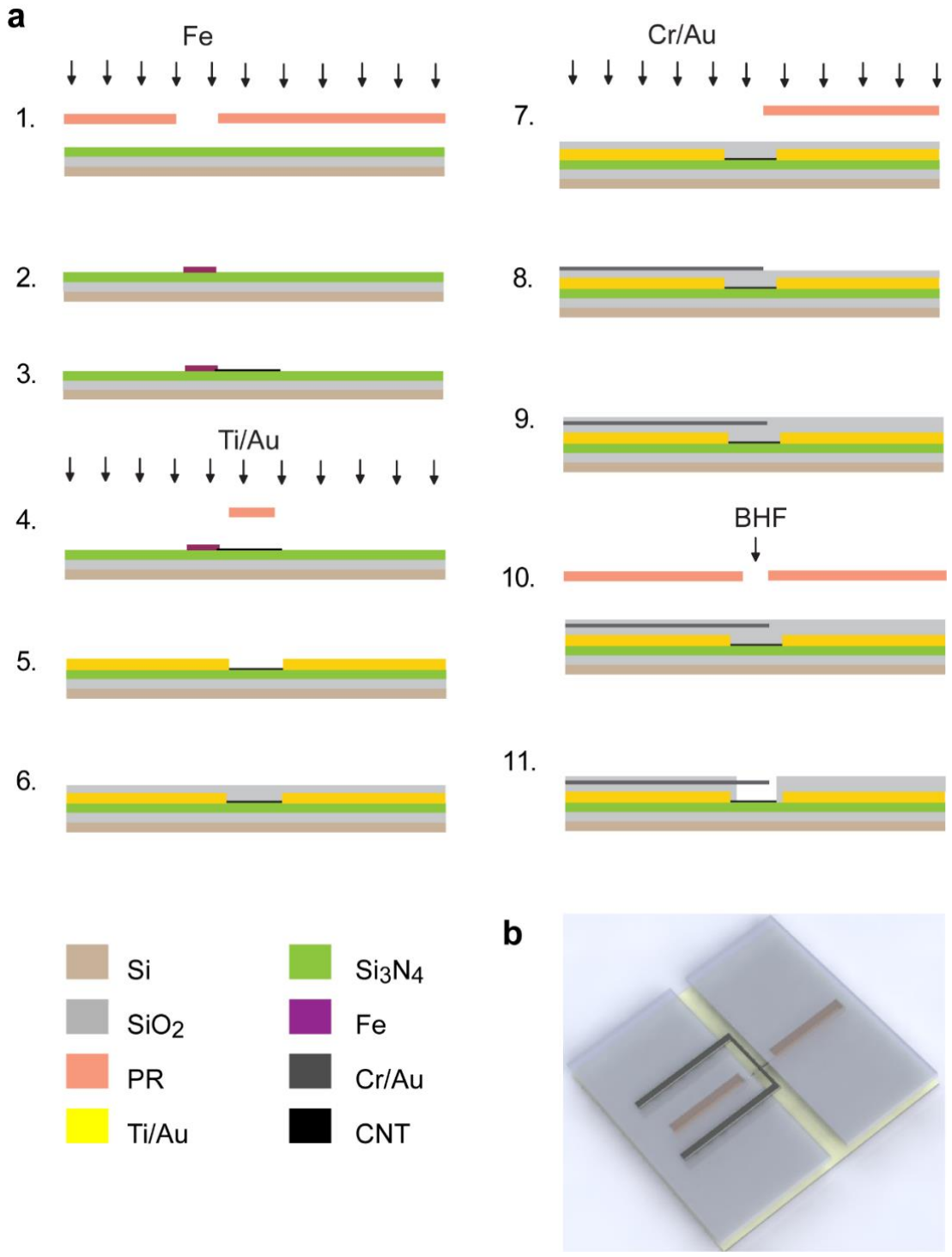

Figure 4-1. Nanotube transistor fabrication process flow. **(a)** Fabrication process – (1) photomask layer-1 (PL-1) for catalyst deposition, (2) metal liftoff, (3) CNT growth, (4) PL-2 for source-drain contact, (5) metal liftoff, (6) SiO_2 blanket deposition, (7) PL-3 for gate contact, (8) metal liftoff, (9) Thin SiO_2 blanket deposition, (10) PL-4 for BHF wet etch channel and (11) final device after photoresist removal. Color scheme is illustrated. **(b)** Schematic of device structure.

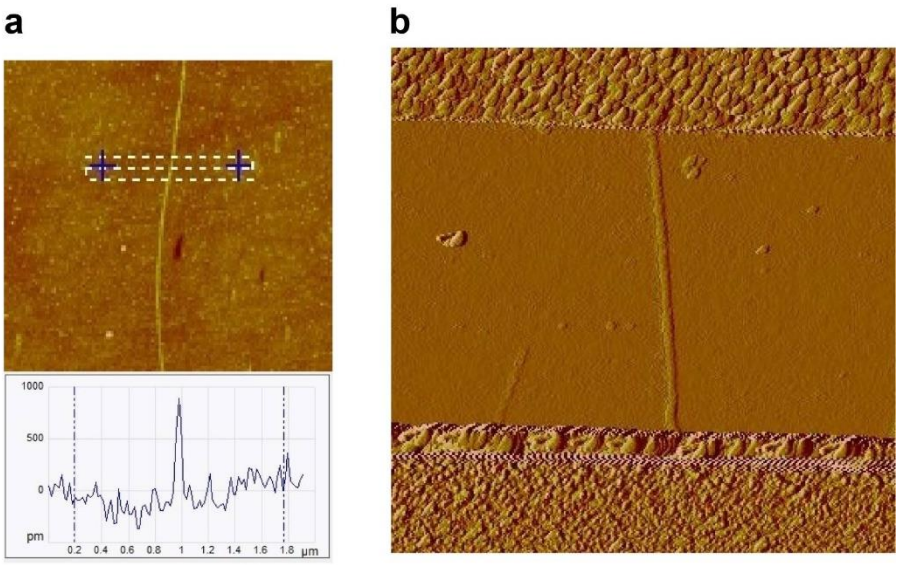

Figure 4-2. AFM image for single walled carbon nanotube after **(a)** growth and **(b)** metal deposition (2 μm × 2 μm scan). The diameter of the nanotube in (a) is around 0.8 nm which represents a single walled carbon nanotube.

We incorporate a suspended top gate [3] (Figure 4-1) placed 500nm above the carbon nanotube which enhances the sensor high frequency response and also allows for a compact microfluidic chamber to seal the die. For the suspended structure, we first blanket-deposit 500 nm thick layer of e-beam evaporated SiO_2. Then, the top gate metal is defined photolithographically and chrome/gold (50nm/50nm) metal layer is deposited. After a second passivation layer deposition of 20 nm SiO_2, we open a channel region by a 3 min 30 sec wet-etch of SiO_2 in 1:20 BHF solution. After the etch process, the die is rinsed in DI water bath. The photoresist mask is removed by immersing the die immediately into a solution of acetone and then IPA. A simple N2 blow dry process is adopted to dry of the IPA solution. The thick layer of chromium provides enough strength to the top gate structure to avoid collapse. A scanning electron microscope image of carbon nanotube transistor with a suspended top gate is shown in Figure 4-3a. The gate dimensions are critical for suspension [3]. The current

design dimensions are length × width × thickness = 25μm × 1μm × 100nm. The suspended structure is also confirmed by the absence of leakage current between top gate and drain (Figure 4-3b).

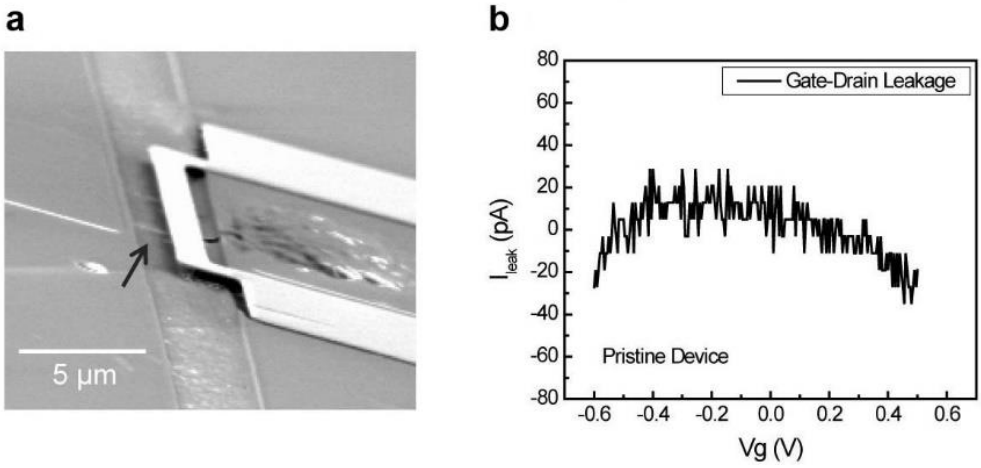

Figure 4-3. **(a)** SEM image of a typical suspended top-gate device, and **(b)** gate-drain leakage to confirm suspended structure. The etched channel is around ~ 4 μm wide.

4.3 Microfluidic chamber

We carry out all our solution measurements inside a microfluidic setup. For static (no-flow) measurements the devices are sealed with a polydimethylsiloxane (PDMS) chamber [4]. For real-time flow measurements, a microfluidic flow channel is incorporated on top the device with inlet and outlet ports [5]. Before placing the microfluidic stamp onto the die, we thoroughly rinse the die to remove contaminants from die processing steps, as they hamper the adhesion of PDMS stamp to the die. If the substrate is not clean, the PDMS stamp is not leak-tight and can peel off with fluid pressure during measurement. To assist the adhesion, a gentle O_2 plasma (15 sec) step was also carried out on the PDMS stamp. We observed that if the duration or power of O_2 plasma is increased, there is better adhesion however, it becomes hard to remove

the stamp from the device without ripping off the electrodes which rendered the die unusable. We do not use O_2 plasma on the SWNT device as this etches the carbon nanotubes. In the following sub-sections, we discuss the soft-lithography steps to fabricate the PDMS chamber and flow channel.

4.3.1 PDMS chamber (no-flow)

The PDMS chamber is constructed by punching a hole in a PDMS stamp. To make the stamp, we first mixed 9:1 ratio (by weight) of PDMS monomer and curing agent. Then, we degassed the mixture for 25 minutes, after which the mixture is poured over a clean silicon wafer kept in a Petri dish. Next, we cured the mixture at 70°C for 1 hour by placing the Petri dish in an oven. From this mold, a PDMS stamp of appropriate size to cap the die is cut out using a scalpel. The PDMS side directly in contact with the silicon wafer is clean and extremely flat. This side is placed in contact with the active area of silicon die and therefore, we punched the hole from the flat side to the other using a biopsy punch (3mm dia.). This ensured no rough edges and allowed better adhesion to the fabricated die. We have observed that a clean stamp forms a good leak tight chamber even without an oxygen plasma treatment on PDMS before stamping. We placed the stamp on the die using the naked eye. Figure 4-4a shows a schematic of the process and Figure 4-4b shows a diagrammatic representation of the entire sealed device.

4.3.2 PDMS flow channel

For fluid flow measurements, we incorporated a flow channel into the PDMS stamp using an SU-8 mold. The process flow is shown in Figure 4-4c. First, on a clean

silicon wafer, we spin-coated a 30 µm thick layer of SU-8 2015. Then, we photolithographically defined a 300 µm wide flow channel and develop the wafer to get the SU-8 negative mold for the flow channel (Figure 4-4c). The dimensions of the flow channel were in the ratio W: H = 10: 1. We placed the wafer with SU-8 mold in a vacuum desiccator along with 2-3 drops of silanizing agent trichloro (3, 3, 3-trifluoropropyl) silane in a petridish for an hour. Then, we poured the degassed PDMS mixture (Section 4.3.1) onto the wafer with SU-8 mold and cured it for 1 hour at 70°C. Next, a PDMS stamp of appropriate size over the mold area with flow channel was cut using a scalpel (Figure 4-4e). For fluid flow, inlet and outlet holes were punched at each end of the flow channel using a 0.75mm dia. biopsy punch. To seal the die, we placed the PDMS flow chamber on the device by carefully aligning the flow channel and the active area containing the carbon nanotube FET under a microscope. In order to get a robust PDMS stamp on the die, we used a gentle oxygen plasma treatment on the PDMS stamp. Once the stamp was secured on the die, we pushed a polyethylene tube (PE-50, 0.023 ID 0.038 OD) into the inlet/outlet holes and connected the other end to a fluid source and drain syringe. Figure 4-4d is a representative image of the flow channel on top of the device. Figure 4-4e shows the tube connections to the inlet and outlet ports.

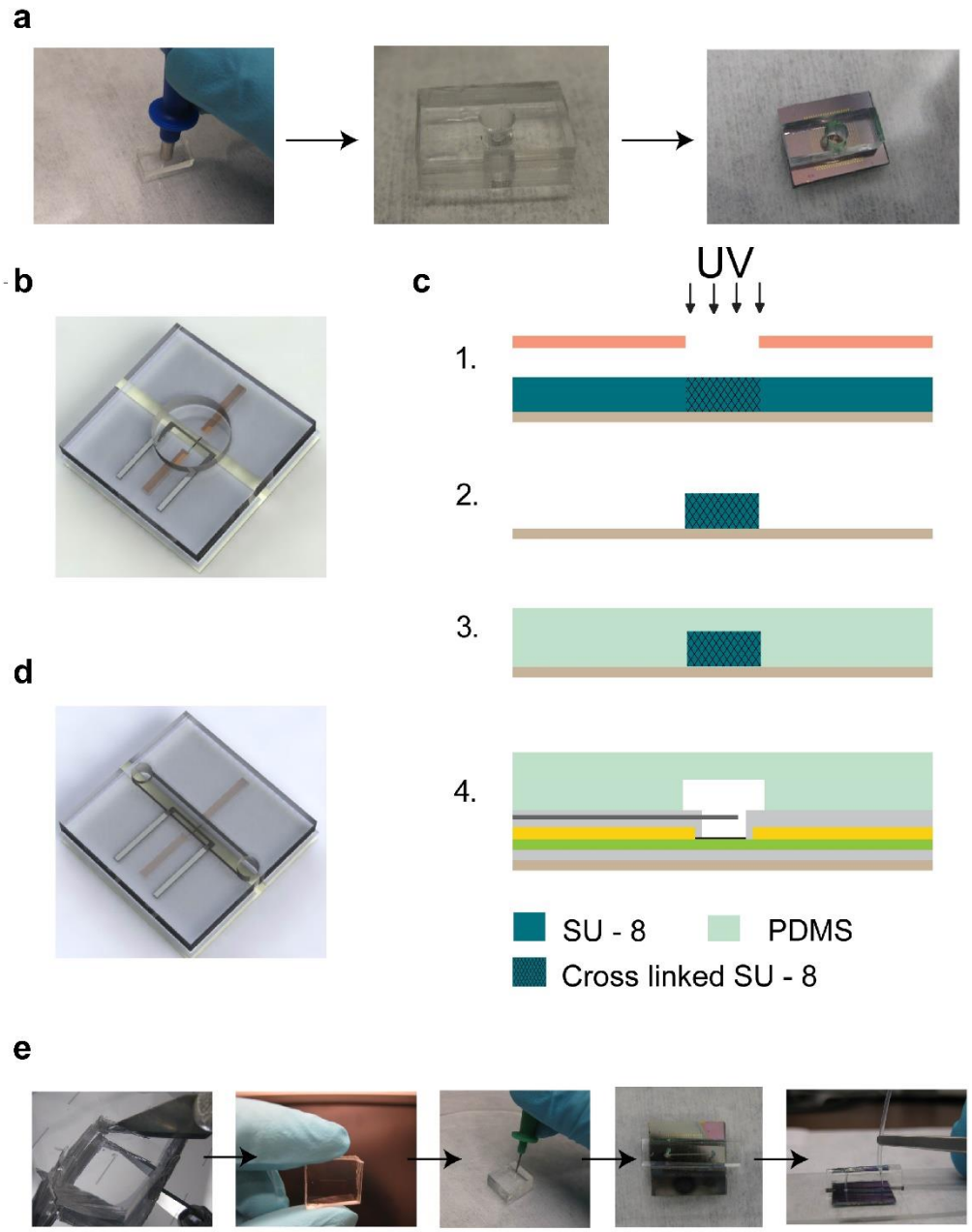

Figure 4-4. PDMS stamp for solution measurements for static (no flow) and flow measurements. **(a)** Punching and mounting a PMDS chamber on device, **(b)** schematic of flow chamber on a device. **(c)** Process flow for PDMS flow channel using SU-8 mold - (1) photomask for defining flow channel, (2) cross linked SU-8 mold, (3) PDMS on SU-8 and (4) PDMS flow channel stamped onto device. **(d)** Schematic diagram of flow channel on a device and **(e)** punching inlet/outlet holes in PDMS, stamping the flow channel on device and connecting polyethylene tubing to inlet/outlet ports.

4.4 Direct current (DC) electrical measurement setup

For the initial characterization of our nanotube transistors at different stages of fabrication and sidewall modification, we used the direct current (DC) setup show in Figure 4-5a.

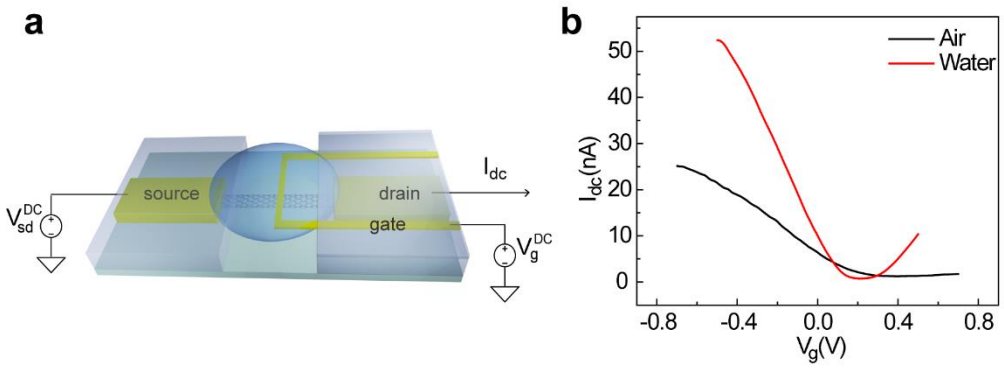

Figure 4-5. **(a)** DC electrical measurement setup **(b)** $I_{dc} - V_g$ curves for nanotube FET in air (black) and DI water (red).

The electronic instruments were controlled by a LabVIEW program, measureit-2.2 [6]. The source and gate voltages were applied through a DAQ card connected to a BNC connector box (National Instruments). The top gate voltage is swept and the output DC current is read at the drain terminal through the DAQ input ports via a DC pre-amplifier (DL-1211, Ithaca). Typical DC characteristic curves for a top-gated single walled carbon nanotube field effect transistor in air and DI water are shown in Figure 4-5b. The high permittivity of water (ε~80) enhances the gate capacitance, which leads to improved gate coupling as compared to an air gate (ε~1).

4.5 Sidewall functionalization of carbon nanotubes

We chose the biotin-streptavidin ligand-receptor system to evaluate the sensing capability of our carbon nanotube sensor in different background ionic strengths. The

first step for label-free detection is surface functionalization of the nanotube with receptor molecules. For sidewall modification, we followed the non-covalent scheme provided by Chen et al. [7]. First, the die was incubated in a solution of 6mM 1-pyrenebutanoic acid succinimidyl ester (PBSE) in dimethylformamide (DMF) for 1 hour at room temperature. After this, the die was thoroughly rinsed in DMF, to remove the unbound PBSE molecules from the substrate. PBSE is a non-covalent linker molecule, which π-stacks along the carbon nanotube sidewall (schematic shown in Figure 4-6). Since there is no chemical bond formation, the pristine electronic properties of the nanotube are preserved. For attaching the receptor to linker molecule, we biotinylated the nanotube by incubating the die in 20 mg/ml solution of biotinyl 3, 6 dioxaoctanediamine (Biotin PEO Amine - BPA) in DI water for 18 hours. After biotinylation step, the die was thoroughly rinsed with DI water.

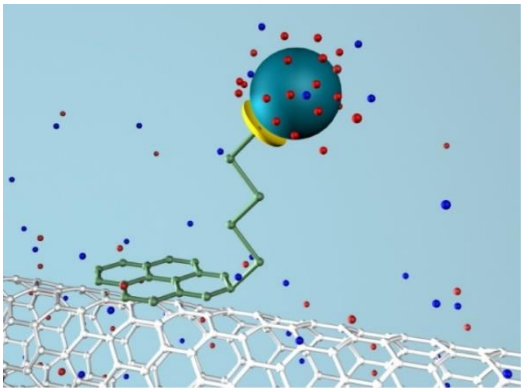

Figure 4-6. Schematic of a non-covalently functionalized nanotube in solution where a biomolecule π-stacks onto the sidewall of single walled carbon nanotube.

We carried out our sensing measurements both, in static (no-flow) as well as flow conditions. For both these measurements, we prepared a 1mg/ml streptavidin solution in 7.2 pH PBS. For the static measurement, the biotinylated die was incubated

in the streptavidin solution for 20 min to achieve the streptavidin-biotin binding. The die was thoroughly rinsed in DI water and then measured in different background ionic strength solutions. For real time sensing, after biotinylation the PDMS flow channel was placed on top of the die and streptavidin solution was introduced.

The success of sidewall modification at each step was confirmed by monitoring the DC transfer curves i.e. $I_{dc} - V_g$ characteristics in air at each stage of modification as shown in Figure 4-7a.

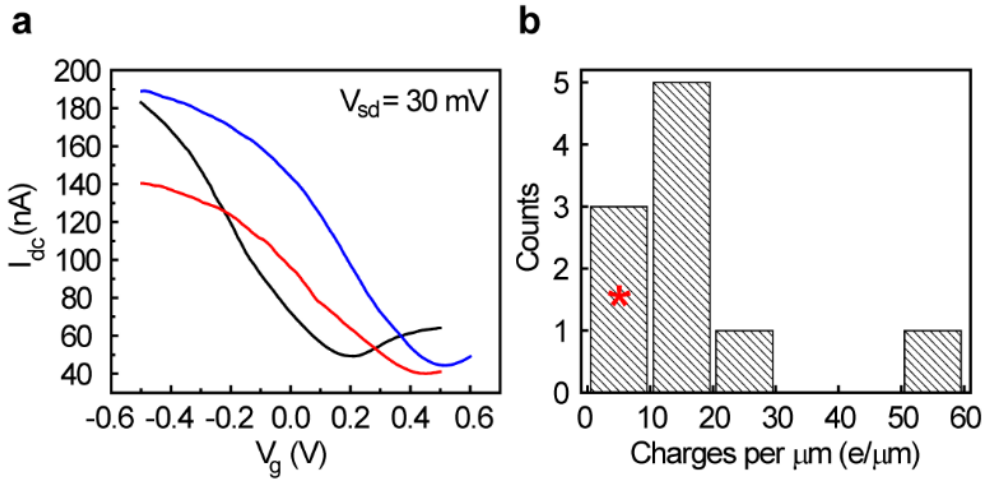

Figure 4-7. Threshold voltage shift of nanotube FET confirming successful nanotube sidewall functionalization. **(a)** $I_{dc} - V_g$ curve for pristine nanotube FET (black), after biotinylation (red) and after streptavidin binding (blue). Measurements are done in air. **(b)** Histogram of 10 devices for surface charge density induced after streptavidin binds to biotin. The device studied in Figure 4-7a, is marked with a *.

We observed that the transfer curve shift to the right after biotinylation (red) and streptavidin binding (blue). We attribute this to the electrostatic gating by the electronegative amine groups present on biotin PEO-amine and streptavidin [8]. The transfer curve shift is consistently observed among 10 devices, showing successful sidewall functionalization. A histogram of these devices is shown in Figure 4-7b for

change in surface charge density after streptavidin binds to biotin. From the shift in the Dirac point voltage ΔV, we can estimate the changes in 1D surface charge density of the nanotube after streptavidin binds to biotin as $Q' = C' \cdot \Delta V$. Using a wire on infinite plane model for the suspended gate, capacitance per unit length is $C' = \frac{2\pi\varepsilon_0}{\cosh^{-1}\frac{d}{r}}$, d is the distance of suspended gate electrode from the nanotube (500nm) and r is the radius of nanotube (~1 nm). For the device in Figure 4-7a, Q' ~ -3 e/μm. Measurements from 10 devices revealed that protein binding induces a surface charge density on the order of 10s of e/μm.

4.6 Debye screening effect

When a charged surface is present in a solution, the electric field emanating from the surface attracts counter ions from the solution. These counter-ions accumulate near the charged surface and in effect screen off the charges. The surface charge and counter ions form an electrical double layer [9], which in case of a metal electrode plate can be visualized as a simple parallel plate capacitor. To solve for the potential as a function of distance from the plate surface, we need to solve the Poisson equation:

$$\nabla^2\phi(\vec{x}) = \frac{\rho(\vec{x})}{\varepsilon\varepsilon_0}. \qquad \text{Equation 4-1}$$

Here, $\phi(\vec{x})$ is the potential at a distance x, $\rho(\vec{x})$ is the local charge density near the surface and $\varepsilon\varepsilon_0$ is the solution permittivity. Now, $\rho(\vec{x})$ is equal to the concentration of cations and anions near the surface $e\left(c^+(x) + c^-(x)\right)$. By assuming a Boltzmann distribution of the ions in potential $\phi(\vec{x})$, we can reframe Equation 4-1 as

$$\nabla^2\phi(\vec{x}) = -\frac{c_0 e}{\varepsilon\varepsilon_0}\left(e^{-e\phi(\vec{x})/k_BT} - e^{e\phi(\vec{x})/k_BT}\right), \qquad \text{Equation 4-2}$$

where c_0 is the bulk electrolyte concentration. To analytically solve this equation, we consider $\phi(x) < k_B T$. We can then use Taylor expansion to simplify the above equation to get

$$\nabla^2\phi(\vec{x}) = \frac{2c_0e^2}{\varepsilon\varepsilon_0 k_B T}\phi(\vec{x}). \qquad \text{Equation 4-3}$$

We define Debye screening length as, $\lambda_D = \sqrt{\frac{\varepsilon\varepsilon_0 k_B T}{2c_0e^2}}$ so we have,

$$\nabla^2\phi(\vec{x}) = \frac{\phi(\vec{x})}{\lambda_D^2}. \qquad \text{Equation 4-4}$$

The above equation yields an exponential decay function $\phi(\vec{x}) = \phi_0 e^{-x/\lambda_D}$ which is plotted for a monovalent ion solution of concentration 1mM, 10mM and 100mM in Figure 4-8.

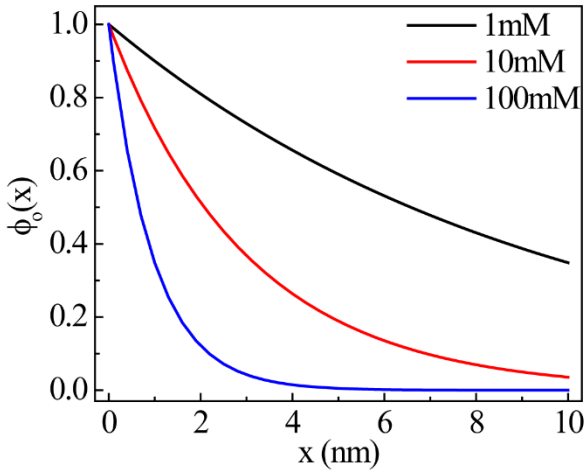

Figure 4-8. Normalized potential, $\phi(\vec{x})/\phi_0 = e^{-x/\lambda_D}$ plotted with distance from a charged surface.

For a typical 100 mM buffer solution, λ_D is around 1 nm and the surface potential is completely screened at a distance of a few nm. Label free biological detection is generally achieved by functionalizing the sensor surface with receptor

molecules, either through covalent or non-covalent binding [10,11]. The receptor molecules are themselves 3-5 nm in diameter, which puts the combined linker-receptor-ligand complex further away from the sensor surface (~10-12nm) [11]. In physiologically relevant conditions, the background ionic strength is ~ 100mM and ligand-receptor complex is completely screened from the surface and hence, conventional charge-detection techniques fail (Figure 4-9). As the result, most of existing nanoelectronic sensors operate either in dry state or in low ionic strength solutions (c ~ 1 nM – 10 mM) as detailed in chapter 2.

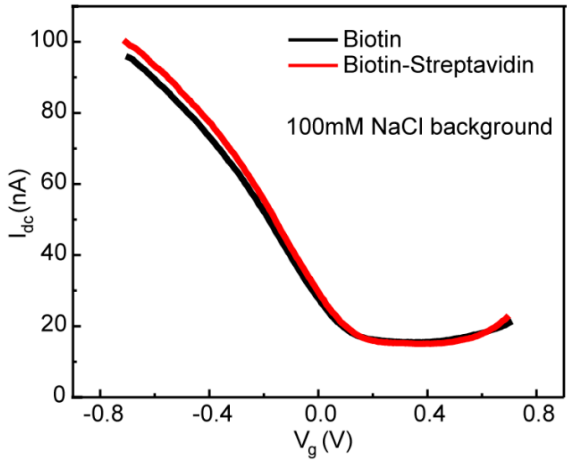

Figure 4-9. DC characteristics, $I_{dc} - V_g$ before and after streptavidin-biotin binding in 100 mM NaCl background solution.

4.7 Heterodyne detection in high ionic strength solutions

For heterodyne detection, we follow 'one-source' setup (chapter 3) shown in Figure 4-10. A high frequency signal ($\left|\tilde{V}^{\omega}\right|$ = 20 mV), AM modulated by a reference signal (1 V_{p-p}, f_m=1.4342 kHz), is fed to the source terminal of the FET. The mixing current is detected at the modulated frequency using a lock-in amplifier. The flowchart for heterodyne detection in static (no-flow) and flow conditions is shown in Figure 4-11.

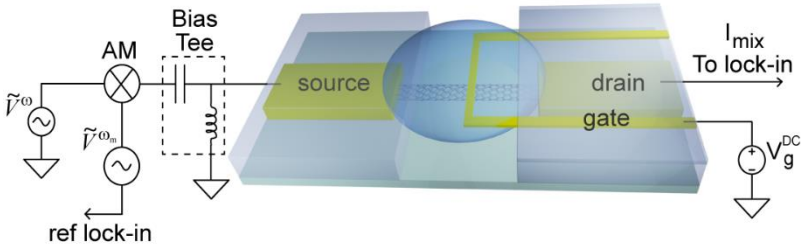

Figure 4-10. Heterodyne detection measurement setup.

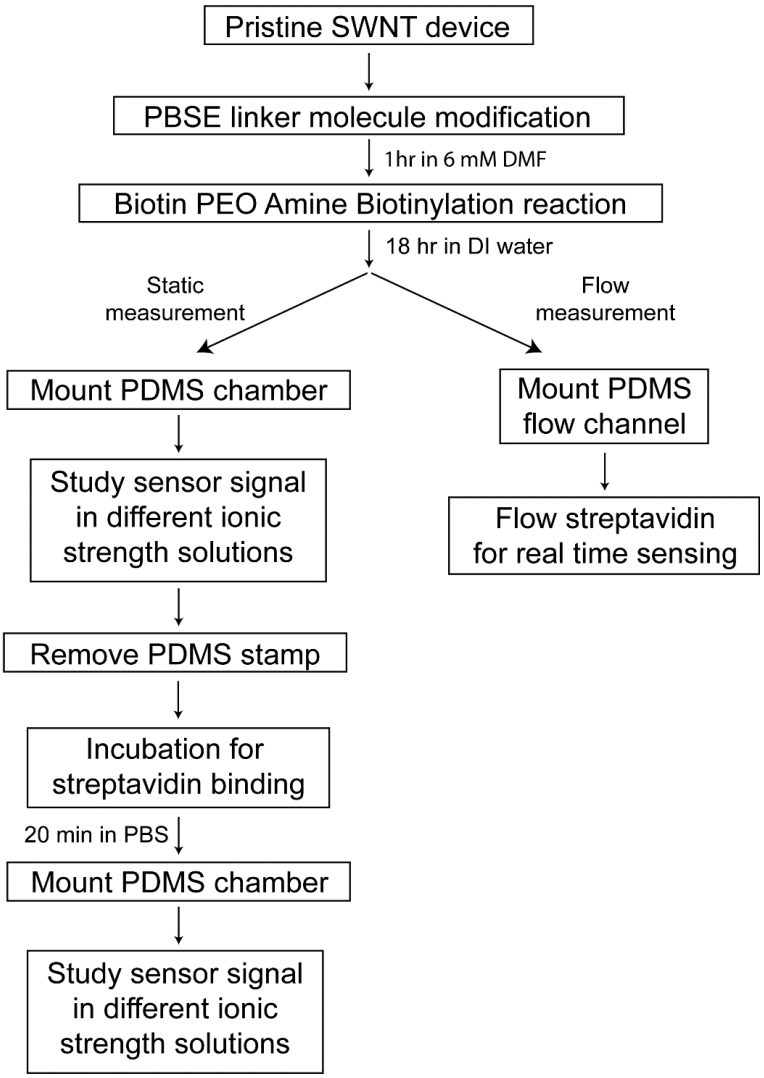

Figure 4-11. Flowchart for chemical functionalization and, static (no-flow) and fluid flow measurements.

4.7.1 Fluid chamber measurement

We first studied the nanotube sensor response in different background ionic strength solutions at relatively lower frequencies, f (200 kHz – 1 MHz). Figure 4-12a shows a comparison of $I_{mix} - V_g$ characteristics for the device in DI water at f = 500 kHz. We observed a large difference in I_{mix} before and after streptavidin binding, with mixing current peaks at V_g = -0.044 and -0.049 V, respectively. The peaks are also the point of maximum non-linearity in the $I_{mix} - V_g$ dependence. The frequency dependence (200 kHz – 1 MHz) of the peak mixing currents are also presented in Figure 4-12b, and substantial changes in I_{mix} before and after streptavidin binding were observed in DI water. As we increased the background NaCl concentration to 1 mM (Figure 4-12c) and 10 mM (Figure 4-12d) differences in I_{mix} before and after streptavidin binding were still visible but smaller than in DI water. Interestingly, when we increased the background salt concentration to 100 mM (Figure 4-12e), the changes in I_{mix} were no longer visible.

The observed differences of sensor's low frequency responses in various background ion concentrations is explained by the ionic screening effect [10,11]. The functionalized biomolecules are typically 5-10 nm away from the nanotube surface, which is within or comparable to the Debye lengths in DI water and 1 mM NaCl solution (Figure 4-12c, inset). Hence, in low ionic strength solutions, the biomolecular dipole can still gate the carbon nanotube, and the mixing current response can be used to detect the binding event. As the buffer concentration is increased to 10 mM NaCl (λ_D ~ 3 nm), the change in the sensing signal become weaker. Finally, at 100 mM NaCl concentration, Debye length drops to ~1 nm and no change is observed because

the streptavidin-biotin complex is completely screened away from the nanotube (Figure 4-12e, inset).

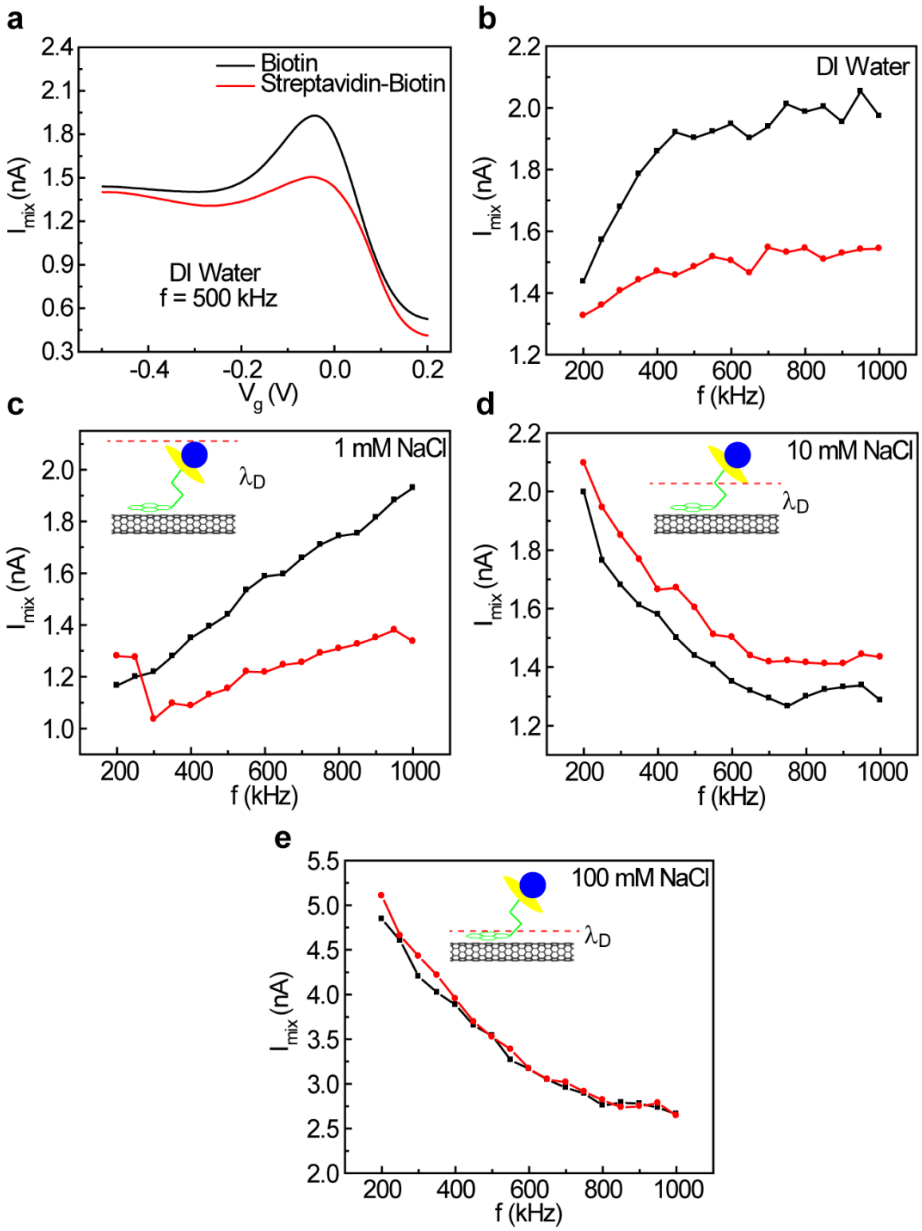

Figure 4-12. Ionic screening effect observed at DC and low frequency. **(a)** $I_{mix} - V_g$ for biotinylated SWNT sensor (black) and streptavidin-biotin bound SWNT sensor (red) in DI water at 500 kHz. Peak values of I_{mix} are plotted over frequencies range of 200 kHz – 1 MHz for biotinylated SWNT (black) and streptavidin-biotin bound SWNT (red) in **(b)** DI water, **(c)** 1 mM NaCl, **(d)** 10 mM NaCl, and **(e)** 100 mM NaCl as background solutions. Insets in (c), (d) and (e) illustrate Debye length in each case compared to the biomolecule separation from the sensor surface.

To mitigate the fundamental ionic screening effect in high ionic strength solution, we operate our carbon nanotube FET sensors at higher frequencies [12,13]. Figure 4-13a, b show the $I_{mix} - V_g$ characteristics of the same device at f = 500 kHz and 10 MHz, respectively, before and after streptavidin binding. At 500 kHz, nanotube sensor cannot pick-up the difference between before and after streptavidin binding. Remarkably however, it recovered its sensitivity when operating at 10 MHz. We also measured the peak values of frequency dependent I_{mix} for the device in 100 mM NaCl solution from 800 kHz – 30 MHz (Figure 4-13c). Both amplitude and phase signal of I_{mix} suggest that the nanotube sensor recovered its sensitivity at f > 1 MHz.

We further calculated the relative sensitivity, defined as the change in I_{mix} after streptavidin binding, divided by the mixing current before binding, $\Delta I_{mix}/I_{mix}$ (Figure 4-13d). Up to 25 % change in sensing signal was observed at f = 10 MHz. In Figure 4-13e, we plot the change in I_{mix} before and after streptavidin binding with different background ionic concentrations. We observe that at high frequency, the sensor response is enhanced compared to low frequencies and becomes independent of background ionic concentration. At low frequency, the sensor response shows a logarithmic dependence on background ionic concentration (solid line fit in Figure 4-13e) which has been reported previously in nanowire biosensors as well and is attributed to Debye screening by the electrostatic double layer (EDL) [14].

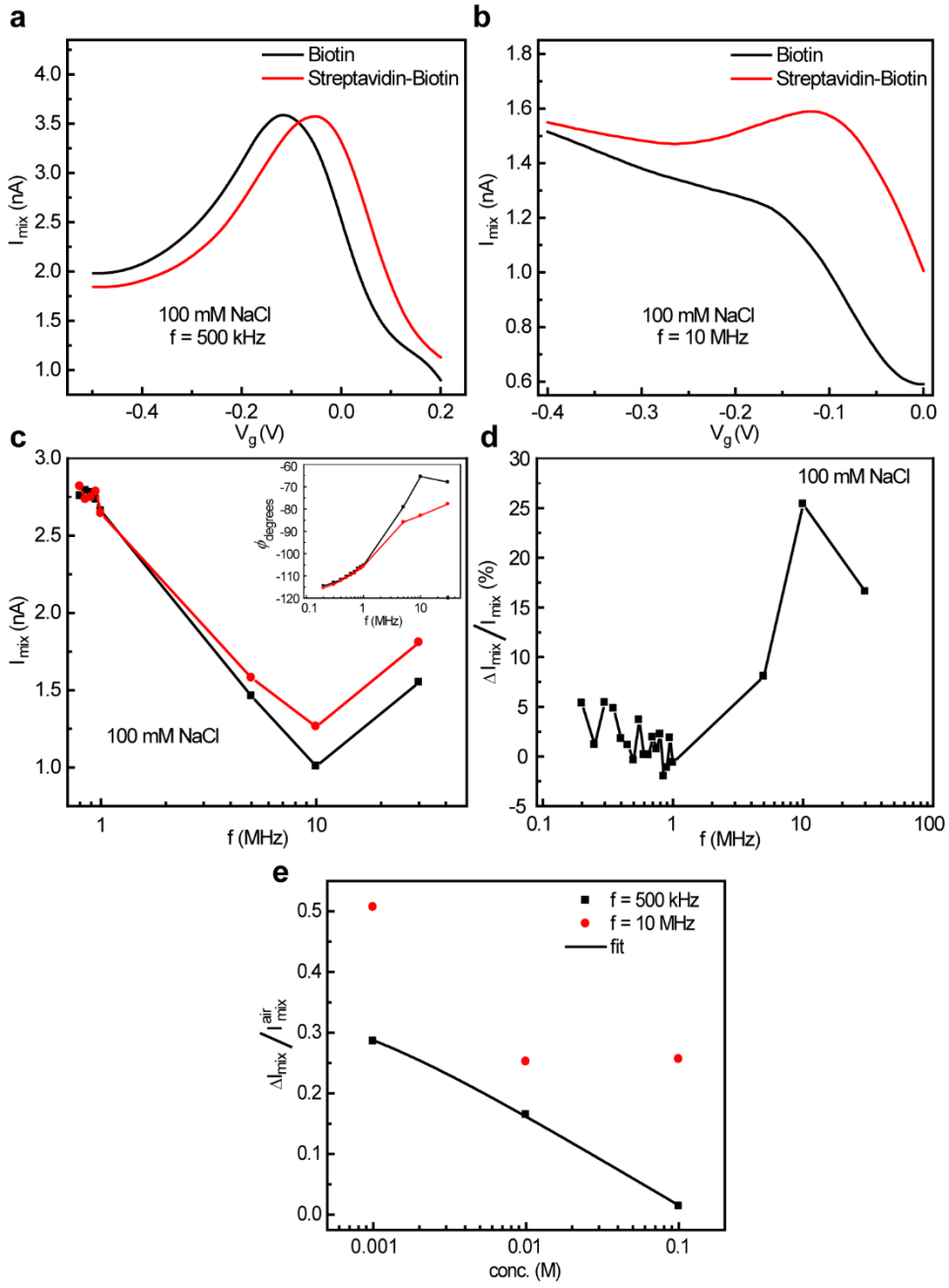

Figure 4-13. High frequency sensing mitigates the ionic screening effect and recovers the sensor sensitivity. $I_{mix} - V_g$ curves for biotinylated (black) and streptavidin-biotin bound (red) SWNT in 100 mM NaCl at **(a)**, f = 500 kHz (peak at V_g = -0.117 V and -0.053 V, respectively) and **(b)**, f = 10 MHz (peak at V_g = -0.186 V and -0.122 V, respectively). **(c)** The peak values of I_{mix} are plotted from 800 kHz – 30 MHz for both before (black) and after streptavidin binding (red) in 100 mM NaCl. Inset: Frequency dependent phase information of I_{mix}. **(d)** Relative sensitivity, $\Delta I_{mix}/I_{mix}$ of high frequency SWNT sensor (in percentage) as a function of f. **(e)** Sensor response with varying background ionic strength at f = 500 kHz (■) and f = 10 MHz (●). The solid line is the logarithmic fit to the experimental data at f = 500 kHz.

The recovery of sensitivity at high frequency can be explained by the breakdown of the EDL [13]. Importantly, when a high frequency oscillatory signal is applied, the ions in solution experience a lag due to their finite diffusivity and are unable to follow the excitation field. The first and second adsorbed water layers at the interface undergo molecular relaxation to weaken the EDL capacitor. Therefore, with increasing frequency, the screening decreases and AC electric field penetrates deeper into the solution. This electric field, although attenuated and phase shifted, can now drive the dipoles of the streptavidin-biotin complex. The fluctuating dipoles in turn gate the nanotube causing a charge density modulation in it. This mixes with the AC drive voltage at source terminal to generate a mixing current response which is greater than the screening limited response at low frequencies (Figure 4-13e). Typical relaxation time in EDL has been estimated [13] to be $10^{-7} \leq \tau_0 \leq 10^{-5}$, which agrees qualitatively with our observed MHz sensitivity-recovery frequency.

To confirm that the signal change arises from the binding of streptavidin to the biotinylated surface of the device, and not due to capacitive effects, we also do a control experiment on fully passivated devices which shows no significant signal change after streptavidin injection in DI water Figure 4-14a and in 100mM NaCl in Figure 4-14b.

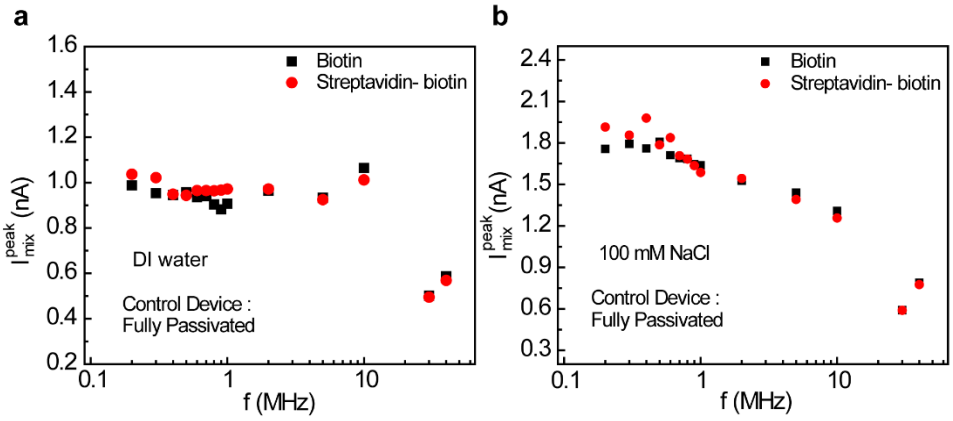

Figure 4-14. Mixing current signal before (■) and after (●) streptavidin binding on control devices with passivated SWNT channel and metal electrodes in **(a)** DI water, and **(b)**100mM NaCl.

4.7.2 Flow measurements

For point of care diagnosis, the sensors need to function at patient site in real-time and physiologically relevant conditions. To test the capability of our frequency mixing schematic in practical conditions we conducted flow measurements to detect streptavidin-biotin binding in real-time. For the fluid flow measurement, we sealed the device with the flow channel (Figure 4-4d), and connected the inlet tube to an empty syringe-barrel and the outlet tube to a syringe pump [15]. We operated the pump in withdrawal mode in order avoid back pressure created by air gaps which impeded fluid flow. An optical image of the fluid flow arrangement is shown in Figure 4-15. In flow measurements in 100mM NaCl background ionic solution also, we observed a change in mixing signal once streptavidin binds to biotin, proving the effectiveness of heterodyne technique (Figure 4-16).

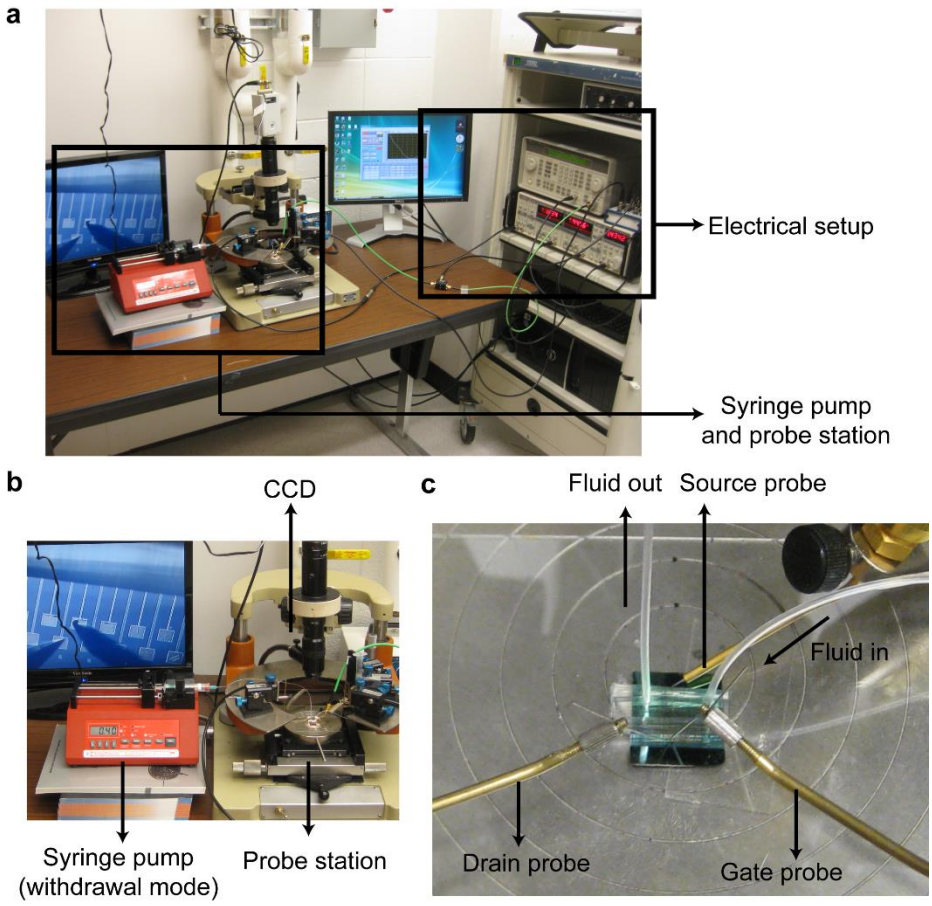

Figure 4-15. Flow measurement setup. **(a)** Image of entire measurement setup; **(b)** Syringe pump and probe station; and **(c)** blow up of device with PDMS flow channel, inlet/outlet flow tubes and electrical probes.

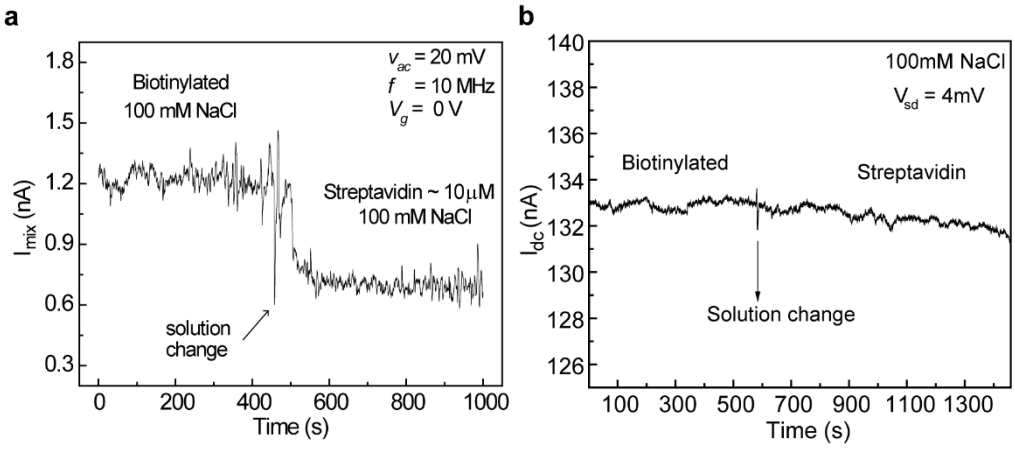

Figure 4-16. Real-time flow measurement to detect biotin-streptavidin binding in 100mM NaCl background using **(a)** heterodyne detection and **(b)** conventional DC current, I_{dc} detection technique.

4.8 Heterodyne mixing contribution from bio-molecules

In this section, we derive a general expression to determine the contribution of the biomolecules to heterodyne mixing current term. In Chapter 3, we illustrated that heterodyne detection term has two components, one from the background gate non-linearity and second from any charge density modulation caused by molecules in the local environment. This is given by Equation 3-12

$$I_{mix} = \frac{1}{C_g}\frac{dG}{dV_g^{DC}}(\tilde{q}_{ext} + C_g\tilde{V}_g^{\omega})\tilde{V}^{\omega}. \qquad \text{Equation 3-12}$$

Here, we derive an expression for the contribution from biomolecules, given by the first term in the above equation. First, we consider a 1D array of dipoles at distance of h nm above the nanotube as shown in Figure 4-17. For simplicity, we assume all dipoles point up in the unperturbed state.

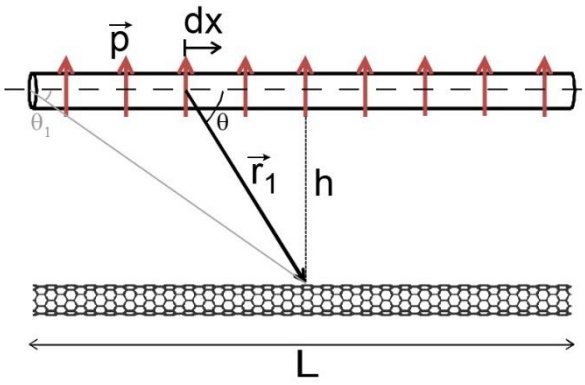

Figure 4-17. Modeling the high frequency carbon nanotube FET sensor. A 1-D array of biomolecules with dipole moment *p*, *h* nanometer above the nanotube surface.

Let n be the 1D dipole density per unit length, then the potential due to the dipole element dx can be written as

$$d\phi = \frac{n\hat{r_1}\cdot\vec{p}dx}{4\pi\varepsilon r_1^2} = -\frac{np\sin\theta\, dx}{4\pi\varepsilon r_1^2}. \qquad \text{Equation 4-5}$$

Using $\frac{dx}{\cos\theta} = dr_1$; $\sin\theta = \frac{h}{r_1}$ and therefore $\cos\theta \cdot d\theta = -\frac{hdr_1}{r_1^2}$, we have

$$d\phi = \frac{np\sin\theta\cos^2\theta}{4\pi\varepsilon h}d\theta. \qquad \text{Equation 4-6}$$

To obtain the surface potential induced by the 1D dipole array, we integrate Equation 4-6 over the length of the nanotube,

$$\phi = \int_{\theta_1}^{\pi-\theta_1} \frac{np\sin\theta\cos^2\theta}{4\pi\varepsilon h}d\theta = \frac{1}{3}\frac{2np\cos^3\theta_1}{4\pi\varepsilon h}. \qquad \text{Equation 4-7}$$

Since, $L/2$ (μm) >> h (nm), we have $\phi = \frac{1}{3}\frac{2np}{4\pi\varepsilon h}$.

As we increase the probing frequency, the EDL weakens and the drive field excites the bio-molecular dipoles located above nanotube. The fluctuating dipoles now act as a local gating potential. We assume that the molecular dipoles are perturbed at the same frequency, $f_c = \frac{\omega_c}{2\pi}$ as the AC drive voltage. When the ionic strength of the solution is high, e.g. 100 mM NaCl (λ_D ~ 1 nm), we can assume that the biomolecules are within the bulk solution and experience the bulk electric driving force. The bulk field can be related to the drive voltage through an attenuation and phase factor, γ and θ respectively [16]. From here, we estimate the local gating potential of the dipole array to be,

$$\Delta\tilde{V}_g = \gamma\phi\cos(\omega_c t + \theta). \qquad \text{Equation 4-8}$$

γ (≤ 1) represents the strength of the dielectric screening and θ represents the phase lag in the dipole response and both are dependent of bulk liquid parameters.

Now, Equation 3-12 is simplified using Equation 3-21, $\frac{dG}{dV_g^{DC}} = \frac{\mu C_g}{L^2}$ to get

$$I_{mix} = \frac{\mu}{L^2}\tilde{q}_{ext}\tilde{V}^{\omega}. \qquad \text{Equation 4-9}$$

Now, we can estimate the charge modulation from $\tilde{q}_{ext} = C'_m L \Delta\tilde{V}_g$ where C'_m is the capacitance per unit length due to a 1-D array of biomolecules on the nanotube and $\Delta\tilde{V}_g$ is gating potential due to oscillating dipoles given by Equation 4-8. Hence, we have

$$I_{mix} = \frac{\mu C'_m}{L} \Delta\tilde{V}_g \tilde{V}^{\omega}. \qquad \text{Equation 4-10}$$

Using the expression for AM modulated source voltage from Equation 3-16 and Equation 4-8 in the above equation, we get

$$I_{mix} = \frac{\mu C'_m}{L} \gamma\phi \cos(\omega_c t + \theta) \cdot \left|\tilde{V}^{\omega}\right| \Big(\cos\omega_c t + \frac{m}{2}\cos(\omega_c - \omega_m)t + \frac{m}{2}\cos(\omega_c + \omega_m)t \Big). \qquad \text{Equation 4-11}$$

Now, using trigonometric identity, $2\cos a \cdot \cos b = \cos(a+b) + \cos(a-b)$ in the above expression gives us a mixing current term at ω_m given by

$$I_{mix}^{\omega_m} = \frac{m}{2}\frac{\mu C'_m}{L}\gamma\left|\tilde{V}^{\omega}\right|\phi\cos\theta. \qquad \text{Equation 4-12}$$

In order to get some quantitative results from the above equation, we estimate the capacitance, attenuation and phase factors. Here, the capacitance per unit length C'_m is between the 1D array of dipoles and the carbon nanotube. The capacitance between two cylinders of radii, 'a' and 'b' which are separated by distance h, is $C'_m = \frac{2\pi\varepsilon}{\log(x+\sqrt{x^2-1})}$ where $x = abs\left(\frac{D^2-a^2-b^2}{2ab}\right)$ and $D = h + a + b$. Here, $a = r$ (nanotube radius) and is taken as 1 nm; b (streptavidin radius) is 2.5 nm and h is 5 nm [17]. For the model, we assume a nanotube mobility μ = 1 $m^2V^{-1}s^{-1}$, which is acceptable for a good single-walled nanotube device. For attenuation and phase lag, we refer to the theoretical model in Ref [16] for a case of bulk liquid between two parallel plate electrodes. Assuming that bulk liquid in our case is formed by the top gate electrode and the nanotube (separation d = 500nm), attenuation and phase factor can be

accounted for, to a decent approximation, by the same equations derived for two parallel plate electrodes,

$$\gamma = \frac{\Omega}{\sqrt{\Omega^2+4}} \qquad \text{Equation 4-13}$$

$$\theta = \tan^{-1}\frac{2}{\Omega}\ , \qquad \text{Equation 4-14}$$

where $\Omega = \frac{\omega d}{D\kappa}$ and ω is the applied carrier frequency, d is the separation between top gate electrode and nanotube (500nm), D is the ion diffusion coefficient (of the same order ~10^{-9} m^2 s^{-1} for Na^+ and Cl^-, from CRC handbook) and κ is the inverse Debye length. Clearly, if we go to very high frequencies, we have $\gamma = 1$ and $\theta = 0°$.

Figure 4-18a shows the calculated mixing current contributions in a 100mM ionic background from an array of biotin ($|\vec{p}|$ = 5.4D [18]) and streptavidin-biotin complex ($|\vec{p}|$ = 15.72D [18]) as a function of distance from the sensor surface using Equation 4-12 at high enough frequencies where ionic screening is overcome. At such a condition, attenuation factor $\gamma = 1$ and phase lag, $\theta = 0°$.

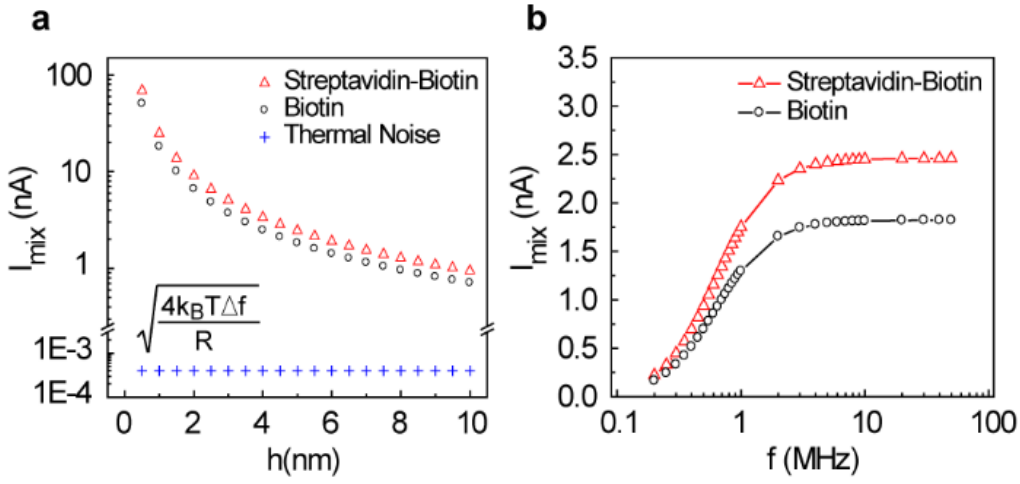

Figure 4-18 **(a)** Calculated I_{mix} due to a 1-D dipole array of biotin (○) and streptavidin-biotin complex (Δ), versus distance from the sensor surface. Thermal noise floor (+) is calculated using the device resistance from Figure 4-7. **(b)** I_{mix} vs f from our model with biotin and streptavidin-biotin complex at distance h = 5nm from the sensor surface.

We observe that as biomolecule moves farther away from the sensor surface, the mixing signal drops roughly as 1/distance (compared to the exponential decay when ionic screening is present). In Figure 4-18b, we plot the mixing current dependence on frequency taking into account the attenuation and phase factor. As the frequency increases we see a distinguishable change in mixing currents before and after streptavidin binding. At higher frequencies, the weaker double layer leads to smaller attenuation and phase lag and helps recover difference in I_{mix} between the two cases.

In a real operating environment, we also have to deal with the noise fluctuations in the device response. From our device characteristics in Figure 4-7, we find the thermal noise floor to be ~ 0.4 pA (Figure 4-18a); the $1/f$ noise is also negligible at our probing frequencies. Hence, our theoretical model supports our premise of high-frequency heterodyne sensing technique being capable of detecting ligand-receptor binding event on sensor surface even in 100 mM ionic strength solution.

4.9 Conclusions and future work

In this chapter, we described the fabrication of suspended top-gate carbon nanotube FETs, application of a microfluidic seal for liquid measurements, and demonstration of heterodyne detection of streptavidin-biotin binding on the carbon nanotube sensor platform in high ionic strength background. We carried out our experiments in both, static (no-flow) and fluid-flow conditions. We also built a qualitative model to estimate the induced potential due to a 1-D array of biomolecules on the nanotube in solution at high frequencies. The experimental results presented in this chapter demonstrate the successful mitigation of fundamental Debye screening effect. Recently, other groups have also addressed this issue [19,20], however, these

methods are much involved and require complex fabrication for on chip de-salting or engineering of receptor molecules.

Our theoretical model suggests the capability of heterodyne detection up to 100s of MHz drive frequency, however, we observed that the signal strength drops dramatically after ~ 40-50 MHz, which we believe is due to the resonance loss from measurement setup as well as the overwhelming background water dipole. This warrants the need for further study in improving the device operational bandwidth to achieve the maximum potential of high frequency biosensors. The sensitivity of the high frequency nanotube FET sensor can be improved by device optimization and reducing setup parasitic. I_{mix} depends on dipole gating potential (ϕ) and device transconductance ($\frac{dG}{dV_g}$). ϕ can be increased by choosing shorter linker molecules and by increasing the receptor coverage to increase the dipole density. The transistor gain can be enhanced by choosing single-walled carbon nanotubes with better device characteristics.

References

[1] J. Kong, H. T. Soh, A. M. Cassell, C. F. Quate, and H. J. Dai, Nature **395**, 878 (1998).

[2] C. C. Wu and Z. Zhong, Nano Letters **11**, 1448 (2011).

[3] G. Liu, J. Velasco, Jr., W. Bao, and C. N. Lau, Applied Physics Letters **92** (2008).

[4] D. C. Duffy, J. C. McDonald, O. J. A. Schueller, and G. M. Whitesides, Analytical Chemistry **70**, 4974 (1998).

[5] B. H. Jo, L. M. Van Lerberghe, K. M. Motsegood, and D. J. Beebe, Journal of Microelectromechanical Systems **9**, 76 (2000).

[6] V. A. Sazonova, PhD thesis, Cornell University, 2006.

[7] R. J. Chen, Y. G. Zhang, D. W. Wang, and H. J. Dai, Journal of the American Chemical Society **123**, 3838 (2001).

[8] I. Heller, A. M. Janssens, J. Mannik, E. D. Minot, S. G. Lemay, and C. Dekker, Nano Letters **8**, 591 (2008).

[9] L. R. F. Allen J. Bard, *Electrochemical Methods: Fundamentals and Applications* (John Wiley and Sons, New York, 2000).

[10] S. Sorgenfrei, C.-y. Chiu, M. Johnston, C. Nuckolls, and K. L. Shepard, Nano Letters **11**, 3739 (2011).

[11] E. Stern, R. Wagner, F. J. Sigworth, R. Breaker, T. M. Fahmy, and M. A. Reed, Nano Letters **7**, 3405 (2007).

[12] Z. J. Han, R. Morrow, B. K. Tay, and D. McKenzie, Applied Physics Letters **94** (2009).

[13] J. O. Bockris, E. Gileadi, and K. Muller, Journal of Chemical Physics **44**, 1445 (1966).

[14] P. R. Nair and M. A. Alam, Nano Letters **8**, 1281 (2008).

[15] G. F. Zheng, F. Patolsky, Y. Cui, W. U. Wang, and C. M. Lieber, Nature Biotechnology **23**, 1294 (2005).

[16] K. Kang and J. K. G. Dhont, Soft Matter **6**, 273 (2010).

[17] K. Bradley, M. Briman, A. Star, and G. Gruner, Nano Letters **4**, 253 (2004).

[18] J. DeChancie and K. N. Houk, Journal of the American Chemical Society **129**, 5419 (2007).

[19] R. Elnathan, M. Kwiat, A. Pevzner, Y. Engel, L. Burstein, A. Khatchtourints, A. Lichtenstein, R. Kantaev, and F. Patolsky, Nano Letters **12**, 5245 (2012).

[20] V. Krivitsky, L.-C. Hsiung, A. Lichtenstein, B. Brudnik, R. Kantaev, R. Elnathan, A. Pevzner, A. Khatchtourints, and F. Patolsky, Nano Letters **12**, 4748 (2012).

Chapter 5

Graphene heterodyne vapor sensor

5.1 Introduction

Rapid and in situ analysis of volatile organic compounds (VOCs) is of importance in a variety of fields like defense, industrial safety, homeland security, healthcare and environmental-monitoring [1-4]. Nanoelectronic sensors are ideal candidates for such on-site vapor monitoring applications due to their small size and low power operation. However, conventional nanoelectronic sensing technologies based on charge-detection mechanism suffer from speed-sensitivity tradeoff (chapter 2), which not only precludes studying the rapid dynamics of molecule–nanomaterial interaction, but also significantly hinders employment of nanoelectronic sensors in applications like gas chromatography (GC), which require detection capability for a broad range of vapor analytes with sub-second response time and ppb-level sensitivity. In this chapter, we demonstrate high speed and high sensitivity detection of a range of vapor analytes by exploring the heterodyne mixing characteristics of pristine, non-functionalized graphene field-effect-transistors.

We discuss the details of graphene FET fabrication, vapor delivery system, and DC electrical measurement setup in Sections 5.2, 5.3 and 5.4 respectively. In Section 5.5 we discuss the drawbacks of DC measurement in vapor sensing. In Section 5.6, we demonstrate heterodyne detection of chemical vapors on a graphene FET and present

the figure-of-merit for our graphene sensors. Next, we discuss (Section 5.7) the mechanism behind heterodyne vapor detection, where we conclusively prove that it is a dipole detection based mechanism. We build a theoretical model to calculate the contribution of molecular dipole (Section 5.8) and estimate the number of molecules detected in our measurement in Section 5.9. Finally, we demonstrate real-time analyte separation and detection on our graphene heterodyne sensors in Section 5.10.

5.2 Graphene FET fabrication

The fabrication of graphene field-effect-transistors (FETs) was carried out in Lurie Nanofabrication Lab at University of Michigan. The graphene FETs were fabricated on a silicon substrate with thermal oxide. A single layer graphene film was first grown on copper foils using the chemical vapor deposition method [5,6]. The growth parameters can be found in Appendix-B. After growth, 950 PMMA A2 (Microchem) was spin-coated on one side of the copper substrate and baked at 180 ^{0}C for 1 min. Graphene on the uncoated side was removed by 25 seconds of O_2 plasma etch and then the sample was placed in 0.1 M ammonium persulfate (Sigma-Aldrich) overnight to etch away the copper [7]. Next, the PMMA-coated graphene was transferred from solution onto a thermal oxide substrate and allowed to dry for a day. The silicon substrate acts as our back gate for electrical measurements. The PMMA was removed by placing the die in acetone and then IPA for 15 minutes each. Through photolithography, metal deposition, and bilayer lift-off processes using LOR 3A (Microchem) and SPR 220-3.0 (Shipley), 0.5 nm titanium/ 100nm gold source-drain electrodes were patterned. The graphene channel was patterned using photolithography and 25 seconds of O_2 plasma etch. In the final step, we cleaned the die by immersing it in warm acetone and then IPA for 30 min each. The entire fabrication is a 2 mask

process and described in Figure 5-1a. In the final step, the graphene sensor die was capped with a silicon flow channel 400 µm deep by 400 µm wide, fabricated by a deep reactive ion etch (DRIE) of a patterned silicon wafer for 30 minutes. The flow channel was carefully aligned to the centre of the die to ensure all the graphene sensors were exposed to the vapor flow. To secure the flow channel, a small amount of epoxy glue (Norland optical adhesive 81) was used at the edges. Connection of the graphene sensor module to a GC system was achieved by using a 70 cm long guard column (Restek, inner diameter 250 µm). Figure 5-1b shows an image of a graphene FET die, capped with a flow channel and GC column inserted at one end for analyte delivery.

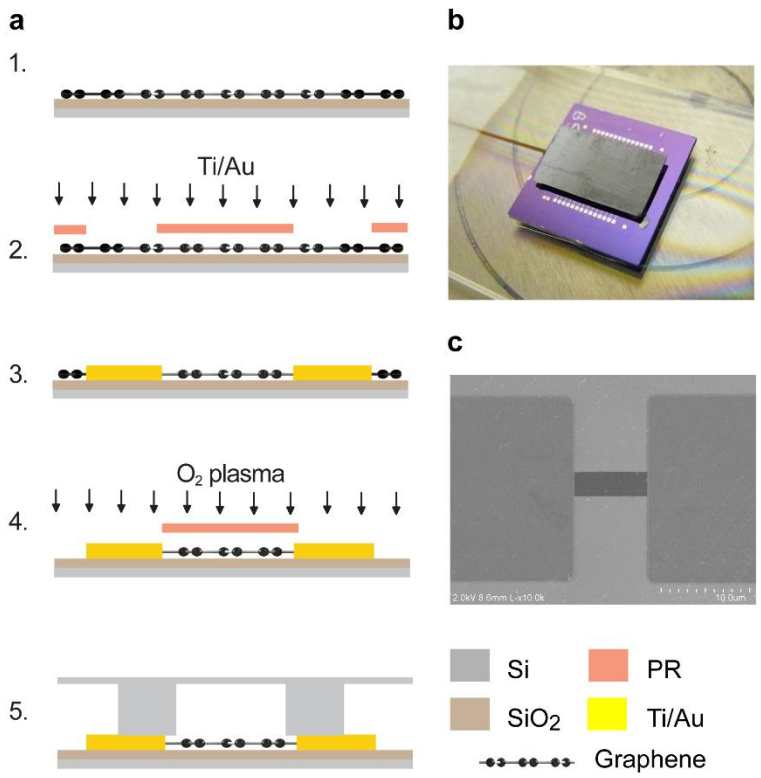

Figure 5-1. **(a)** Graphene transistor fabrication process flow - (1) graphene transferred from solution onto a SiO_2/Si substrate, (2) photomask layer-1 (PL-1) for source-drain metal deposition, (3) metal liftoff, (4) PL-2 for defining graphene channel using O_2 plasma etch, (5) placing a silicon flow channel on top of device. **(b)** Optical image of a finished device with a silicon flow channel on top and guard column at one end. **(c)** SEM image of a typical graphene FET. L = 7 µm and W = 2 µm.

Figure 5-1c is a scanning electron microscope of a pristine graphene ribbon (7μm x 2μm) between source-drain electrodes. Devices used in our study have graphene channel width of 1-4 μm, and length of 1-9 μm.

5.3 Gas chromatography vapor delivery system

A schematic of the gas chromatography (GC) vapor delivery system [8] is shown in Figure 5-2. The analytes can be sampled using a variety of methods like gas syringe, liquid syringe or a solid phase microextraction (SPME). In this thesis, we used liquid injection of analytes through the injector port. The analytes were vaporized in the injector oven which in our measurements was maintained at 250° C. We also used a GC split of 1:10000 to inject extremely small quantities of analytes, the rest being discarded. The analytes are carried into a capillary column using an inert carrier gas - helium. The capillary columns can either be uncoated or coated with a polymer. We use the uncoated column in our preliminary measurements where we characterize the graphene FET detector's response to different analytes. For studying the sensor response to a mixture of analytes delivered simultaneously, we use a combination of polymer coated columns to separate analytes spatially.

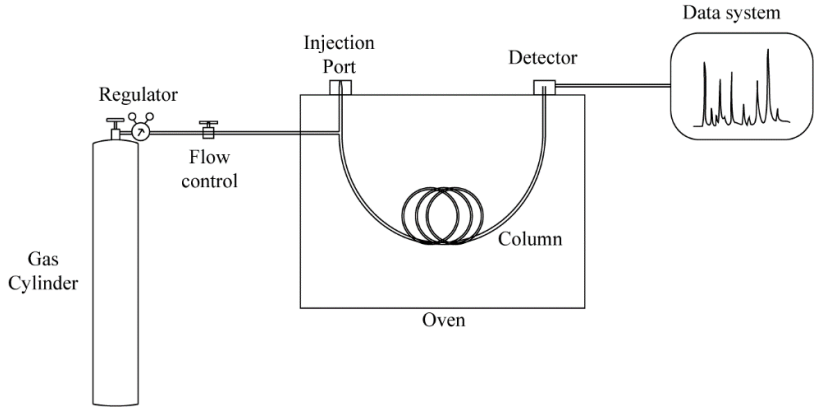

Figure 5-2. Schematic of gas chromatography vapor delivery system adapted from McNair and Miller, *Basic Gas Chromatography* [8].

Generally, in a gas chromatograph system the other end of the column is connected to either a flame-ionization-detector (FID) or a mass spectrometer (MS) which respond to the presence of each analyte [8,9]. Our setup consists of the GC separation column connected to the FID as well as our graphene FET sensor through a Y-split. The Y-split is used only during the detection of a mixture of analytes separated by the column and the length travelled by the analytes to the respective detector is kept same. This allows us to compare the response times of our graphene sensors with the industry standard FID in the same temporal window. During characterization of our sensors for the presence of different analytes, we directly connected the column to the graphene sensor without a Y-split, to accurately estimate the injected amount as the Y-split may not provide an exact 50-50 split. The experimental setup for our measurement is presented in Figure 5-3.

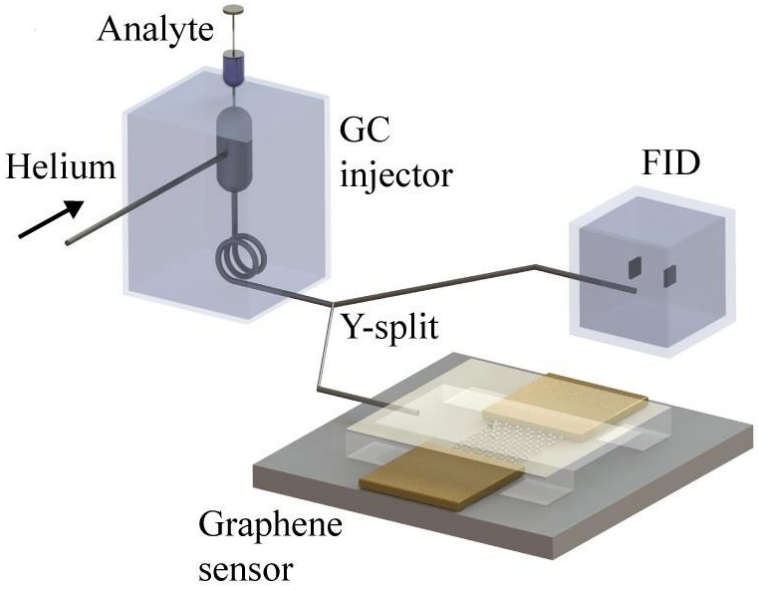

Figure 5-3. Experimental setup showing a gas chromatography (GC) injector connected to the graphene sensor and flame ionization detector (FID, standard vapor detector with <0.1 s time resolution and <1 ppb sensitivity) through a GC separation column and a Y-split.

5.4 Direct current (DC) electrical measurement setup

We pre-screened graphene FET devices based on their DC $I - V_g$ characteristics in air and chose ones with high *transconductance* ($g_m = \frac{dG}{dV_g}$) values for vapor measurements. The DC electrical measurement setup is presented in Figure 5-4a.

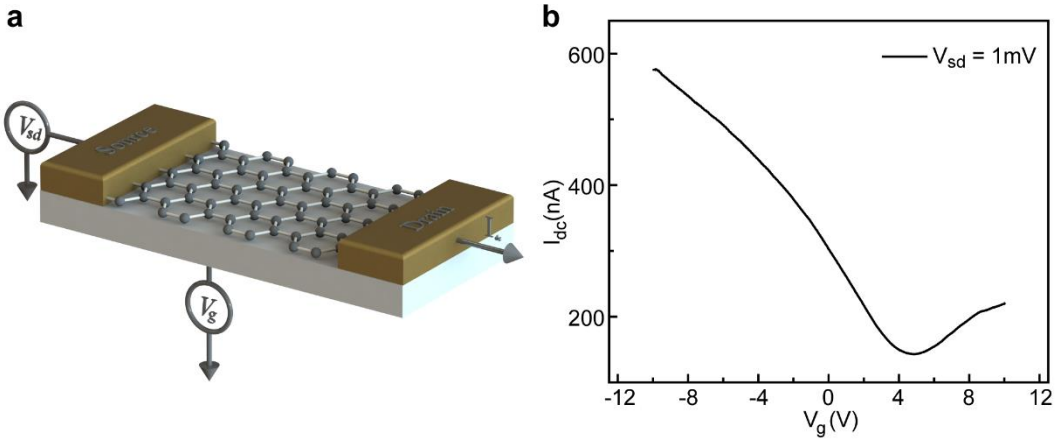

Figure 5-4. **(a)** DC electrical measurement schematic, **(b)** $I_{dc} - V_g$ curve for a graphene FET with channel length, L = 1 μm and width, W = 2 μm. Fit to Equation 5-3 yields a hole mobility value, μ = 600 $cm^2V^{-1}s^{-1}$.

The electronic instruments are controlled by a LabVIEW program, measureit-2.2 [10]. The source and gate voltages were applied through a DAQ card connected to a BNC connector box (National Instruments). The back-gate (silicon) voltage is swept and the output DC current is read at the drain terminal through the DAQ input ports via a DC pre-amplifier (DL-1211, Ithaca). Typical DC characteristic curve for a back-gated graphene field-effect-transistor in air is shown in Figure 5-4b.

We estimate the mobility of the graphene FETs from the DC characteristic curves. As discussed in chapter 1, the total charge density in graphene consists of both the residual charge density, n_0 [11] and electrostatic gate induced charge density, n:

$$n_{total} = \sqrt{n^2 + n_0^2}\,. \qquad \text{Equation 1-10}$$

Now, the conductivity for graphene can be considered as $\sigma = \mu n e$, where μ is mobility of carriers and e is electronic charge. This gives us the 2D resistance as:

$$R = \rho \frac{L}{W} = \frac{1}{\sigma}\frac{L}{W} = \frac{L}{\mu n e W}\,. \qquad \text{Equation 5-1}$$

The total resistance measured in 2-probe DC measurements (Figure 5-4) also includes the contact resistance R_c, hence the resistance measured is:

$$R = R_c + \frac{L}{\mu e W\sqrt{n^2+n_0^2}}\,. \qquad \text{Equation 5-2}$$

Here, $n = \frac{C_{bg}(V_g - V_{Dirac})}{e}$ and Equation 5-2 becomes:

$$R = R_c + \frac{L}{\mu e W\sqrt{\left(\frac{C_{bg}(V_g - V_{Dirac})}{e}\right)^2 + n_0^2}}\,. \qquad \text{Equation 5-3}$$

Now, the DC $I_{dc} - V_g$ curves can be fit with the above equation to obtain values for contact resistance (R_c), mobility (μ) and residual charge density (n_0). The hole mobility obtained for the device in Figure 5-4b is 600 $cm^2V^{-1}s^{-1}$.

5.5 Conventional direct current (DC) detection of chemical vapors

Mostly all nanoelectronic sensors rely on the detection of charges (refer to Section 2.3 and Section 3.2). Charge transfer between a surface adsorbed molecule and the nanomaterial changes the surface charge density, thus altering the Fermi energy and conductance of the sensor. The biggest challenge for such DC nanoelectronic vapor sensors is their extremely slow sensing response and recovery (10-1000s of seconds) [12-15]. Unfortunately, the slow response for nanoelectronic vapor sensors arises intrinsically from slow dynamics of interface trapped charges and slow defect-mediated

charge transfer processes [16-18], and therefore, is difficult, if not impossible, to overcome within the current framework of available sensing mechanisms.

Charge traps are present at the sensor/dielectric (oxide) interface and can extend up to ~5nm into the oxide [19]. Some researchers have also show that charge trapping effect is enhanced by the presence of water molecules near the oxide/ambient interface [17,20], leading to hysteresis. The relaxation times associated with oxide trap can be as high as 10 seconds [19,21] which makes DC sensing intrinsically slow. Moreover, charge transfer from vapor molecules into the active region of the sensor is efficient only at defect sites. Infact, the availability of defect binding sites is what leads to ppb level sensitivities for such DC sensors [16]. However, on the other hand it also leads to slow response times and sensor irreversibility as binding energy at these sites is high. Hence, in such cases sensor regeneration requires periodic external stimuli such as heating, exposure to ultra violet radiation, degassing etc., all of which are impractical for real-time on-site rapid vapor monitoring systems. Infact, in the absence of defect sites, these sensors show extremely poor response [22]. Recently, various chemoselective surface coatings have been used to reduce the response and recovery time to only a few seconds [23-25]. However, those coatings function only for a narrow set of vapor molecules and may possibly result in even slower response to other vapor molecules. All these drawbacks significantly hinder the employment of nanoelectronic sensors in applications like gas chromatography (GC), which require detection capability for a broad range of vapor analytes with sub-second response time and ppb-level sensitivity.

To demonstrate the limitations of DC response of graphene sensors, we setup the electrical measurement system as described in Figure 5-4a, and injected four different analytes - dimethylmethylphosphonate (DMMP), dimethylformamide (DMF), chloroform and 2-propanol. In Figure 5-5, we show the temporal response of a pristine graphene FETs to different amounts of above analytes. We observed-(1) the DC sensitivity is poor as there is no response at lower injection quantities, and (2) sensor recovery is slow for higher mass injections of analytes especially DMMP and DMF, where ($t_{recovery}$ ~ 100s).

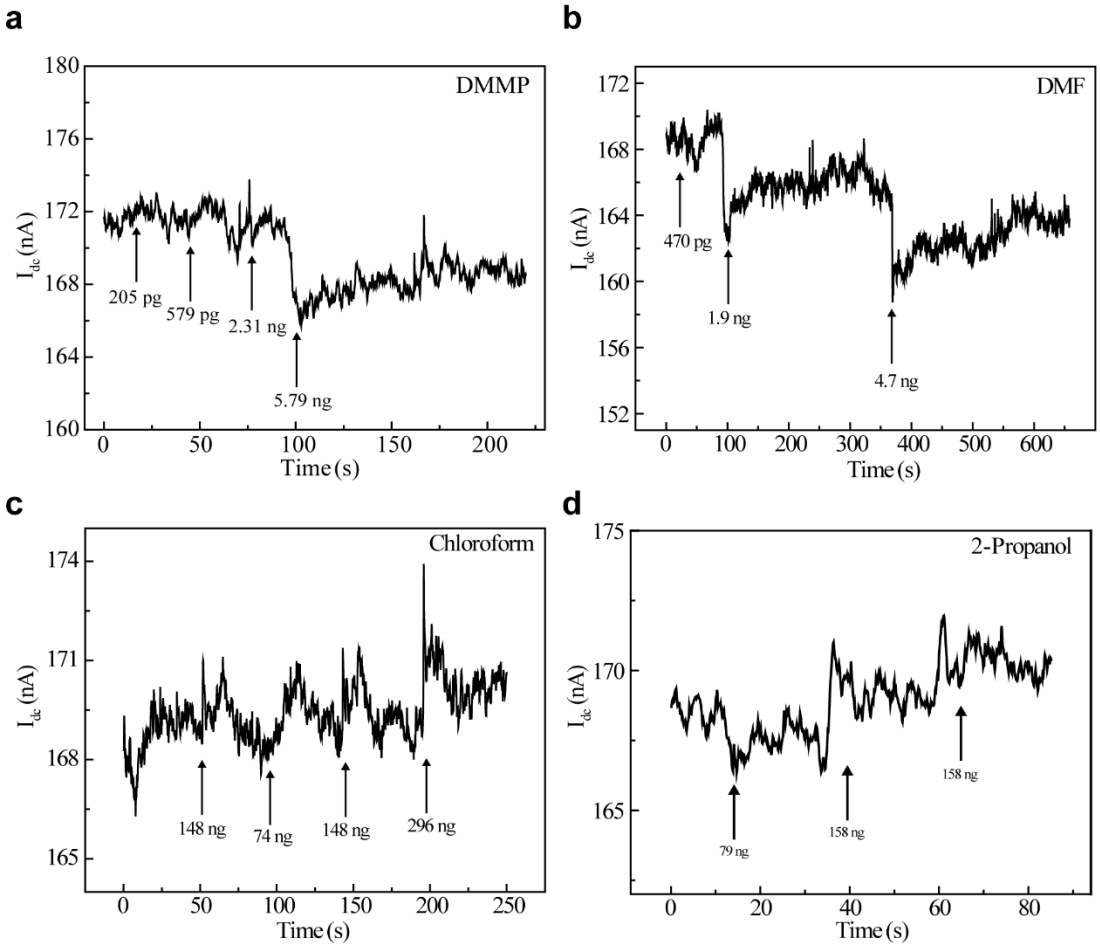

Figure 5-5. Temporal DC response of a GrFET sensor to **(a)** DMMP, **(b)** DMF, **(c)** chloroform and **(d)** 2-propanol. The source and gate voltages are V_{sd} = 1 mV and V_g = 0 V respectively.

In order to integrate nanoelectronic sensors with micro-GC components for rapid vapor analysis, we need to overcome these limitations of speed-sensitivity tradeoff. Next, we explore the graphene FET as a heterodyne vapor detector to demonstrate simultaneous high speed and high sensitivity detection.

5.6 Heterodyne mixing measurement for chemical vapor detection

For frequency-mixing measurements, used the 'one-source' setup (chapter 3). We applied an amplitude modulated (AM) voltage drive ($|\tilde{V}^{\omega}|$ = 20mV, f_c = 100 kHz, $|\tilde{V}^{\omega_m}|$ = 1V, f_m = 1.4342 kHz) to the source terminal. The dc bias at source and gate were held at ground (V_{sd}, V_g = 0 V), and the mixing current was detected at modulated frequency using a lock-in amplifier. The measurement schematic is illustrated in Figure 5-6a. When vapor molecules adsorb on graphene surface, the source AC drive excites the molecular dipoles in the adsorbed layer. These oscillating dipoles act as a modulating gate potential at the same frequency as drive voltage, leading to a mixing current term, which we monitor. Figure 5-6b represents the mixing-current response of the same graphene-FET sensor as in Figure 5-5, to 9 different analytes.

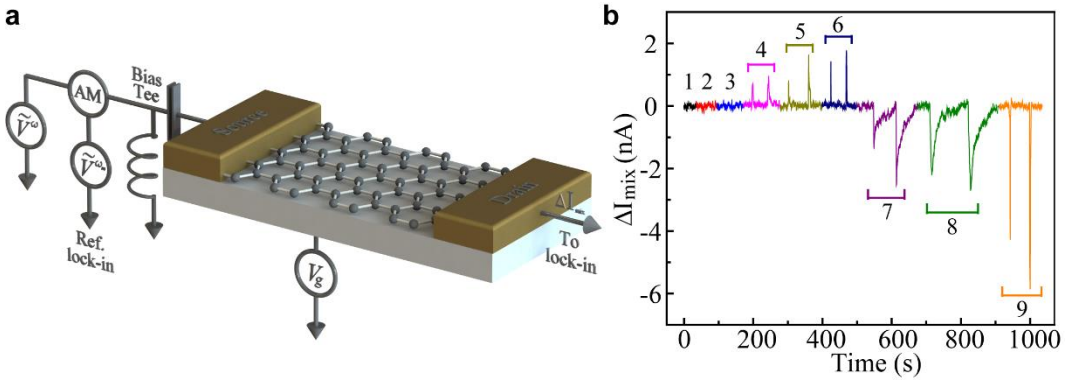

Figure 5-6. **(a)** Heterodyne detection electrical measurement setup. **(b)** Mixing current response of a graphene-FET sensor to injections of (1) pentane, (2) hexane, (3) benzene, (4) chlorobenzene, (5) dichloromethane, (6) chloroform, (7) N, N-dimethylformamide (DMF), (8) dimethylmethylphosphonate (DMMP), and (9) acetone.

We observed rapid detection of 6 out of 9 analytes Figure 5-6b. Furthermore, these results indicate that our graphene sensor was highly selective to polar molecules: three non-polar molecules (pentane, hexane, and benzene) showed no signal, while the remaining polar ones showed strong response. In addition, the sensing signal also has different signs for different molecules. We will discuss the detection mechanism later in Section 5.7. Importantly, by using higher frequencies, the slow sensing response hindering the conventional nanoelectronic sensor was overcome when the AC field switching outpaced the slow dynamics of interface states. And, by detecting the molecular dipoles of the adsorbed species, we avoided the slow charge-transfer processes as well. Next, we looked at the figure-of-merit of our graphene heterodyne sensors in terms of speed and sensitivity of response.

5.6.1 Speed

The most important criteria for rapid insitu detection of volatile organic compounds are the response and recovery times. In our measurements, we take the full width half maximum (FWHM, $t_{1/2}$) of the response curves as the figure-of-merit for the speed of the sensor. For reference, we compared the graphene sensor response with the flame-ionization-detector (FID) response, which is an industry gold standard for GC detectors. The temporal response of the graphene FET sensor to pulsed injections of varying masses of common volatile organic compounds is presented in Figure 5-7 and Figure 5-8. In order to minimize the peak broadening caused by the GC column, a GC guard column (Restek Corporation), which has a minimal broadening effect, was used to deliver analytes to the graphene sensor and FID, separately. The length of the

delivery column to graphene sensor was 70 cm. All parameters were kept the same for analysis with FID.

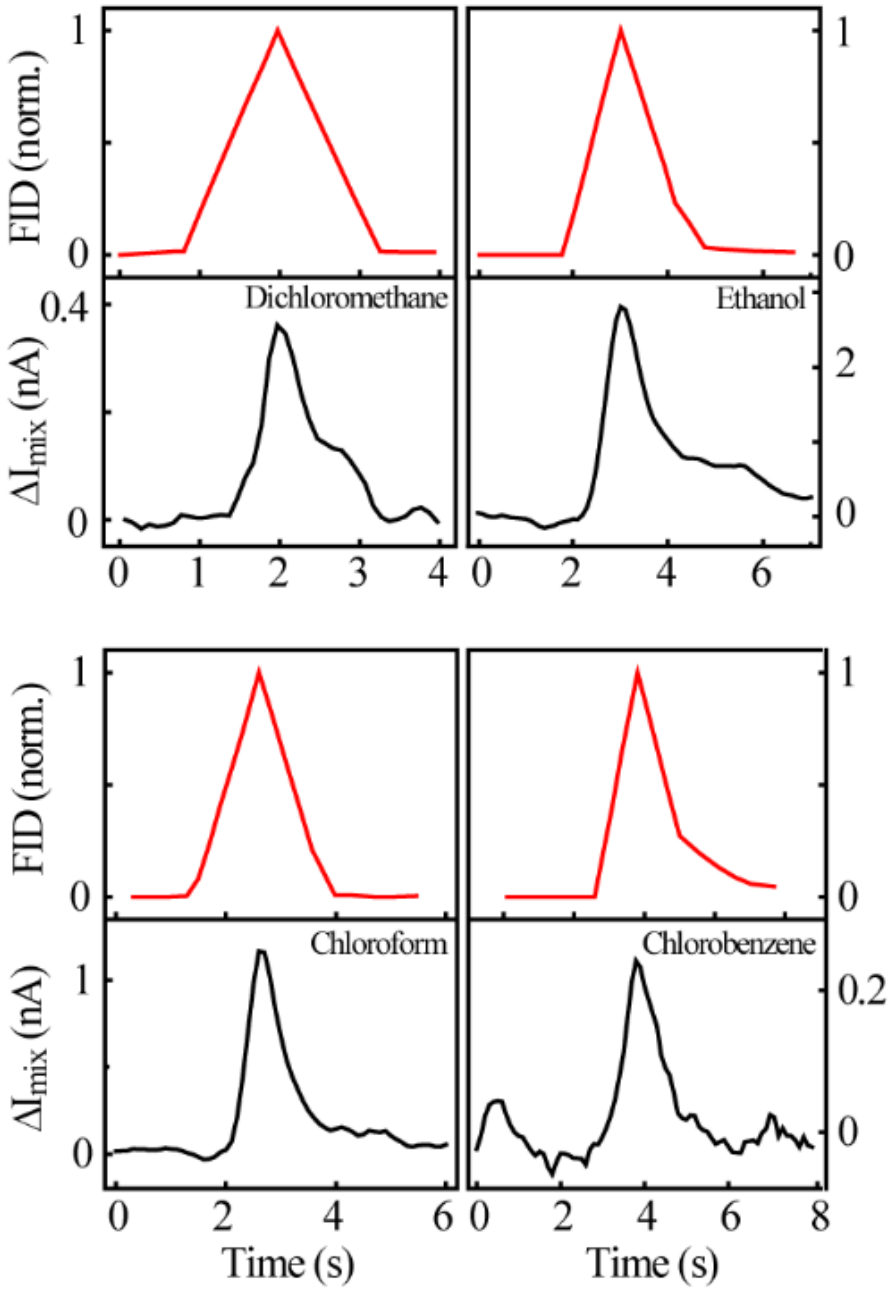

Figure 5-7. Graphene sensor response to different chemical vapors. Comparison of the temporal response of the FID (red, top panels) and graphene sensor (L = 7 µm, W = 2 µm) measured at V_{sd} = 0 V, V_g = 0 V, f_c = 100 kHz, $\left|\tilde{V}^{\omega}\right|$ = 20 mV, f_m = 1.4342 kHz, m = 1 (black, bottom panels) to the same injected mass of 4 analytes (dichloromethane – 66.5 ng, ethanol – 78.8 ng, chloroform – 296 ng, chlorobenzene – 5.5 ng).

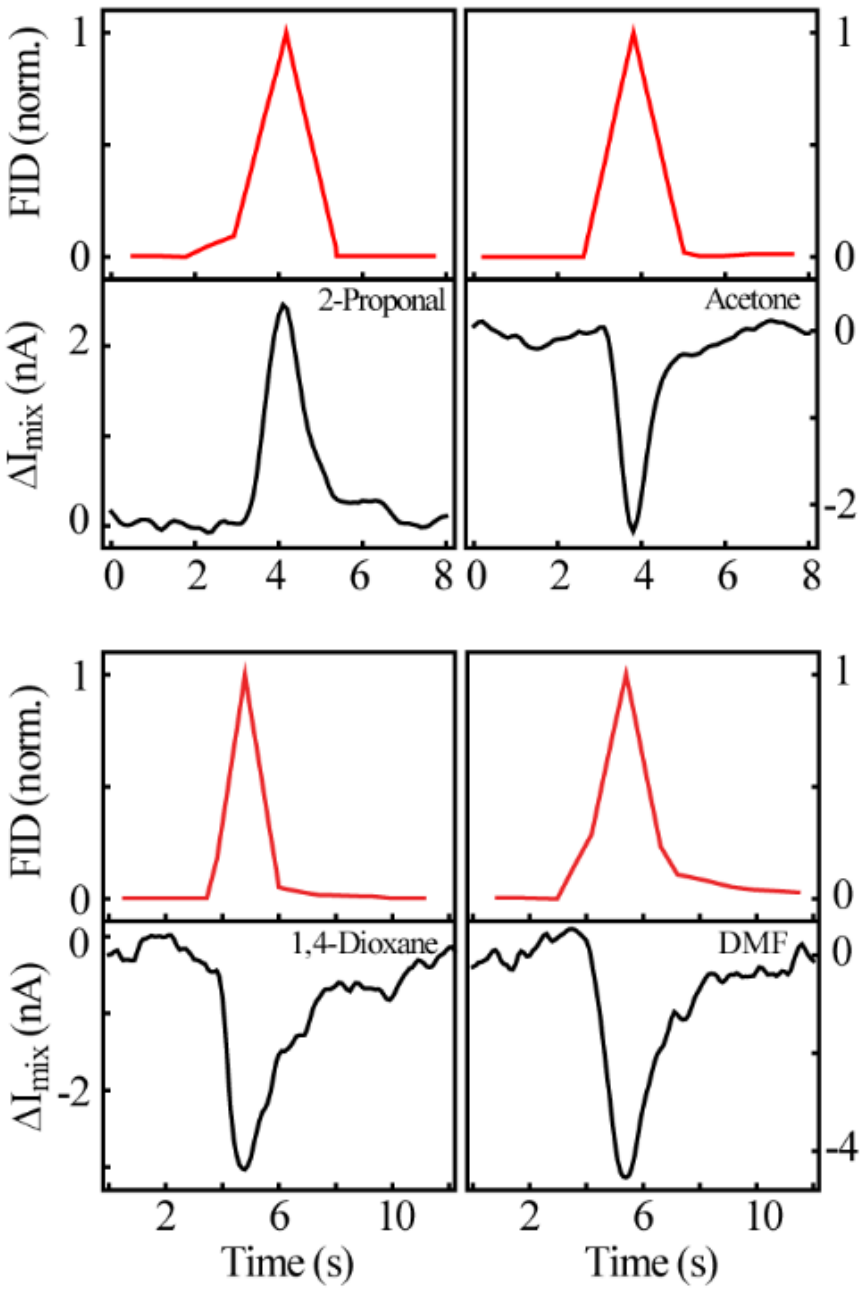

Figure 5-8. Graphene sensor response to different chemical vapors. Comparison of the temporal response of the FID (red, top panels) and graphene sensor measured at V_{sd} = 0 V, V_g = 0 V, f_c = 100 kHz, $\left|\tilde{V}^{\omega}\right|$ = 20 mV, f_m = 1.4342 kHz, m = 1 (black, bottom panels) to the same injected mass of 4 analytes (2-propanol – 78.5 ng, acetone – 15 ng, 1,4-dioxane – 51.5 ng, and DMF – 4.72 ng). 2-propanol and acetone were measured on a device with L = 7 µm and W = 2 µm. 1, 4-dioxane and DMF were measured on a device with L = 9 µm, W = 2 µm at $\left|\tilde{V}^{\omega}\right|$ = 30 mV, all other parameters being the same.

Fast sensor response with a sub-second full-width-half-maximum (FWHM, $t_{1/2}$) times was observed for dichloromethane ($t_{1/2}$ = 0.61 s), ethanol ($t_{1/2}$= 0.92 s), chloroform ($t_{1/2}$ = 0.69 s), 2-propanol ($t_{1/2}$ = 0.98 s) and acetone ($t_{1/2}$= 0.75 s), which were similar to or faster than FID response times (Figure 5-7). Even for relatively high boiling point vapors - chlorobenzene, 1, 4-dioxane, and DMF, whose boiling point is over 100° C, the graphene heterodyne sensor still showed impressive responses time of 0.9 s, 1.65 s and 1.8 s respectively (Figure 5-8), which was again comparable to the FID response. Although 1, 4-dioxane and DMF showed slow desorption from the graphene surface, total response time (90% recovery time, $t_{90\%}$) still compares well with the FID responses.

5.6.2 Sensitivity

Vapors of a higher boiling point tend to condense more on a surface and thus have longer desorption time, hence can be used as a model system to determine the ultimate sensitivity of nanoelectronic sensors. We used dimethylmethylphosphonate (DMMP, boiling point 181° C), a nerve agent simulant, which is an important analyte for micro gas chromatography measurements, for testing the sensitivity of our graphene heterodyne vapor sensors. Figure 5-9a presents the temporal response of the graphene FET sensor to 205 pg injection of DMMP along with the corresponding FID response time (in red). We observed comparable response time for graphene sensor ($t_{1/2}$ = 6.1 s) and FID ($t_{1/2}$= 5.5 s). However, DMMP desorption time for graphene sensor ($t_{90\%}$ = 28 s) was approximately two times that of FID ($t_{90\%}$ = 13.2 s), indicative of the slow desorption process of DMMP molecules from the graphene surface. Since the minimum quantity that can be injected through a liquid syringe is 579 pg for DMMP,

we used a 1:1 mixture of acetone: DMMP to inject lower quantities of DMMP. The exact amount of DMMP in the mixture is calibrated using the FID (Appendix-C).

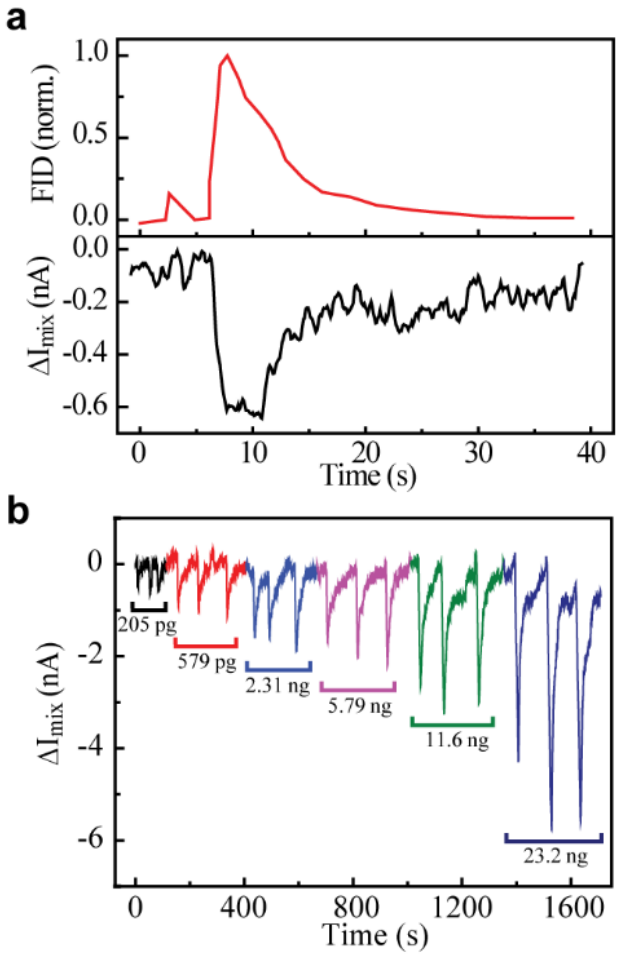

Figure 5-9. **(a)** Temporal response of the FID (red) and graphene sensor (black) to 205 pg injected mass of DMMP. **(b)** Chromatographic response of the sensor to repeated pulses of DMMP at varying mass injections noted in the figure. Error bars show the standard deviation over 3 runs. Analytes were delivered using a 70 cm long guard column at a carrier gas (helium) flow rate of 8 mL/min. All measurements were carried out in air, at atmospheric pressure and room temperature.

To determine the sensor performance towards DMMP, we plot the sensor response ΔI_{mix}, to repeated doses of DMMP varying from 205 pg to 23.2 ng in Figure 5-9b. We observed that sensing signal increased with increasing injected mass of

DMMP, and that the response was instantaneous and also completely reversible for all the masses under test. Experimentally, the lowest injected mass was 205 pg, corresponding to a concentration of approximately 43 ppb (see Appendix-D for concentration calculation). To further estimate the sensor detection limit, we plot sensor dosage response in the log-log scale in Figure 5-10. Linear fit to this plot gave a slope of 0.4. Using a 3σ noise floor calculated from graphene response in the absence of analytes (3σ = 0.12 nA, see Appendix-E), the detection limit of our graphene sensor for DMMP is approximately 3 pg in mass or 0.64 ppb in concentration, which to our knowledge is the lowest for any uncoated, pristine nanoelectronic vapor sensor.

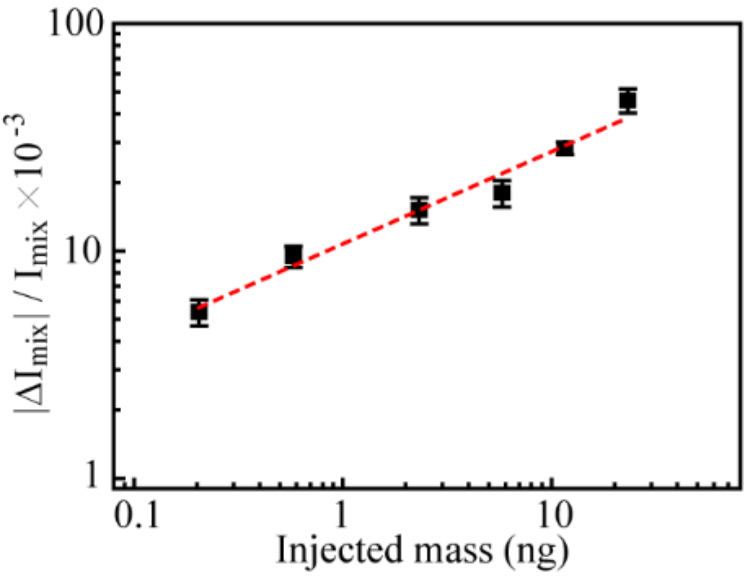

Figure 5-10. Measured relative mixing current change of graphene sensor to DMMP mass injections from Figure 5-9b. Linear fit (red) to log-log plot gives a slope of 0.4.

To demonstrate the capability of heterodyne sensors to detect a wide range of vapor analytes, we present the graphene sensor dosage response to 9 additional analytes on the log-log scale Figure 5-11. All analytes are linear on the log-log scale at low concentrations and saturate at higher concentrations. The parameters and the

experimental results (dipole moment, boiling point, lowest injected mass, response time and concentration at lowest injected mass) of all 13 analytes studied are summarized in Table 1.

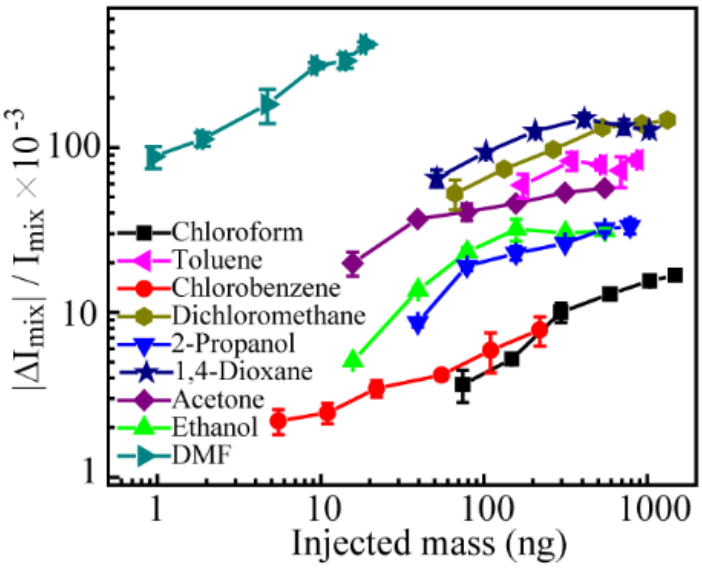

Figure 5-11. Measured relative mixing current response at varying mass injections of 9 different analytes. Error bars show the standard deviation over 3 runs. Analytes were delivered using a 70 cm long guard column at a carrier gas (helium) flow rate of 8 mL/min. All measurements were carried out in air, at atmospheric pressure and room temperature.

The superior performance of the high-frequency heterodyne detection compared to DC conductance measurement is obvious when we contrast the results in Figure 5-5a with Figure 5-9b. The measurements have been carried out on the same device. Clearly, we can observe that heterodyne mixing measurement (i) is more than an order-of-magnitude sensitive than DC response, (ii) is completely reversible unlike the DC conductance measurements, (iii) has much faster response and recovery times than DC response and (iv) has lower noise levels.

Analyte	Dipole moment (D)	Boiling point (°C)	Smallest injected mass (ng)	FWHM ($t_{1/2}$, s)	Concentration at minimum injected mass (ppm)
Pentane	0	36	-	-	-
Hexane	0	69	-	-	-
Benzene	0	80	-	-	-
Toluene	0.37	111	172	1.61	210
1,4-Dioxane	0.45	101	52	2.1	50
Chloroform	1.04	61	74	0.68	164
Chlorobenzene	1.54	131	5.5	0.75	12
Dichloromethane	1.6	40	66	1	139
2-Propanol	1.66	82	39	1.12	105
Ethanol	1.69	79	15	0.9	65
Acetone	2.88	56	15	0.8	58
DMMP	3.62	181	0.205	6.83	0.043
DMF	3.82	153	0.944	2.54	0.92

Table 1. Experimentally detected minimum concentration of analytes. Listed are the smallest injected mass detected by the sensor, full width half maximum ($t_{1/2}$; mean of 3 runs), and minimum concentration calculated using injected mass and $t_{1/2}$.

5.7 Mechanism for heterodyne vapor detection

It is clear from Figure 5-6 that polar molecules yield a stronger signal whereas the signal from non-polar molecules is nearly negligible. This distinct sensor response is attributed to the fact that heterodyne detection is based on the molecular dipole induced charge density modulation on graphene, and is proportional to the molecules dipole moment. To further confirm the dipole detection based sensing mechanism, we measured the sensor response to a pair of *cis*- and *trans*- isomers, *cis*- and *trans*- 1, 2-

dichloroethene, with the same injected mass (Figure 5-12). It is clear that the polar *cis*-1, 2-dichloroethene (dipole moment = 1.9 D) exhibits a strong sensing signal, while the non-polar *trans*-1, 2-dichloroethene (dipole moment = 0 D) only shows minimal response below the 3σ noise floor.

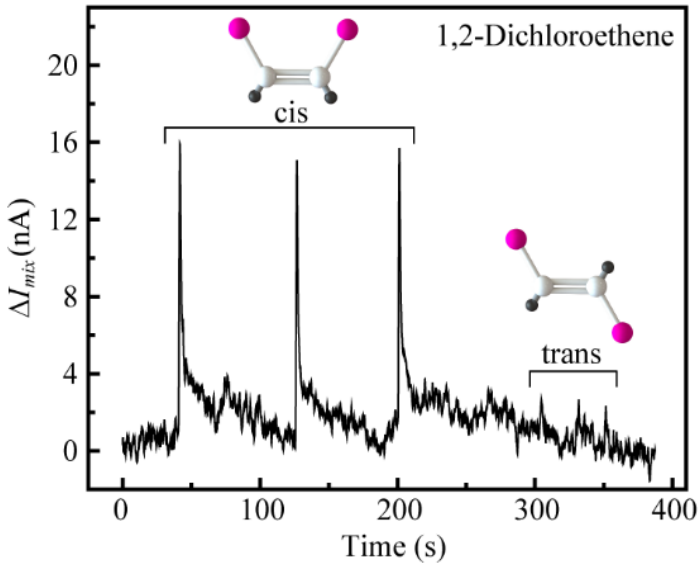

Figure 5-12. Measured mixing current response for a pair of *cis*- and *trans*- isomers, 1, 2-dichloroethene, with the same injected mass of 1.28 µg. Only the polar *cis*-1, 2-dichloroethene shows strong sensor response. The analytes were measured on a device with L = 1 µm, W = 1 µm, at $\left|\tilde{V}^{\omega}\right|$ = 12 mV.

The graphene heterodyne sensor further exhibits strong bi-polar behaviour, as exemplified in Figure 5-13, where the sensor response can be categorized into 3 types – zero (Left Panel), positive (Middle Panel), and negative (Right Panel). This characteristic can again be traced to the fact that our sensor is responsive to the dipole moment of the surface adsorbed molecule. Consequently, non-polar molecules, such as hexane and benzene, show no sensing signal. On the other hand, for polar molecules adsorbed on top of graphene, opposite dipole orientation can lead to opposite signs in the mixing current signal. This bi-polar response of the graphene heterodyne sensor not

only adds an additional degree of selectivity for vapor identification, but also hints at its potential as an excellent test-bed for elucidating the fundamental molecule-graphene interaction.

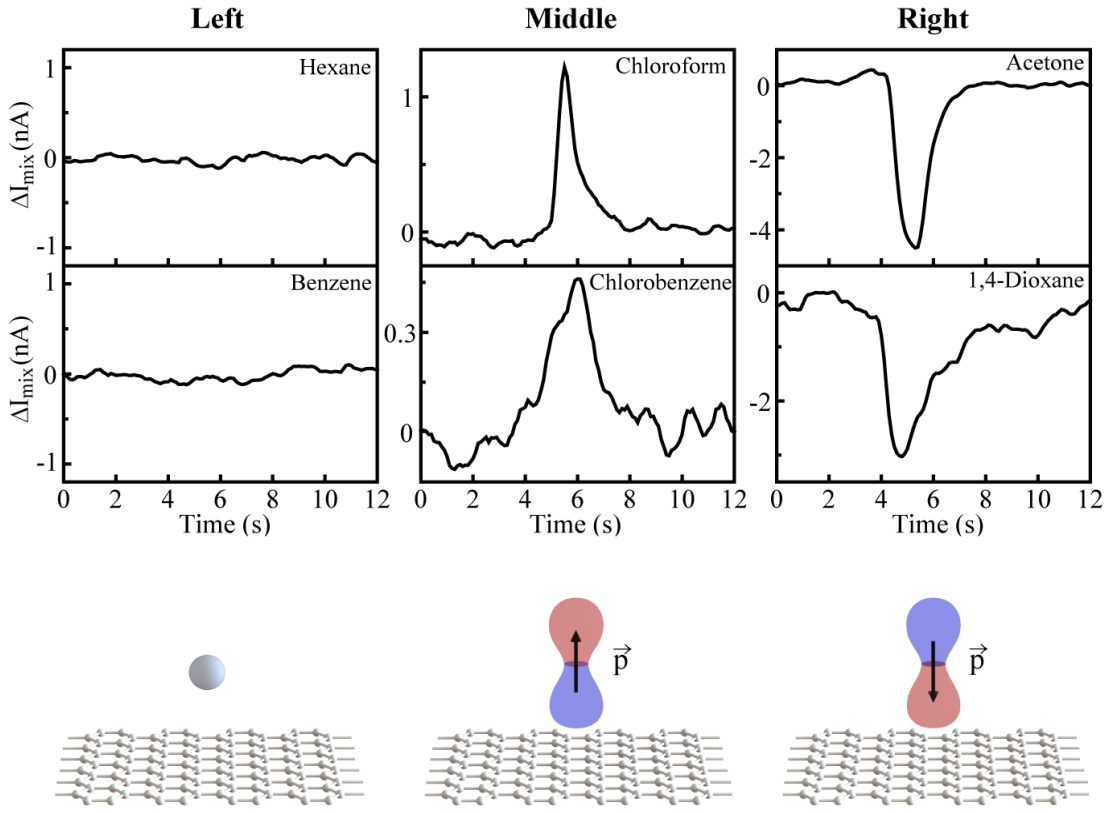

Figure 5-13. Graphene sensor chromatographic response and the corresponding illustration of the orientation of vapor molecules. **Left Panel** – (Top) Measured mixing current response for hexane and benzene with an injected mass of 131 ng and 43.8 ng, respectively. (Bottom) Schematic illustration of an analyte with zero dipole moment on graphene. **Middle Panel** – (Top) Measured mixing current response for chloroform and chlorobenzene with an injected mass of 296 ng and 55 ng, respectively. (Bottom) Schematic illustration of an analyte on graphene with the electronegative cloud (blue) closer to the graphene surface. **Right Panel** – (Top) Measured mixing current response for acetone and 1, 4-dioxane with an injected mass of 156 ng and 51.5 ng, respectively. (Bottom) Schematic illustration of an analyte on graphene with the electropositive cloud (red) closer to the graphene surface. $\vec{\boldsymbol{p}}$ is the molecular dipole moment vector. The analytes were measured on a device with L = 7 µm, W = 2 µm, at $\left|\tilde{V}^{\omega}\right|$ = 20 mV.

5.8 Heterodyne mixing contribution from adsorbed vapor molecules

In this section, we derive a general expression for contribution of adsorbed vapor molecule to mixing current response of a graphene FET. Continuing the discussion from chapter 3, the DC current-voltage relation for a transistor is given as

$$I = \frac{\mu W}{L}\left[C_g\left(V_g - \frac{1}{2}V\right) + Q_m\right] \cdot V, \qquad \text{Equation 5-4}$$

where Q_m is the adsorbed molecule induced charge per unit area inside the graphene channel. Importantly, since vapor molecules are charge neutral, Q_m is zero unless there is charge transfer between molecule and graphene or under imperfect screening. This is the fundamental reason why pristine graphene DC sensors have low sensitivity toward most vapor molecules.

A time varying AC excitation at ω, $\tilde{V}^{\omega}$ will modulate the channel potential and generate charge density modulation due to electrostatic coupling with gate. In addition, $\tilde{V}^{\omega}$can also excite the adsorbed molecules, which in turn produce a dipole-induced charge density modulation at ω, $\tilde{Q}_m^{\omega}$. Thus, the heterodyne mixing current from Equation 3-3 can be expressed as:

$$I_{mix} = \frac{\mu W}{L}\left[C_g\left(-\frac{1}{2}\tilde{V}^{\omega}\right) + \tilde{Q}_m^{\omega}\right] \cdot \tilde{V}^{\omega}. \qquad \text{Equation 5-5}$$

The second term is related to the molecular dipole-induced charge perturbation in graphene. Hence, we can measure the changes in mixing current due to molecular adsorption as the sensor signal

$$\Delta I_{mix} = \frac{\mu W}{L}\tilde{Q}_m^{\omega} \cdot \tilde{V}^{\omega}. \qquad \text{Equation 5-6}$$

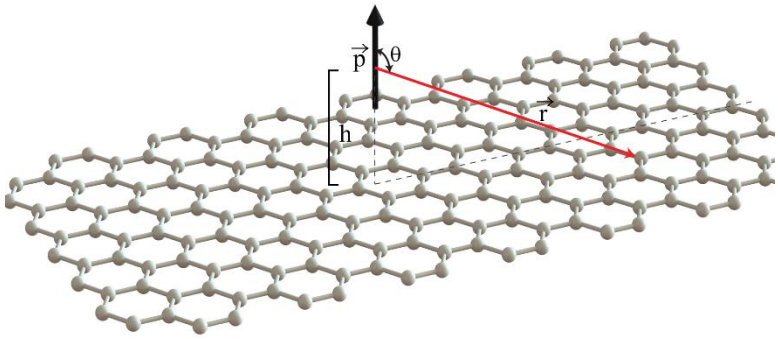

Figure 5-14. Model of surface adsorbed molecule located above graphene film with dipole moment, $\vec{p}$ perpendicular to the graphene surface.

To calculate, $\tilde{Q}_m^{\omega}$ we first examine a single molecule with a dipole moment, $\vec{p}$ adsorbed on the centre of graphene surface. For simplicity, we assume the molecule-graphene vertical distance is h, and the dipole moment is perpendicular to the graphene surface (Figure 5-14). The electric field on graphene due to the molecular dipole can be expressed as

$$\vec{\boldsymbol{E}}_{Gr} = \frac{1}{4\pi\varepsilon_0}\left[\frac{3(\vec{\boldsymbol{p}}\cdot\hat{\boldsymbol{r}})\hat{\boldsymbol{r}}-\vec{\boldsymbol{p}}}{r^3}\right], \qquad \text{Equation 5-7}$$

where $\vec{r}$ is a point on graphene from $\vec{p}$. $\hat{r}$ is its unit vector, and the angle between $\vec{r}$ and $\vec{p}$ is θ. This local electric field polarizes graphene:

$$\vec{\boldsymbol{p}}_{Gr} = \alpha_{Gr}\vec{\boldsymbol{E}}_{Gr} = \frac{\alpha_{Gr}}{4\pi\varepsilon_0}\left[\frac{3(\vec{\boldsymbol{p}}\cdot\hat{\boldsymbol{r}})\hat{\boldsymbol{r}}-\vec{\boldsymbol{p}}}{r^3}\right], \qquad \text{Equation 5-8}$$

where α_{Gr} is graphene's polarizability and $\vec{\boldsymbol{p}}_{Gr}$ is the molecular dipole induced graphene dipole moment at $\vec{r}$. The macroscopic polarization normal to graphene surface, $\vec{\boldsymbol{P}}_{Gr}^{Z}$ can be obtained by integrating $\vec{\boldsymbol{p}}_{Gr}$ over the entire graphene lattice. The unit area can be calculated as $\mathrm{d}A = 2\pi r \sin\theta \frac{-h}{\cos^2\theta} d\theta$, while the number of carbon

atoms within this unit area is given by $\frac{2\,dA}{A_{uc}}$, with A_{uc} = 0.051 nm^2 being the unit cell area of graphene. Hence, we have:

$$\vec{\boldsymbol{P}}_{Gr}^{Z} = \frac{1}{W\times L\times t}\int_{\pi}^{\pi-\cos^{-1}\left(\frac{2h}{W}\right)} \frac{\alpha_{Gr}}{4\pi\varepsilon_0}\left[\frac{3(\vec{\boldsymbol{p}}\cdot\hat{\boldsymbol{r}})\hat{\boldsymbol{r}}-\vec{\boldsymbol{p}}}{r^3}\right]\frac{2}{A_{uc}}2\pi r\sin\theta\,\frac{-h}{\cos^2\theta}\,d\theta$$

$$= \frac{1}{W\times L\times t}\frac{\alpha_{Gr}}{4\pi\varepsilon_0}\frac{4\pi}{A_{uc}}\frac{p}{h}\int_{\pi}^{\pi-\cos^{-1}\left(\frac{2h}{W}\right)} -\sin\theta\,(3\cos^2\theta-1)\,d\theta$$

$$\approx \frac{1}{W\times L\times t}\frac{\alpha_{Gr}}{4\pi\varepsilon_0}\frac{4\pi}{A_{uc}}\frac{p}{h}\frac{2h}{W}$$

$$= \frac{1}{W^2\times L\times t}\frac{\alpha_{Gr}}{4\pi\varepsilon_0}\frac{8\pi}{A_{uc}}p\ , \qquad \text{Equation 5-9}$$

with t being the thickness of the graphene film. For simplicity, we only add up all atoms within the radius of $W/2$ (assuming $W < L$) in the integration.

An AC drive voltage at ω will cause the molecular dipole to oscillate at the same frequency, introducing charge density fluctuation on graphene. Here, we include a proportional quantity, $\gamma(\tilde{V}^{\omega},\omega)$ to account for the degree of dipole excitation, $\gamma(\tilde{V}^{\omega},\omega)p$. The amount of dipole perturbation at ω would depend on the strength of the AC drive voltage compared with the binding strength between molecule and graphene. See Appendix-F for mixing current dependence on AC drive voltage. If the molecule is in free space, then one would expect the entire molecule to flip following $\tilde{V}^{\omega}$, *i.e.* $\gamma = \cos\omega t$. Hence, the oscillating molecular dipole induced charge density fluctuation on graphene can be estimated by:

$$\tilde{Q}_m^{\omega} = \gamma\left(\tilde{V}^{\omega},\omega\right)\vec{\boldsymbol{P}}_{Gr}^{Z} = \gamma\left(\tilde{V}^{\omega},\omega\right)\frac{1}{W^2\times L\times t}\frac{\alpha_{Gr}}{4\pi\varepsilon_0}\frac{8\pi}{A_{uc}}p\ . \qquad \text{Equation 5-10}$$

We emphasize that since graphene is not an ideal metal, Equation 5-10 only serves for order of magnitude calculation. From Equation 5-6 and Equation 5-10, we obtain the sensing signal for a single molecule:

$$\Delta I_{mix} = \frac{\mu W}{L}\gamma\left(\tilde{V}^{\omega},\omega\right)\frac{1}{W^2\times L\times t}\frac{\alpha_{Gr}}{4\pi\varepsilon_0}\frac{8\pi}{A_{uc}}p\tilde{V}^{\omega} = \frac{\gamma(\tilde{V}^{\omega},\omega)\mu}{W\times L^2\times t}\frac{\alpha_{Gr}}{4\pi\varepsilon_0}\frac{8\pi}{A_{uc}}p\tilde{V}^{\omega}\ .$$

Equation 5-11

If $n = \frac{N}{WL}$ is the areal density of the surface adsorbed molecules, we have:

$$\Delta I_{mix} = \frac{\gamma(\tilde{V}^{\omega},\omega)\mu}{L\times t}\frac{\alpha_{Gr}}{4\pi\varepsilon_0}\frac{8\pi}{A_{uc}}np\tilde{V}^{\omega}$$ Equation 5-12

for a quantitative measurement of analyte concentration in the vicinity of graphene sensor. For better noise rejection, we use AM modulation in all our measurements. This does not change anything related to the above equations, except that we now measure the mixing current change at the modulation frequency rather than DC.

5.9 Estimation of number of vapor molecules detected

We estimate the sensor detection limit using Equation 5-11. For a typical device, we use $L = W$ = 1 μm, t = 0.34 nm, μ = 1000 $cm^2V^{-1}s^{-1}$, and α_{Gr} = 0.9 $Å^3$ (in CGS unit, Ref [26]). A single DMMP molecule with p = 3.62 Debye is adsorbed on graphene surface. For simplicity, we assume the molecular dipole is partially excited at $\left|\tilde{V}^{\omega}\right|$= 20 mV, with $\gamma = 0.1 \times \cos\omega t$. Using Equation 5-11, we estimate a sensor signal on the order of ~3 fA for a single DMMP molecule. Using a 3σ noise floor of 0.12 nA (Appendix-E), we estimate a detection limit of ~10^4 molecules for our heterodyne sensor.

We can also compare this number with estimation from concentration calculation. Using the molecule weight of 124 g/mol and the mass density of 1.145 g/mL (liquid), we estimate that the inter-molecule distance is approximately 0.57 nm for liquid DMMP. Therefore, the maximal number of DMMP molecules adsorbed and closely packed on a 1 μm (L) x 1 μm (W) graphene surface is approximately 3x10^6.

From Figure 5-9b we assume that 23.2 ng of injected DMMP molecules saturate the graphene surface and form a liquid layer, which generates a sensing signal of approximately 6 nA (see Figure 5-9b). Using a 3σ noise floor of 0.12 nA, we estimate that the *upper limit* of detectable DMMP molecules on the graphene sensor surface is approximately $6x10^4$, agreeing with the detection limit estimated from Equation 5-11.

5.10 Real time analyte separation and detection

Rapid separation and detection of chemical vapors is of critical importance for on-site vapor monitoring with portable μGC systems. In Figure 5-15, we present the response of graphene sensor (lower panel) and FID (upper panel) to a mixture of eight analytes. The analytes were separated using a combination of columns and delivered simultaneously to graphene sensor and FID using a Y-split (Figure 5-3). Analytes were separated and delivered using a combination of 7.2 m long CP-SIL-5-CB column, 2.8 m long Carbowax column, and 70 cm long guard column. Temperature and flow programming were used to achieve rapid separation, while maintaining sharp peaks. The oven temperature was initially set to 32° C, after 36 seconds it was ramped up to 45° C at a rate of 50° C/min. The temperature was held at 45° C for 24 seconds before being ramped up to 80° C at 100° C/min. After 12 seconds the temperature is increased to 110° C at 50° C/min and held there for the rest of the run. The flow pressure is initially set to 15 psi and ramped at a rate of 30 psi/min to 19 psi, after 30 seconds. A Y-split, placed after the CP-SIL-5-CB and Carbowax columns is used to split the analytes in a near 50-50 ratio and deliver them to the graphene sensor and FID simultaneously using two 70 cm long guard columns. Injector oven and FID oven were set at 250° C and 300° C respectively.

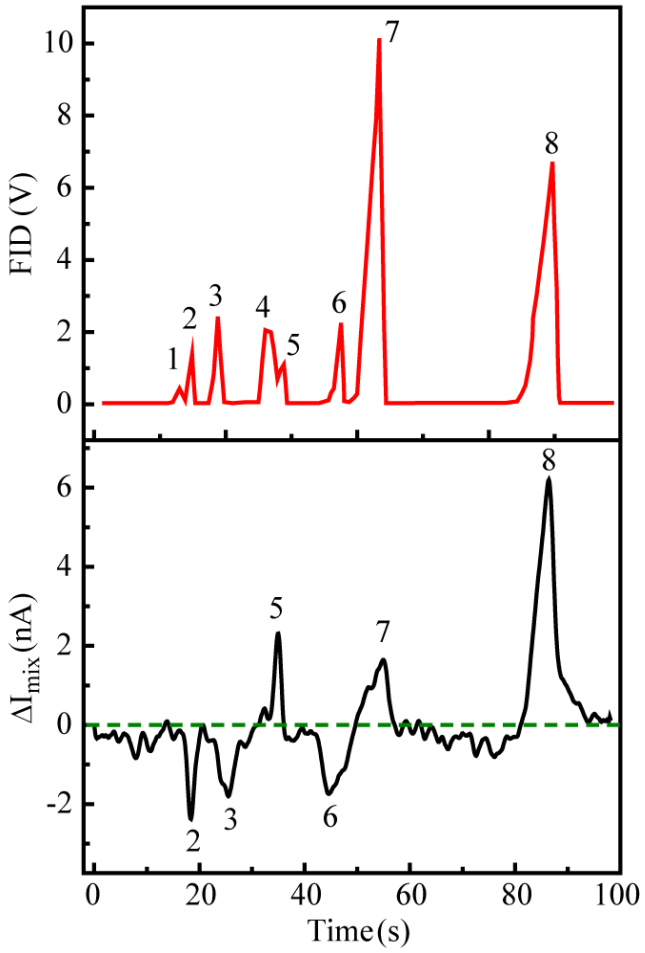

Figure 5-15. GC chromatograms obtained simultaneously from the FID (red, top panel) and the graphene sensor (black, bottom panel). The mixing current baseline for the sensor is marked by the green dashed line in lower panel. Graphene sensor device (dimensions - L = 2 µm and W = 2 µm) was operated at V_{sd} = 0 V, V_g = 0 V, f_c = 100 kHz, $\left|\tilde{V}^{\omega}\right|$ = 10 mV, f_m = 1.4342 kHz and m = 1. Peaks correspond to: (1) – pentane, (2) – acetone, (3) – 2-propanol, (4) – benzene, (5) – chloroform, (6) – 1,4-dioxane, (7) – toluene, and (8) – chlorobenzene.

We observed that the graphene sensor not only responds instantaneously to all polar molecules in the same temporal window as the FID, but also switches sign rapidly for electronegative and electropositive species (relative to graphene), delivered one after the other as shown in Figure 5-15. Pentane and benzene, being non-polar were not detected by the graphene sensor. We have observed both positive and negative ΔI_{mix}

response to 2-propanol in our measurements, however all devices processed (including thermal oxide growth) in one batch show consistent behavior. We feel this is a substrate effect [27] where end terminations may preferentially orient the alcohol molecules through hydrogen bonding, however further investigation is needed.

5.11 Conclusions and future work

In this chapter, we successfully demonstrated heterodyne graphene based vapor sensors, and for the first time demonstrated high speed (~0.1 s) and extremely high sensitivity (< 1ppb detection limit) detection of a range of analytes on a pristine graphene device without any surface functionalization. We also convincingly proved heterodyne sensing is a dipole detection based mechanism by testing *cis*- and *trans*-isomers which have same composition but different dipole moments. Compared to existing nanoelectronic vapor sensor technologies, our graphene heterodyne sensor presents a number of distinct advantages. First, it is a dipole-detection based technique, and does not involve the slow charge transfer processes. By operating at high frequencies we also avoid the slow dynamics of interface trap states. Therefore, the sensing response time can be tremendously improved. Second, unlike chemi-capacitive impedance sensors, the high transconductance of graphene transistor provides intrinsic gain for signal amplification.

Since, graphene can be synthesized on wafer-scale and is fully compatible with existing top-down fabrication technology and on-chip electronic circuitry, the next step towards practical applications is to integrate graphene heterodyne sensors with micro GC components. On the fundamental side, single-to-few molecule detection can be easily achieved by scaling down the channel region, opening a door for fundamental studies of individual molecular events with unprecedented precision.

References

[1] D. V. Lim, J. M. Simpson, E. A. Kearns, and M. F. Kramer, Clinical Microbiology Reviews **18**, 583 (2005).

[2] T. Shigemori, The 14th International Meeting on Chemical Sensors (2012).

[3] J. Carrano, 2004.

[4] A. R. Clifford K. Ho, David R. Miller, and Mary J. Davis, Sensors for Environmental Monitoring and Long-Term Environmental Stewardship, 2004.

[5] S. Lee, K. Lee, and Z. H. Zhong, Nano Letters **10**, 4702 (2010).

[6] X. S. Li *et al.*, Science **324**, 1312 (2009).

[7] S. Bae *et al.*, Nature Nanotechnology **5**, 574 (2010).

[8] J. M. M. Harold M. McNair, *Basic Gas Chromatography* (John Wiley and Sons, New Jersey, 2009).

[9] E. F. B. Robert L. Grob, *Modern Practice of Gas Chromatography* (John Wiley and Sons, New Jersey, 2004).

[10] V. A. Sazonova, PhD thesis, Cornell University, 2006.

[11] S. Das Sarma, S. Adam, E. H. Hwang, and E. Rossi, Reviews of Modern Physics **83**, 407 (2011).

[12] F. Schedin, A. K. Geim, S. V. Morozov, E. W. Hill, P. Blake, M. I. Katsnelson, and K. S. Novoselov, Nature Materials **6**, 652 (2007).

[13] F. K. Perkins, A. L. Friedman, E. Cobas, P. M. Campbell, G. G. Jernigan, and B. T. Jonker, Nano Letters **13**, 668 (2013).

[14] V. Dua, S. P. Surwade, S. Ammu, S. R. Agnihotra, S. Jain, K. E. Roberts, S. Park, R. S. Ruoff, and S. K. Manohar, Angewandte Chemie-International Edition **49**, 2154 (2010).

[15] J. Li, Y. J. Lu, Q. Ye, M. Cinke, J. Han, and M. Meyyappan, Nano Letters **3**, 929 (2003).

[16] C. Y. Lee and M. S. Strano, Langmuir **21**, 5192 (2005).

[17] W. Kim, A. Javey, O. Vermesh, O. Wang, Y. M. Li, and H. J. Dai, Nano Letters **3**, 193 (2003).

[18] S. Kar, A. Vijayaraghavan, C. Soldano, S. Talapatra, R. Vajtai, O. Nalamasu, and P. M. Ajayan, Applied Physics Letters **89**, 132118 (2006).

[19] Y. Paska and H. Haick, Acs Applied Materials & Interfaces **4**, 2604 (2012).

[20] H. M. Wang, Y. H. Wu, C. X. Cong, J. Z. Shang, and T. Yu, Acs Nano **4**, 7221 (2010).

[21] D. Estrada, S. Dutta, A. Liao, and E. Pop, Nanotechnology **21** (2010).

[22] Y. Dan, Y. Lu, N. J. Kybert, Z. Luo, and A. T. C. Johnson, Nano Letters **9**, 1472 (2009).

[23] C. Y. Lee, R. Sharma, A. D. Radadia, R. I. Masel, and M. S. Strano, Angewandte Chemie-International Edition **47**, 5018 (2008).

[24] C. Y. Lee and M. S. Strano, Journal of the American Chemical Society **130**, 1766 (2008).

[25] E. S. Snow, F. K. Perkins, E. J. Houser, S. C. Badescu, and T. L. Reinecke, Science **307**, 1942 (2005).

[26] E. K. Yu, D. A. Stewart, and S. Tiwari, Physical Review B **77** (2008).

[27] B. Kumar *et al.*, Nano Letters **13**, 1962 (2013).

Chapter 6

Electrical probing and tuning of vapor-graphene interaction dynamics

6.1 Introduction

The behavior of molecules near a surface is dictated by the interplay of forces of attraction and repulsion between the two. Understanding the nature of such interactions is of great significance, and can lead to efficient design of complex physicochemical processes. The interaction between a molecule and a surface is either chemical (covalent/ionic) or physical (non-covalent). Covalent interactions involve sharing of electrons with or without partial charge transfer between two systems, and are strong with interaction energies between 1-10 eV. On the other hand, electrostatic non-covalent interactions have interaction energy of only a few 100 meVs (Figure 6-1). Even though non-covalent interactions are weak, they are precise in nature, work in a time dependent manner and are the bedrock of most biological and cellular processes [1,2]. In fact, non-covalent interactions control diverse phenomena like base-pair stacking, protein-nucleic acid recognition, self-assembly, catalysis, etc. [3-7]; and understanding them can usher new scientific and technological breakthroughs.

Nanoelectronic systems are perfect platforms to study and mimic the physicochemical nature of such interactions owing to their large surface-to-volume ratio, exceptional electronic properties and chemical stability in different environments [8-11]. To date, nanoelectronic systems have been used to demonstrate rapid and

sensitive molecular recognition as discussed in Chapter 2, however, the fundamental interaction mechanism between molecules and pristine nanomaterial is still little understood. The reason is that most conventional nanoelectronic systems detect charge transfer (Chapter 2 and the references therein) at defect sites which do not represent the true nature of interaction between charge neutral molecules and nanomaterials.

Here, the heterodyne sensing technique we have developed stands out, as it monitors dipole-moment induced electrical change which is independent of charge transfer processes and hence, can provide insight into non-covalent interactions at the nanomaterial surface. The fast, sensitive and reversible nanoelectronic heterodyne responses (Chapter 5) allow us to monitor vapor kinetics near a nanomaterial surface in real-time revealing the dynamics of their interaction. Moreover, the added advantage of using nanoelectronic platforms is the ability to electrically tune the charge density and hence, the Fermi level in them via an electrostatic gate [8-11], thereby providing another parameter to tune fundamental interactions. The realistic range of gate control over Fermi levels in carbon nanotube, graphene and MoS_2 is between ± 0.5 eV as shown in Figure 6-1 where we compare it with the typical intermolecular interaction energy range. Graphene due to its linear band structure provides a continuous range of gate tuneable energies [12] (Figure 6-1).

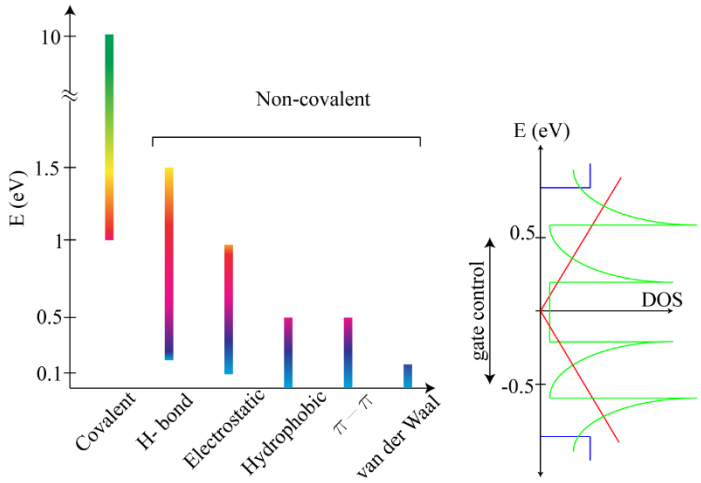

Figure 6-1. Interaction energy range for covalent and non-covalent intermolecular interactions. On the right is plotted the typical density of states for common 1-dimensional (carbon nanotube; green) and 2-dimensional (graphene; red and MoS_2; blue) with charge carrier energy levels.

In this chapter, we discuss the utilization of graphene nanoelectronic heterodyne mixer as a tool to probe vapor molecule-graphene interaction kinetics in real-time, quantify the binding affinities and demonstrate electrical tuning of this interaction. We start with a brief description of generally used experimental methods to determine interaction affinities at a surface in Section 6.2. Next, we discuss the measurement setup used in our work (Section 6.3) followed by the temperature dependent desorption spectroscopy results of various polar molecules on graphene in Section 6.4. In Section 6.5, we demonstrate the electrical tuning of vapor molecule interaction on graphene using the electrostatic back gate of the graphene FET. In Section 6.6, we discuss the experimental observations of interaction of aromatic molecules with graphene.

6.2 Thermodynamics and kinetics of molecule-surface interaction

When a gas molecule approaches a substrate, it binds to the surface thereby reducing the surface energy. This is referred to as the adsorption process. This binding

can be strong (chemical) or weak (physical), and the competition of the binding energy with thermal fluctuations determines the ability of molecules to reside on the surface after which they desorb [13]. To measure the adsorption thermodynamics, micro-calorimetry is generally used [14]. Chemical processes are exothermic or endothermic and hence for a chemical event, there is always heat produced or consumed. In micro-calorimetry study, the rate of heat flow to or from a sample over time is analyzed to calculate the total amount of heat consumed or released for a process. In micro-calorimetry, this represents the negative of adsorption enthalpy ($-\Delta H_{ads}$). Even though micro-calorimetry is used to study a broad range of chemical and biological processes, it still is time consuming requiring hours to days.

The molecule-surface interaction strength can also be studied by analyzing the equilibrium adsorption/desorption pressure at different temperatures for a constant surface coverage [15]. The adsorption enthalpy, ΔH_{ads} is then given by the Clausius-Clapeyron equation:

$$\left(\frac{\partial \ln P}{\partial(1/T)}\right)_{\Theta} = \frac{\Delta H_{ads}}{R}, \qquad \text{Equation 6-1}$$

where P is the pressure and T is the temperature for the surface coverage Θ, and R the ideal gas constant. For small molecules, the physisorption enthalpy reflects the adsorbate binding energy, E_b within ~ RT [16], therefore $\Delta H_{ads} \sim E_b$.

The third way to determine thermodynamic binding parameters is from the temperature dependence of molecular desorption at different temperature ramp-rates [13]. As the substrate temperature is increased, rate at which molecules leave the surface is increased and peaks at a particular temperature, after which the surface is depleted. By analyzing the mass of (or pressure due to) desorbed species with

temperature one can determine the activation energy for desorption, E_{a} using Redhead analysis. For a first-order process, the desorption energy is given by,

$$\frac{E_a}{R} = \frac{v_0}{\sigma\alpha} e^{-E_{\mathrm{a}}/RT_p} , \qquad \text{Equation 6-2}$$

where v_0 is a pre-exponential factor,σ the adsorbate concentration,α the temperature ramp rate and T_p, the temperature at which peak desorption rate is observed. In absence of re-adsorption and a negligible adsorption barrier, $E_{\mathrm{a}} = -\Delta H_{ads}$, which is also the binding energy, E_b. This is the principle of temperature desorption spectroscopy [13].

The thermodynamics of adsorption-desorption events can also be derived from the temperature dependence of kinetics of this interaction [13]. The desorption rate from a surface, r_{des} $(= -\frac{dN}{dt})$ is related to the amount of adsorbed species, N through the rate equation: $r_{des} = k_{des}N$ which can also be written as $-\frac{dN}{dt} = k_{des}N$. Solving the two expressions, we have

$$r_{des} = Ae^{-k_{des}t}. \qquad \text{Equation 6-3}$$

For molecular adsorption and desorption on nanoelectronic surface, the electrical response also follows the above rate since it is proportional to the number of adsorbed molecules on surface at any time. Exponential fits to electrical response, hence can give us the desorption rate constant k_{des}. From transition state theory [13], desorption activation barrier, E_{a} and the desorption rate constant, k_{des} are related as:

$$k_{des} = v_f e^{-(\frac{E_a}{k_B T})} , \qquad \text{Equation 6-4}$$

where v_f is the attempt frequency, k_B the Boltzmann constant, and T the temperature. The temperature dependence of desorption rate constant can be studied to obtain the activation barrier, E_{a} which is equal to the adsorbate binding energy.

Nanoelectronic devices are excellent transducers and as molecules adsorb-desorb on a nanomaterial surface, the chemical interaction energy is converted to an electrical response. The chemo-electrical response from thermally-activated molecular desorption can also be analyzed to study the dynamics of molecule-nanomaterial interaction and estimate the binding parameters. In particular, the 2-dimensional planar structure of graphene makes it an ideal system to study such molecular events. In Chapter 5, we demonstrated graphene heterodyne vapor sensors which are fast, sensitive and reversible. The fast responses allow us to monitor vapor kinetics near the graphene surface in real-time while high sensitivity promises the ability to monitor dynamics of extremely low concentrations of chemical species. The reversible responses are inherent to the heterodyne mixing technique as it detects the dipole moment of the physisorbed species and not the associated charges. Therefore, heterodyne measurement of thermal desorption events can reveal the true nature of non-covalent interactions between vapor molecules and graphene surface. In the following sections we study the kinetics of vapor-graphene interaction.

6.3 Thermal desorption measurement setup

The graphene field-effect-transistor fabrication process is presented in Section 5.2. Gas chromatography setup is used to provide sub-second wide vapor pulses for dynamic study of vapor molecules on graphene. The vapor delivery system is detailed in Section 5.3 and the heterodyne electrical measurement setup is described in detail in Section 5.6. For temperature dependent desorption measurement, the silicon die with graphene-FETs was mounted on top of a solid state cooler (Vktech TEC1-12706) using a silver paste (Artic Silver 5 thermal compound). The temperature of the solid state cooler was controlled by a DC power supply (Yihua-YH305D) and was calibrated

using a K-type thermocouple (Amico) at each voltage. Figure 6-2 shows the close up of the actual device where the solid state cooler (white) acts as a base on which the silicon die is mounted. The three electrical probes (source, drain, and gate) can also be seen. The vapor molecules are delivered through a 70 cm long column using helium as the carrier gas at a flow rate of 8 mL/min.

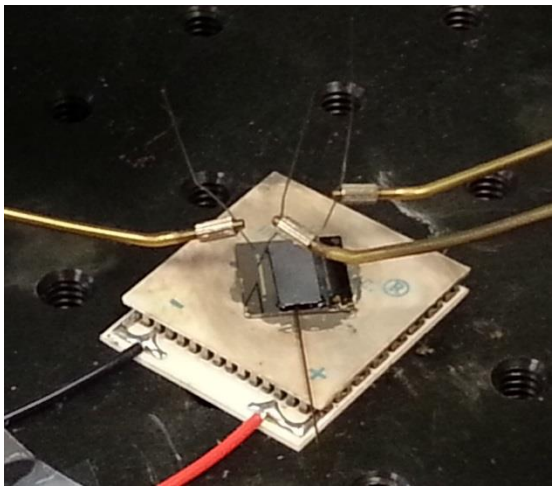

Figure 6-2. Image of the temperature measurement setup. The temperature of solid state cooler (white base) is controlled by a voltage between the two leads (red and black). The silicon die is mounted using silver paste for efficient thermal contact. The die is encapsulated with a flow channel and the vapor delivery column can also be seen. The three probes are source, drain and gate for the graphene field-effect-transistor.

6.4 Estimation of vapor molecule binding energy on graphene

The heterodyne mixing response of graphene to 285 ng chloroform and 4.72 ng *N, N*- dimethylformamide (DMF) is shown in Figure 6-3. We observe that (i) the heterodyne response of graphene to these molecules is opposite and (ii) the response is reversible and consists of an instantaneous rise (fall for DMF) followed by a desorption event. The opposite response of these molecules is related to the orientation of their molecular dipoles with respect to the graphene plane as detailed in chapter 5. Following first order rate kinetics, $r_{des} = Ae^{-k_{des}t}$ from Equation 6-3, the fast desorption curve

can be fit with an exponential to obtain the desorption rate, k_{des} or desorption time, τ_{des} (k_{des} = $1/\tau_{des}$) as illustrated in Figure 6-3. In all our experiments, desorption was dominated by a fast exponential decay followed by a slow return to baseline.

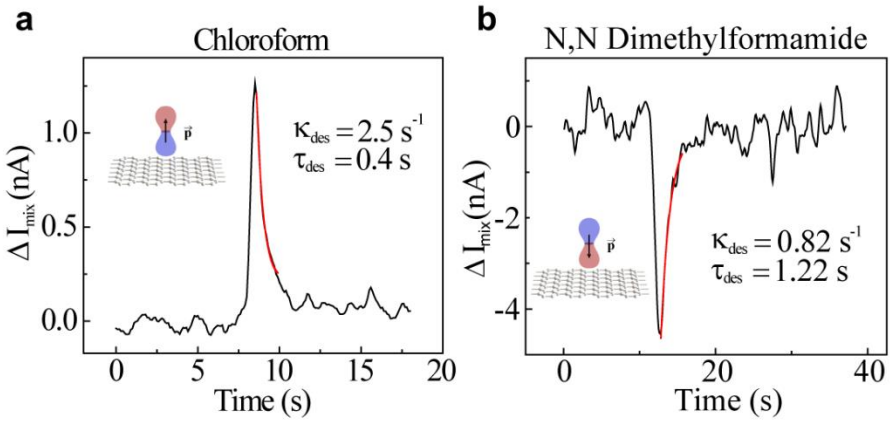

Figure 6-3. Heterodyne mixing response of graphene to **(a)** 285 ng chloroform and **(b)** 4.72 ng DMF. Exponential fits (in red) to decay curves yield desorption rates k_{des} = 0.25 s^{-1} and 0.82 s^{-1} for chloroform and DMF respectively. The parameters for the measurement were - back gate voltage, V_g = 0 V and temperature, T = 296.2 K. Inset in (a) and (b) show the orientation of respective molecule's dipole on top of graphene.

In order to determine the thermodynamic binding energy of molecules on graphene, we study the temperature dependence of desorption kinetics as detailed in Section 6.2. In the absence of charge transfer, the weak interactive forces determine the ability of a molecule to adsorb onto graphene surface. The competing electronic repulsive forces and attractive van der Waals forces lead to the formation of a potential energy well, the minima of which determines the binding energy of molecule to graphene [17]. By providing enough thermal energy this barrier (desorption) can be overcome. In the following sections, we present the binding energy study of small polar molecules and aromatic compounds on graphene.

6.4.1 Small polar organic molecules

In Figure 6-4, we plot the normalized graphene FET response to dimethylmethylphosphonate (DMMP) at different substrate temperatures. We clearly observed that with increasing temperatures, the molecular desorption process is fastened and the time required for signal response to reach baseline decreases as the substrate temperature is elevated. The graphene FET channel dimensions were L = 1 µm, W = 1 µm, and back gate voltage was held at V_g = 0V.

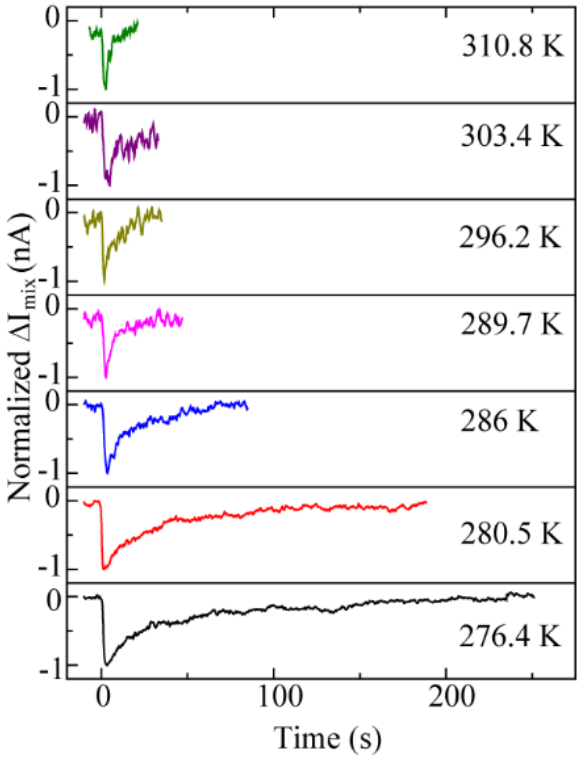

Figure 6-4. Normalized temporal response of graphene mixer to 1.145 ng DMMP at different temperatures.

Next, we carried out a detailed study of graphene FET response at different temperatures with repeated doses of 1.145 ng DMMP (Figure 6-5a). Above 310.8 K substrate temperature, the signal response for DMMP injection was within the noise

floor. In Figure 6-5b, we plot the peak response values obtained from Figure 6-5a, with temperature. The fall in graphene FET peak response values is a direct manifestation of the enhanced desorption since at higher substrate temperature the net molecular adsorption flux is reduced to zero [18]. From a thermodynamic argument, physisorption (and therefore the graphene response) increases when low temperature compensates for the fall in enthalpy and entropy as molecules adsorb, in order to keep the process spontaneous (Gibbs free energy, $\Delta G < 0$). An exponential fit to the desorption curves in Figure 6-5a yields corresponding desorption rate constants, at each temperature. In Figure 6-6 we present these desorption rate constants as an Arrhenius plot with temperature. The slope of the $\ln(k_{des}) - {}^{1}/_{T}$ plot gives the binding energy of DMMP on graphene which is 734 ± 52 meV.

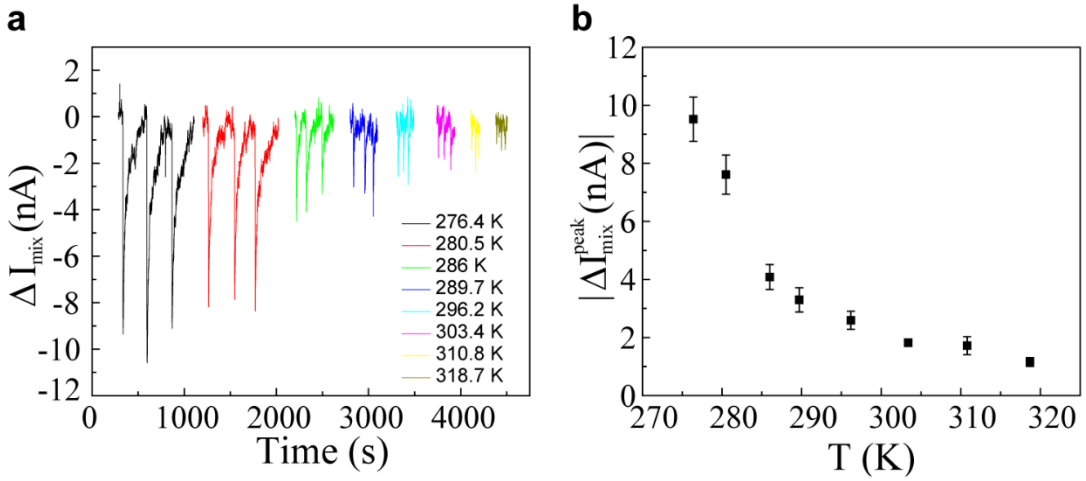

Figure 6-5. **(a)** Temporal response of graphene mixer to repeated doses of 1.145 ng DMMP injection at different temperatures. **(b)** Temperature dependence of peak mixing current responses in (a). These measurements were done on graphene FET with L = 1 µm, W = 1 µm, and back gate voltage was held at V_g = 0V. Error bars in (b) show the standard deviation over 3 runs. All measurements were carried out at atmospheric pressure.

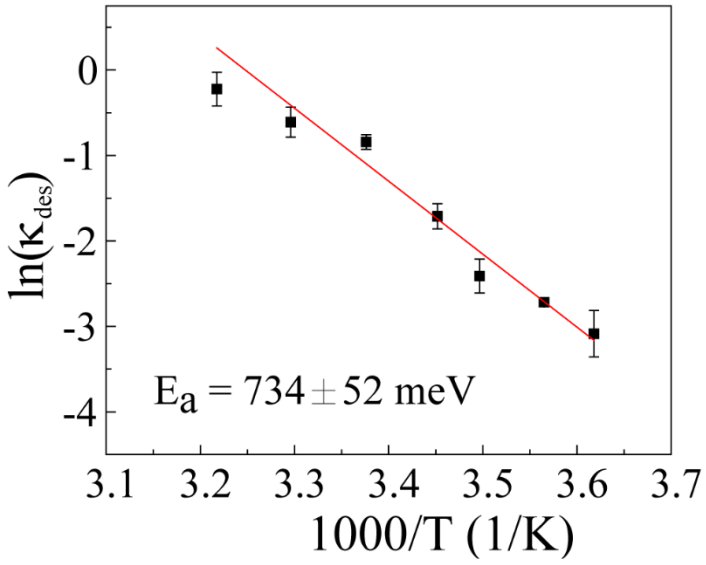

Figure 6-6. Desorption rates, k_{des} obtained by exponential fit of curves in Figure 6-5a plotted with temperature on Arrhenius scale $\ln(k_{des}) - {}^{1}/_{T}$. Slope of this plot is obtained from a linear fit (in red) which gives non-covalent binding energy of 734 ± 52 meV.

Similar temperature-dependent desorption fits for chloroform, dichloromethane and DMF yield binding energies of 223 ± 13 meV, 195 ± 10 meV and 657 ± 23 meV respectively as shown in Figure 6-7. For DMF, we chose a smaller temperature range as at lower temperatures desorption was extremely slow (~hours) and successive injections were carried out during the slow phase of desorption for lower temperatures. These measurements were done on graphene FET with L = 1 µm, W = 1 µm for chloroform; L = 5 µm, W = 1 for dichloromethane and L = 2 µm, W = 2 for DMF. The back gate voltage was held at V_g = 0V for all the measurements.

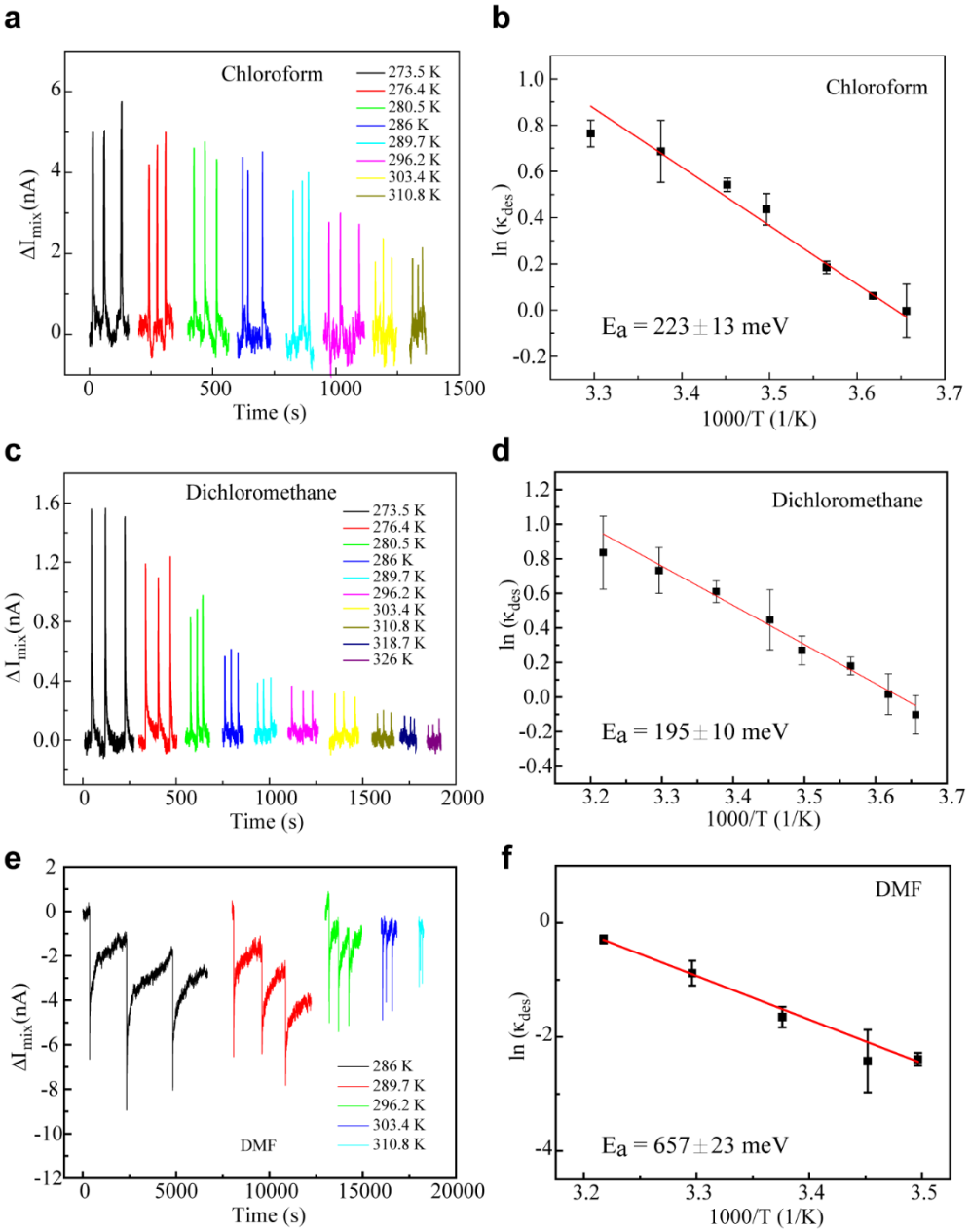

Figure 6-7. Temperature dependent desorption for small molecules. Temperature dependence of graphene-FET response to repeated doses of (1.428 µg) chloroform, (1.329 µg) dichloromethane and (28 ng) DMF. **(a)**, **(c)**, **(e)** represent the temporal response of graphene-FET at different temperature to chloroform, dichloromethane and DMF. **(b)**, **(d)**, **(f)** show the Arrhenius plot of desorption rate constants at each temperature obtained from exponential fits of all the curves in (a), (c) and (e) respectively. Linear fits to these curves are in red. Error bars show the standard deviation over 3 runs.

6.4.2 Aromatic molecules

Non-covalent modification of graphene lattice with aromatic chemical compounds is widely pursued to enhance or tailor the electronic and optical properties of graphene [19]. The planar sp^2-hybridized graphene lattice also makes it a perfect substrate to study π-π interactions, which has been a topic of intense research, albeit mostly theoretical and controversial [20-22]. Here, we choose chlorobenzenes as model systems to study arene-graphene interaction. Figure 6-8 represents the normalized graphene-FET response to 130 ng injection of 1, 2- dichlorobenzene (DCB) at different substrate temperatures.

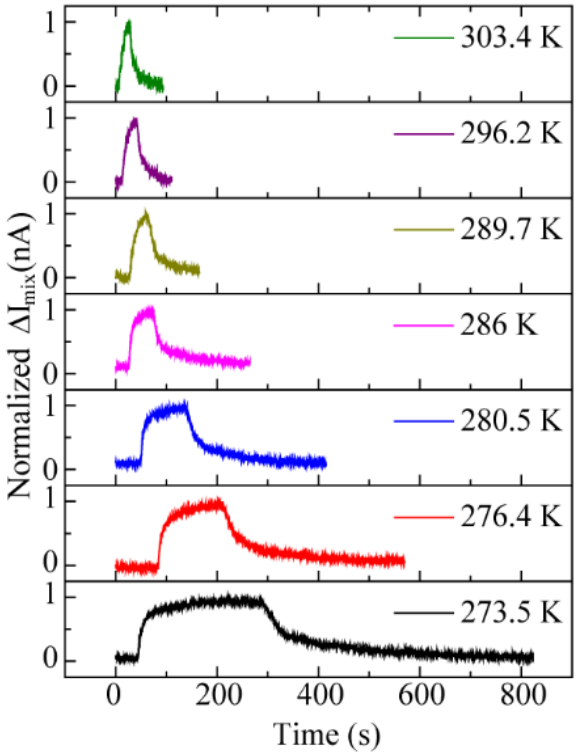

Figure 6-8. Normalized temporal response of graphene mixer to 130 ng 1, 2-DCB at different temperatures. The graphene FET channel dimensions were L = 5 µm, W = 1 µm, and back gate voltage was held at V_g = 0V.

The temperature dependence desorption trend for DCB agrees with the other small molecules reported earlier, where faster desorption with increasing temperatures was observed. In Figure 6-9a, we plot the temporal response of graphene FET to repeated doses of 130 ng DCB at different temperatures. Above 326 K substrate temperature, the signal response for DCB injection was within the noise floor. In Figure 6-9b, we plot the peak response values obtained from Figure 6-9a, with temperature.

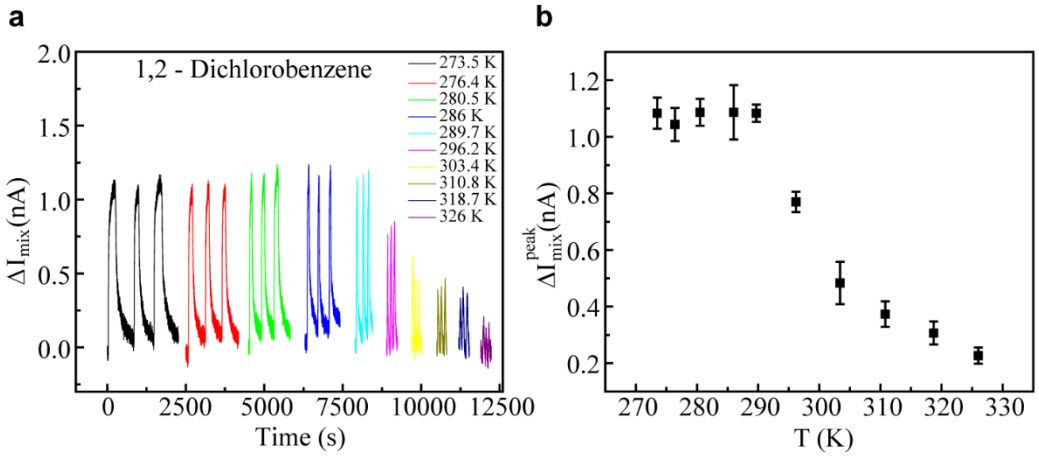

Figure 6-9. **(a)** Temporal response of graphene mixer to repeated doses of 130 ng 1, 2-DCB injection at different temperatures. **(b**) Temperature dependence of peak mixing current responses in (a). These measurements were done on graphene FET were L = 5 µm, W = 1 µm, and back gate voltage was held at V_g = 0V. Error bars in (b) show the standard deviation over 3 runs. All measurements were carried out in air and at atmospheric pressure.

Interestingly, the peak mixing current response to DCB is observed to saturate at lower temperatures. This is due to surface saturation with a layer of DCB which causes steric hindrance to accommodate more DCB molecules on graphene. This is observed in the saturation of sensor responses at higher concentrations as well (Chapter 5). An exponential fit to the desorption curves in Figure 6-9a yields corresponding desorption rate constants, at each temperature. In Figure 6-10, we present these

desorption rate constants as an Arrhenius plot with temperature. The slope of the $\ln(k_{des}) - {}^{1}/_{T}$ plot gives the binding energy of DCB on graphene which is 447 ± 24 meV.

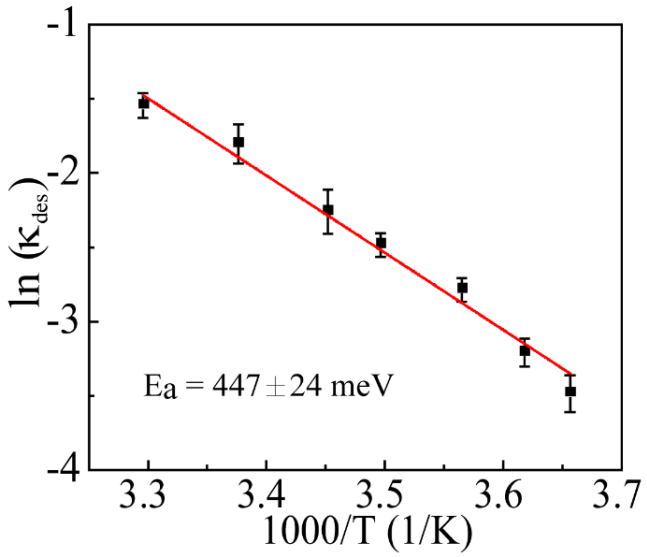

Figure 6-10. Desorption rates, k_{des} obtained by exponential fit of curves in Figure 6-9a plotted with temperature on Arrhenius scale $\ln(k_{des}) - {}^{1}/_{T}$. Slope of this plot is obtained from a linear fit (in red) which gives non-covalent binding energy of 447 ± 24 meV for DCB.

We studied another aromatic compound, chlorobenzene where we observed the same effect as 1, 2- DCB. For chlorobenzene also, the peak current saturates at lower temperature (below 289.7 K) as shown in Figure 6-11. The slope from Arrhenius plot for chlorobenzene Figure 6-11c gives us a binding energy of 367 ± 30 meV. The graphene FET channel dimensions were L = 1 µm, W = 1 µm, and back gate voltage was held at V_g = 0V.

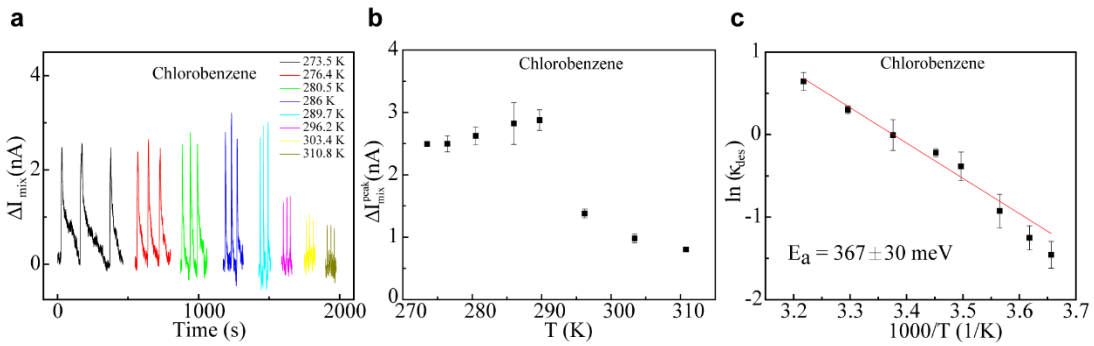

Figure 6-11. **(a)** Temperature dependent mixing current response to repeated doses of 109 ng chlorobenzene. **(b)** Peak response values for chlorobenzene from (a) plotted with temperature. **(c)** Arrhenius plot of desorption rate constants at each temperature obtained from exponential fits of all the curves in (a). Linear fits to these curves are in red. Error bars show the standard deviation over 3 runs.

6.5 Electrical tuning of vapor-graphene interaction

Temperature control of molecule-substrate interaction provides rich insight into the fundamental binding parameters however, on-chip thermal management (especially cooling) in micro and nano-environments has practical limitations [23]. The biggest advantage of using nanoelectronic systems is the ability to tune the charge density and hence the Fermi level in them, which can be employed to electrostatically control non-covalent interactions, given the practical limitations of localized thermal management on-chip. Here, we modify Equation 6-4 as

$$k_{des} = \nu_f e^{-\left(\frac{E_a^0 + \beta \Delta E_F}{k_B T}\right)}, \qquad \text{Equation 6-5}$$

where E_a^0 is the activation barrier for charge neutral nanomaterial and ΔE_F is the electrostatic contribution to the energy barrier due to the Fermi level shift from the charge neutral point. β is the gate-activation factor, which denotes contribution of gate to changing the activation energy barrier. This flexibility is missing in conventional

metallic or insulating substrates used generally in kinetic studies. In a three terminal device, the back gate terminal provides a knob to control the Fermi level in the device.

To study the gate-dependence of graphene response, we choose two representative molecules; chloroform and DMF. Figure 6-12a, b show the $I - V_g$ characteristics of the device used for chloroform and DMF, respectively. The graphene channels are initially p-doped and the corresponding charge neutrality points, V_D can be used to determine the Fermi level, E_F at each gate voltage, V_g using the expression [12],

$$E_F = \hbar v_F \sqrt{\pi n}\,, \qquad \text{Equation 6-6}$$

where $\hbar$ is the Planck constant and v_F, the Fermi velocity in graphene. n is the charge density of graphene given by $n = \left|\frac{C_{bg}(V_g - V_D)}{e}\right|$, where $C_{bg} = \frac{\varepsilon_r \varepsilon_0}{d}$ is the back-gate capacitance for graphene device on d = 60 nm thick silicon oxide (ε_r=4). In Figure 6-12c, d graphene mixer response to (285 ng) chloroform and (18.8 ng) DMF at different gate voltages is plotted. In Figure 6-12e, d we plot peak response values from Figure 6-12c, d respectively with the corresponding graphene Fermi levels calculated from Equation 6-6.

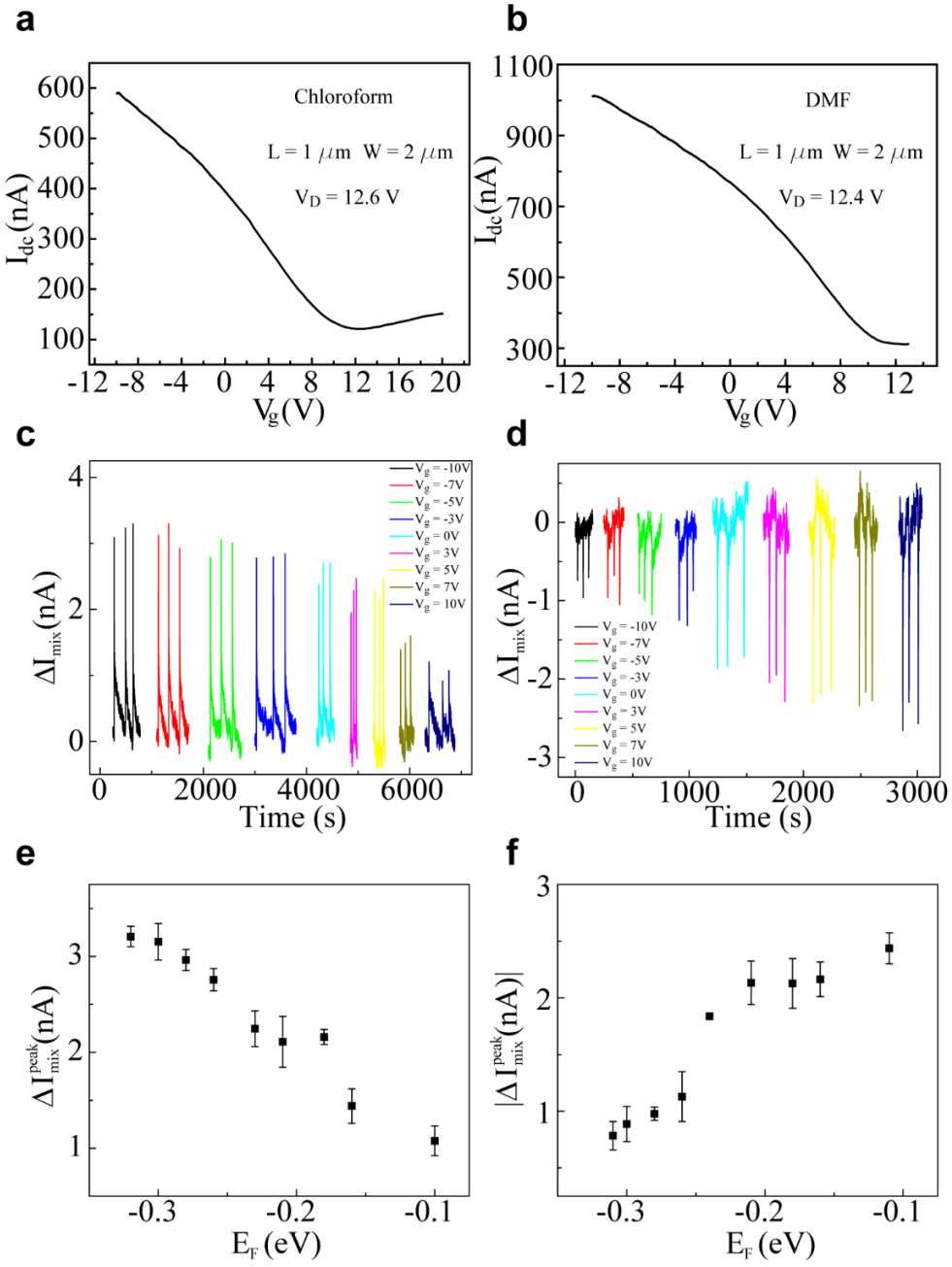

Figure 6-12. DC electrical transport characteristics for the devices used for back-gate tuning measurement for **(a)** chloroform and **(b)** DMF. The device dimensions and the charge neutrality point (V_D) are mentioned in the figure for each device. The source-drain voltage, V_{sd} = 1mV. Temporal response to repeated doses for **(c)** 285 ng chloroform and **(d)** 18.88 ng DMF plotted with different gate voltage. **(e)** and **(f)**, Peak responses for chloroform and DMF from (c) and (d) plotted with the corresponding Fermi level of the graphene device in (a) and (b) respectively.

We observe that graphene back-gate response has the opposite trend for chloroform and DMF in Figure 6-12, which have opposite dipole orientations on top of graphene, as discussed previously in Chapter 5. As we increased the gate voltage, the signal response to chloroform decreased, while for DMF it increased. The back gate can affect the interaction by either the unscreened field directly attracting (repulsing) the molecules to (from) the graphene surface, or the field induced carrier doping in graphene leading to enhanced electrostatic attraction/repulsion between the molecules and graphene charge carriers. For chloroform, which has the electronegative side closer to graphene, a positive gate voltage will cause the unscreened electric field to attract more molecules towards the graphene surface. This will lead to an increase in signal response with positive gate voltages for chloroform, while the same mechanism will lead to a decrease in signal response for DMF. However, we observed a completely opposite trend to this as shown in Figure 6-12. Therefore, this effect is attributed to the shift in Fermi levels due to gate electric field induced carrier doping. For chloroform, increasing positive gate voltage causes enhanced electrostatic repulsion between the electronegative side of chloroform and less p-doped (more n-doped) graphene, and the $\Delta I_{mix} - E_F$ trend in Figure 6-12 is exactly opposite for DMF.

The increasing graphene Fermi levels also influence the interaction times between chloroform (DMF) and graphene. As the Fermi level increases, the increasing repulsion (attraction) between chloroform (DMF) and graphene leads to faster (slower) desorption (slower) highlighting the ability to electrically tune absorbate-graphene interactions. This is evident in the Fermi level dependence of desorption times, τ_{des} as seen in Figure 6-13a, b.

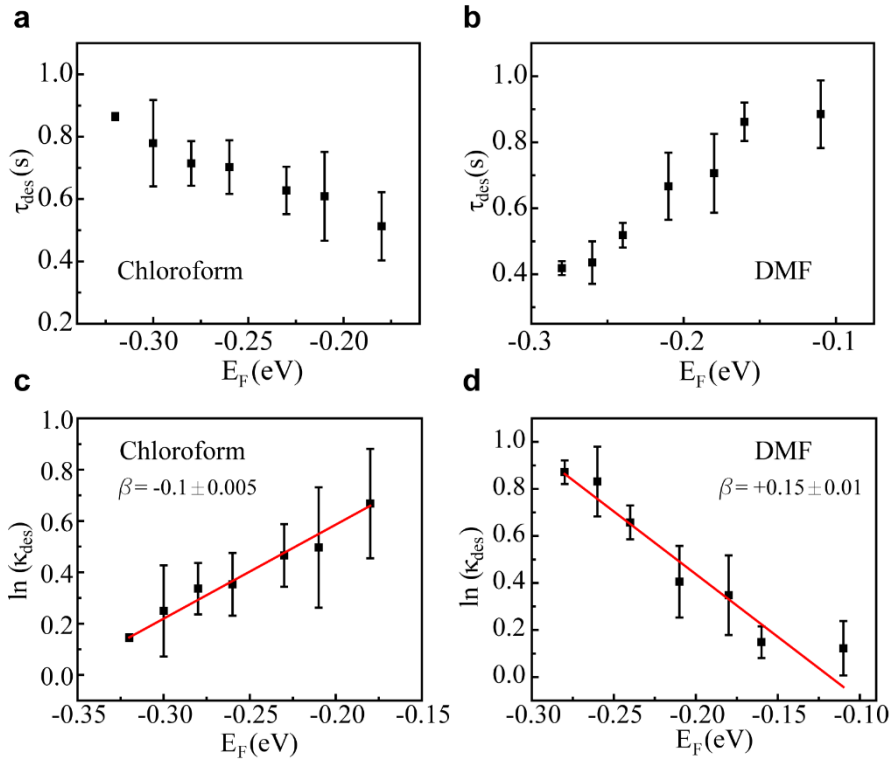

Figure 6-13. **(a)** and **(b)** Desorption times ($\tau_{des} = 1/k_{des}$) obtained from the exponential fits to the mixing current responses of Figure 6-12c, d, plotted with graphene Fermi level for chloroform and DMF respectively. **(c)** and **(d)** Desorption rate constants for chloroform and DMF respectively, plotted with graphene Fermi levels at different gate voltages. The slope of $\ln k_{des} - E_F$ plot gives us the gate-activation barrier from Equation 6-7. Error bars show the standard deviation over 3 runs. All measurements were carried out in air, at atmospheric pressure and room temperature.

To determine the gate-activation factor, β we revisit Equation 6-5 and express it as:

$$\ln k_{des} = \left(\ln v_f - \frac{E_a^0}{k_B T}\right) - \frac{\beta}{k_B T}\Delta E_F \,, \qquad \text{Equation 6-7}$$

where the slope of $\ln k_{des}$ – ΔE_F curve yields β. In Figure 6-13c, d we plot the logarithmic dependence of desorption rate constant with the Fermi level of the devices in Figure 6-12a, b respectively. The linear fit to these curves (in red) gives us the gate-activation factor, β ~ -0.1±0.005 and β ~ + 0.15±0.01 for chloroform and DMF, respectively.

6.6 $\pi - \pi$ interaction between aromatic molecules and graphene

The effect of back gate terminal on the interaction of aromatic compounds and graphene can help understand the complex interplay of dispersive van der Waal forces and the electrostatic π- π forces. In Figure 6-14b we plot the temporal response of graphene device in Figure 6-14a, to repeated doses of 13 ng 1, 2-DCB at different gate voltages. We plot the peak mixing response of the device in Figure 6-14c.

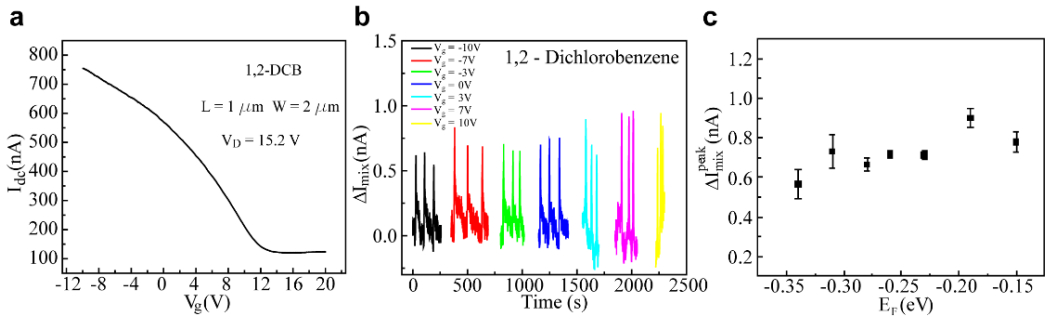

Figure 6-14. **(a)** DC electrical transport characteristics for the device used for back-gate dependence of 1, 2 – DCB. The device dimensions and the charge neutrality point (V_D) are mentioned. The source-drain voltage, V_{sd} = 1mV. **(b)** Temporal response of graphene device in (a) to repeated doses of 13 ng 1, 2 – DCB at different gate voltages. **(c)** Peak response of graphene device in (b) plotted with the Fermi level at different gate voltages calculated from Equation 6-6.

We observe that the Fermi level shift has a relatively weak effect on DCB-graphene interaction as seen in Figure 6-14c, where graphene response increases only slightly even with a ΔE_F shift of ~200 meV. We see similar behavior to chlorobenzene, which also is an aromatic compound with π-electrons. Figure 6.15 shows the gate dependence of graphene FET to chlorobenzene.

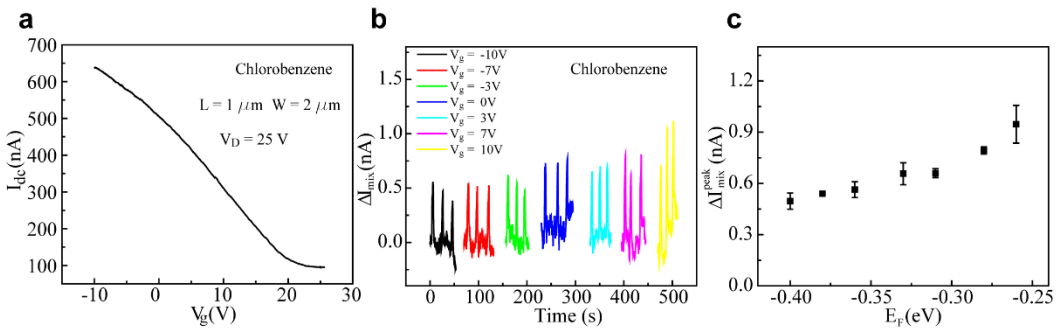

Figure 6-15. **(a)** DC electrical transport characteristics for the device used for back-gate dependence of chlorobenzene. The device dimensions and the charge neutrality point (V_D) are mentioned. The source-drain voltage, V_{sd} = 1mV. **(b)** Temporal response of graphene device in (a) to repeated doses of 54.5 ng chlorobenzene at different gate voltages. **(c)** Peak response of graphene device in (b) plotted with the Fermi level at different gate voltages calculated from Equation 6-6.

DCB and chlorobenzene have a dipolar orientation with electronegative side closer to graphene, hence one would expect the behavior of back gate tuning to be similar to chloroform where we see a clear gate dependence (Figure 6-12). To understand this we look at the orientation of aromatic molecules on graphene. The lowest energy configuration for DCB and chlorobenzene on graphene is offset parallel stacking [24] where the π- π repulsion leads to the aromatic compound being offset from a complete π- π overlap, with the local polar C-Cl bonds lie directly atop the graphene π- electron cloud [21,22]. This is represented in Figure 6-16. In such a case, as the electron density of graphene increases, the dispersive interaction between local polar C-Cl bonds and graphene π-electrons increases. However, at the same time the offset π-π repulsion between the two systems also increases as the systems tend to come closer. Because the polar bonds are closer to the π-electrons of graphene, the dispersive interaction dominates [22], though the increase in graphene mixing current response is only slight.

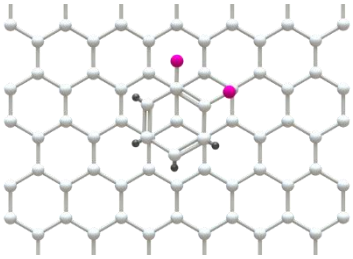

Figure 6-16. Offset stacked structure of 1, 2-dichlorobenzene on graphene.

The weak effect of back-gate is also observed in desorption times of chlorobenzene and DCB from graphene. In Figure 6-17a, c, desorption time, τ_{des} from the exponential fits to device response in Figure 6-14 and Figure 6-15 is plotted with the Fermi level shift. We also calculate the gate-activation factor, β from linear fits to $\ln k_{des} - E_F$ shown in Figure 6-17b and d.

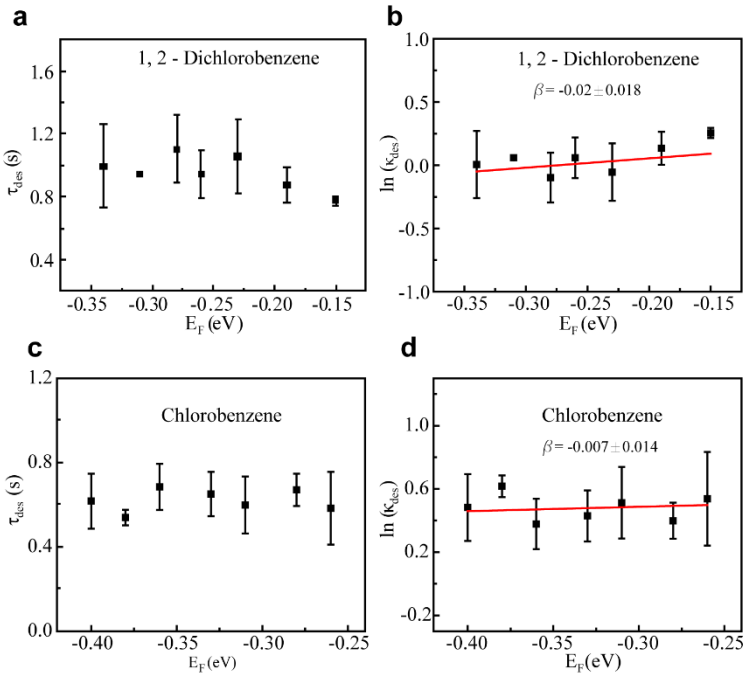

Figure 6-17. **(a)**, **(c)** Desorption times ($\tau_{des} = 1/k_{des}$) for 1, 2-DCB and chlorobenzene obtained from the exponential fits to the mixing current responses in Figure 6-14b and Figure 6-15b respectively, plotted with graphene Fermi level. **(b)**, **(d)** Estimation of gate-activation factor from the slope of linear fits (in red) to $\ln k_{des} - E_F$ curves for 1, 2 – DCB and chlorobenzene respectively.

6.7 Theoretical estimate of electrostatic and van der Waal contribution to molecule graphene interaction

The total non-covalent interaction energy is sum of electrostatic and van der Waal contributions which can be written as:

$$w_{Total}(h) = w_{elec} + w_{vdw} \,. \qquad \text{Equation 6-8}$$

Here, the electrostatic energy, comprises of the repulsive quantum mechanical interaction due to wave-function overlap ($\frac{A}{r^{12}}$) and the electrostatic interaction, $w_n$between a dipole and sheet of charges (graphene).

We first start by looking at the interaction energy, w_n between graphene and a dipole. Consider a ring of radius, x and thickness, dx on graphene as shown in Figure 6-18. The area of the ring of charges is,

$$dA = 2\pi x dx.$$

If *n* is the charge density per unit area in graphene, then

$$dQ = ne \times 2\pi x dx.$$

Now, interaction energy between a dipole $\vec{\boldsymbol{p}}$ (Figure 6-18) and ring of charges on graphene is given by,

$$dw_n(r) = -\frac{dQq}{4\pi\varepsilon\varepsilon_0}\left(\frac{1}{r-\frac{l}{2}sin\varphi}\right) + \frac{dQq}{4\pi\varepsilon\varepsilon_0}\left(\frac{1}{r+\frac{l}{2}sin\varphi}\right)$$

$$dw_n(r) = -\frac{dQq}{4\pi\varepsilon\varepsilon_0}\left[\frac{1}{r-\frac{l}{2}sin\varphi} - \frac{1}{r+\frac{l}{2}sin\varphi}\right]$$

$$dw_n(r) = -\frac{dQq}{4\pi\varepsilon\varepsilon_0}\left[\frac{lsin\varphi}{r^2-\frac{l^2}{4}sin^2\varphi}\right] \approx -\frac{dQ}{4\pi\varepsilon\varepsilon_0}\frac{p_y sin\varphi}{r^2}$$

$$dw_n(r) = -\frac{ne2\pi x dx}{4\pi\varepsilon\varepsilon_0}\frac{p_y sin\varphi}{r^2}$$

$$w_n(r) = \int_0^\infty -\frac{ne2\pi}{4\pi\varepsilon\varepsilon_0}\frac{p_y sin\varphi}{r^2}xdx = -\frac{p_y ne}{2\varepsilon\varepsilon_0}$$

Now, n is the charge density given by: $ne = -C_{bg}(V_g - V_d)$. Hence, we have

$$w_n(r) = \frac{p_y C_{bg}(V_g - V_d)}{2\varepsilon\varepsilon_0}\,. \qquad \text{Equation 6-9}$$

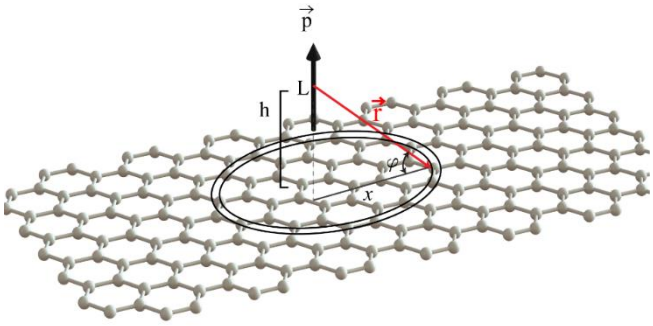

Figure 6-18. Diagrammatic representation of a dipole of length L on graphene sheet at a height of h.

More negative this energy, $w_n(r)$ more stable is the interaction. Considering chloroform dipole points up i.e. p_y = +1.04 D and DMF dipole points down, i.e. p_y = -3.82 D (see chapter 5); for a p-doped graphene-FET, clearly the electrostatic interaction for chloroform decreases and DMF increases with increasing positive gate voltages. From experimental results we see the same in Figure 6-12.

Next, we calculate the Van der Waal interaction energy w_{vdW}. The van der Waal interaction consists of dipole-dipole, dipole-induced dipole and induced dipole-induced dipole contributions. First we consider van der Waal interaction between two molecules with dipole moment $p_{i,i=1,2}$, polarizability $\alpha_{i,i=1,2}$ and ionization potentials $I_{i,i=1,2}$ and then consider interaction of a molecule and graphene sheet. From [17],

$$w(r) = -\frac{C_{dip-dip}}{r^6} - \frac{C_{dip-induced\ dip}}{r^6} - \frac{C_{induced\ dip-induced\ dip}}{r^6}$$

$$w(r) = -\frac{1}{r^6}\left(\frac{1}{(4\pi\varepsilon\varepsilon_0)^2}\frac{p_1^2 p_2^2}{3kT}\right) - \frac{1}{r^6}\left(\frac{p_1^2\alpha_2 + p_2^2\alpha_1}{(4\pi\varepsilon\varepsilon_0)^2}\right) - \frac{1}{r^6}\left(\frac{1}{(4\pi\varepsilon\varepsilon_0)^2}\frac{3}{2}\alpha_1\alpha_2\frac{I_1 I_2}{I_1 + I_2}\right).$$

Equation 6-10

This dependence of $w(r)$ on distance, r can be written as $w(r) = -\frac{C_{vdw}}{r^6}$.

To find the interaction with the entire graphene sheet we again consider a ring of radius x, and thickness dx. Given a graphene unit cell of area A_{uc}, the number of atoms in the ring of are dA (Figure 6-18) is given by

$$dN = 2\pi x dx \times \frac{2}{A_{uc}}.$$

Assuming all interactions are additive, we can integrate over the graphene sheet to get the total van der Waal interaction energy.

$$dw_{vdW}(h) = dN \times -\frac{C_{vdw}}{r^6}$$

$$w_{vdW}(h) = -\int_0^{\infty} \frac{2\pi x dx \times \frac{2}{A_{uc}} C_{vdw}}{r^6}. \qquad \text{Equation 6-11}$$

From Figure 6-18, $r^2 = x^2 + h^2$ and integrating Equation 6-11, we have

$$w_{vdW}(h) = -\frac{\pi C_{vdw}}{A_{uc}} \frac{1}{h^4}. \qquad \text{Equation 6-12}$$

Now, graphene dipole moment is zero, i.e. $p_1 = 0$, so from Equation 6-10

$$-C_{vdw} = -\frac{1}{(4\pi\varepsilon\varepsilon_0)^2}\left[p_2^2\alpha_1 + \frac{3}{2}\alpha_1\alpha_2\frac{I_1 I_2}{I_1 + I_2}\right].$$

Therefore,

$$w_{vdW}(h) = -\frac{\pi}{A_{uc}}\frac{1}{h^4}\frac{1}{(4\pi\varepsilon\varepsilon_0)^2}\left[p_2^2\alpha_1 + \frac{3}{2}\alpha_1\alpha_2\frac{I_1 I_2}{I_1 + I_2}\right]. \qquad \text{Equation 6-13}$$

Now, the total interaction energy is given by $w_T(h) = \frac{A}{r^{12}} + w_{intr}$, where $w_{intr}(h) = w_n + w_{vdw}$. Therefore,

$$w_T(h) = \frac{A}{r^{12}} + \frac{p_y C_{bg}(V_g - V_d)}{2\varepsilon\varepsilon_0} - \frac{\pi}{A_{uc}} \frac{1}{h^4} \frac{1}{(4\pi\varepsilon\varepsilon_0)^2} \left[p_2^2 \alpha_1 + \frac{3}{2} \alpha_1 \alpha_2 \frac{I_1 I_2}{I_1 + I_2} \right].$$

Equation 6-14

Now, we can estimate the interaction energy $w_{intr}(h) = w_n + w_{vdw}$ from the available values of dipole moment, polarizability, ionization energy [25-27] and the corresponding Dirac points of graphene-FETs which are documented in Table 1. For equilibrium distance, we approximate h values for chloroform, DMMP and DCB from literature [24,28,29], and assume similar values for dichloromethane, DMF and chlorobenzene respectively, to get some estimates. The obtained interaction energy contribution from electrostatic forces between a dipole and graphene and the van der Waal interaction are given in Table 2 along with the experimental binding energies measured in our study.

	Dipole moment p (D)	**Ionization energy, I (eV)**	**Polarizability (α, x10^{-24} cm^3)**	**Equilibrium distance (h, Å)**	**V_D (V)**
Chloroform	1.04	11.42	8.23	4	6.1
Dichloromethane	1.6	11.35	6.48	4	13.7
Chlorobenzene	1.54	9.07	12.3	3.3	12.9
Dichlorobenzene	2.5	9.07	14.17	3.3	13.7
DMMP	3.62	9.94	10	2.8	11.3
DMF	3.82	9.12	7.8	2.8	4.9
Graphene	0	9	0.9		

Table 1. Dipole moment, ionization energy and polarizability values for small molecules and graphene. Also, tabulated are the equilibrium distance of small molecules on graphene obtained from literature. The Dirac point for the devices under study are from $I - V_g$ characteristics taken for each device.

	Experimental binding energy, E_a (meV)	**Interaction energy $w_{intr}(h)$ (meV)**
Chloroform	223	140
Dichloromethane	195	124
Chlorobenzene	367	410
Dichlorobenzene	447	491
DMMP	734	684
DMF	657	547

Table 2. Experimental binding energy obtained from temperature dependence measurement in this work and the theoretical interaction energy based on $w_{intr}(h) = w_n + w_{vdw}$.

The contour plots for the experimental values and theoretical estimates are plotted in Figure 6-19 for comparison. We observe the same trend, however, one we must mention that the theoretical interaction energies obtained are an overestimation since we do not account for the quantum mechanical repulsive force term at potential energy minima.

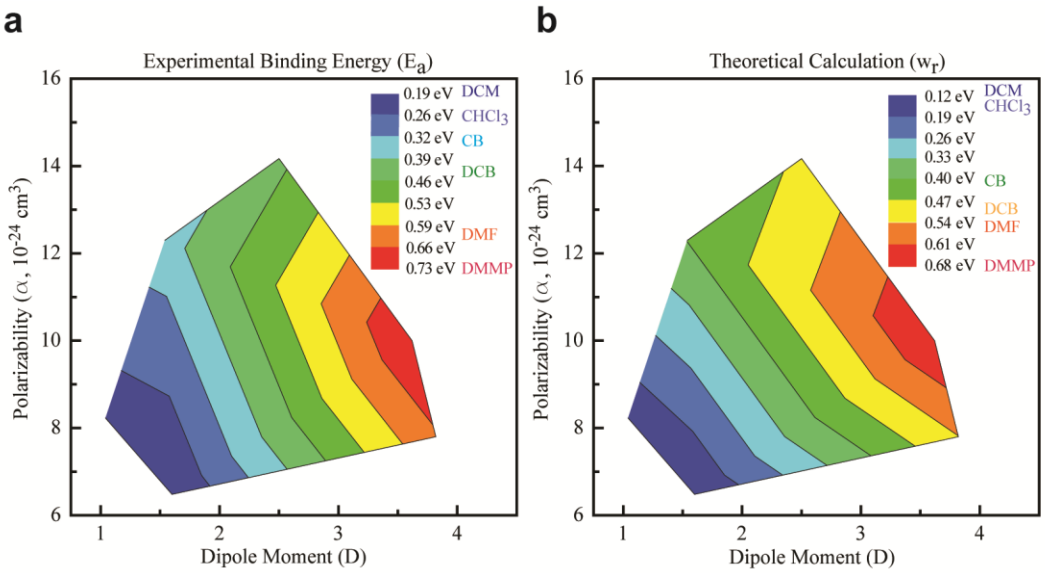

Figure 6-19. Contour plots of **(a)** experimental binding energy and **(b)** theoretical interaction energy from Table 2 plotted with dipole moment and polarizability of the molecules.

6.8 Conclusion

In this chapter, we demonstrated how heterodyne detection schematic provides a powerful tool to monitor molecular behavior near a nanomaterial surface in real-time. We experimentally calculated the binding energy of six different polar analytes on graphene by real-time heterodyne mixing analysis of temperature dependent desorption kinetics. Moreover, we demonstrated the electrical tuning of molecular interaction on graphene by back-gate modulation of graphene Fermi level. Further, we studied the temperature and electric field dependent behavior of aromatic compounds on graphene which highlights the complex nature of π-π interactions. The electric field tuning of interaction dynamics between small molecules and graphene adds another dimension to engineering chemical control-on-chip which has potential applications if diverse fields like biochemical recognition to catalysis.

Previous studies on molecular recognition on nanoelectronic systems have yielded inconclusive results because of their defect-dominated interaction mechanism. Such conventional charge-detection based techniques rely on binding of a molecule to defect sites leading to charge transfer, which is not representative of molecule-pristine graphene interaction especially considering the fact that the molecules under study are charge neutral. For example in ref [28], DMMP (electron donating) and DCB (electron withdrawing) molecules which also have different orientations with respect to graphene plane, show similar signal response trends with varying gate voltages. This can only be explained in terms of a defect-site desorption energy barrier. Similarly, in Ref. [30] high back gate voltage induced Dirac point shifts in the presence of ammonia molecules is attributed to dipole flipping of ammonia by the unscreened field. However, this picture is inconsistent with the ascribed orientation of ammonia molecule on top of

graphene in that work, hinting towards contribution of hysteretic behavior of substrate charge traps. In contrast, by relying on detecting molecular dipole induced conductance fluctuations in graphene as shown in the current work, both charge transfer and hysteretic processes can be avoided, facilitating the understanding and control of interaction between molecules and pristine graphene.

One of important focus areas for future work includes understanding the interaction of aromatic compounds on graphene in detail. The low temperature saturation in peak mixing currents and the lack of gate-dependent tuning can provide deep insight into π-π stacked systems. Here, the study of variety of substituted aromatic rings may help address some of the controversies in this field.

References

[1] E. Frieden, J. Chem. Educ. **52**, 754 (1975).

[2] P. Hobza and K. Müller-Dethlefs, *Non-covalent Interactions: Theory and Experiment* (The Royal Society of Chemistry, Cambridge, UK, 2010).

[3] M. Goyal, M. Rizzo, F. Schumacher, and C. F. Wong, J. Med. Chem. **52**, 5582 (2009).

[4] S. K. Burley and G. A. Petsko, Adv. Protein Chem. **39**, 125 (1988).

[5] J. M. Lehn, Angew. Chem.-Int. Edit. Engl. **29**, 1304 (1990).

[6] O. Ramstrom and J. M. Lehn, Nat. Rev. Drug Discov. **1**, 26 (2002).

[7] D. Strmcnik, K. Kodama, D. van der Vliet, J. Greeley, V. R. Stamenkovic, and N. M. Markovic, Nat. Chem. **1**, 466 (2009).

[8] W. Lu and C. M. Lieber, Nature Mater. **6**, 841 (2007).

[9] P. L. McEuen, Phys. World **13**, 31 (2000).

[10] A. K. Geim and K. S. Novoselov, Nature Mater. **6**, 183 (2007).

[11] Q. H. Wang, K. Kalantar-Zadeh, A. Kis, J. N. Coleman, and M. S. Strano, Nature Nanotechnol. **7**, 699 (2012).

[12] S. Das Sarma, S. Adam, E. H. Hwang, and E. Rossi, Reviews of Modern Physics **83**, 407 (2011).

[13] G. A. Somorjai, *Introduction to Surface Chemistry and Catalysis* (John Wiley and Sons, New York, 1994).

[14] N. Cardonamartinez and J. A. Dumesic, Advances in Catalysis **38**, 149 (1992).

[15] F. C. Tompkins, *Chemisorption of Gases on Metals* (Academic Press, London, 1978).

[16] P. Lazar, F. Karlicky, P. Jurecka, M. Kocman, E. Otyepkova, K. Safarova, and M. Otyepka, J. Am. Chem. Soc. **135**, 6372 (2013).

[17] J. Israelachvili, *Intermolecular and Surface Forces* (Academic Press, Waltham, MA, 2011), Third edn.

[18] D. E. Brown, S. M. George, C. Huang, E. K. L. Wong, K. B. Rider, R. S. Smith, and B. D. Kay, Journal of Physical Chemistry **100**, 4988 (1996).

[19] V. Georgakilas, M. Otyepka, A. B. Bourlinos, V. Chandra, N. Kim, K. C. Kemp, P. Hobza, R. Zboril, and K. S. Kim, Chem. Rev. **112**, 6156 (2012).

[20] C. A. Hunter and J. K. M. Sanders, J. Am. Chem. Soc. **112**, 5525 (1990).

[21] F. Cozzi, M. Cinquini, R. Annuziata, and J. S. Siegel, J. Am. Chem. Soc. **115**, 5330 (1993).

[22] S. E. Wheeler, J. Am. Chem. Soc. **133**, 10262 (2011).

[23] S. V. Garimella *et al.*, Ieee Transactions on Components and Packaging Technologies **31**, 801 (2008).

[24] Y.-H. Zhang, K.-G. Zhou, K.-F. Xie, H.-L. Zhang, Y. Peng, and C.-W. Wang, Physical Chemistry Chemical Physics **14**, 11626 (2012).

[25] W. Haynes, *CRC Handbook of Chemistry and Physics* (CRC Press, 2014), 95th Edition edn.

[26] F. A. Bulat, J. S. Burgess, B. R. Matis, J. W. Baldwin, L. Macaveiu, J. S. Murray, and P. Politzer, Journal of Physical Chemistry A **116**, 8644 (2012).

[27] http://www.dem.ri.gov/pubs/sops/wmsr2114.pdf

[28] B. Kumar *et al.*, Nano Letters **13**, 1962 (2013).

[29] J. Akesson, O. Sundborg, O. Wahlstrom, and E. Schroder, Journal of Chemical Physics **137** (2012).
[30] S. Chen, W. Cai, D. Chen, Y. Ren, X. Li, Y. Zhu, J. Kang, and R. S. Ruoff, New Journal of Physics **12** (2010).

Chapter 7

Conclusions and future work

7.1 Summary

In this work, we developed a fundamentally new sensing mechanism based on the principle of heterodyne mixing between charge density fluctuations in a nanoelectronic sensor caused by the oscillating dipole moment of an adsorbed molecule and an alternating current drive voltage which excites it, and demonstrated rapid and sensitive chemical and biological detection. By detecting molecular dipole instead of the associated charge, we address the limitations of conventional nanoelectronic detection techniques.

In particular, in chapter 4 we demonstrated for the first time biomolecular detection using carbon-nanotube heterodyne biosensors in physiologically relevant ionic strength solutions (~100mM), where conventional nanoelectronic sensors based on charge-detection mechanism fail due to the fundamental Debye screening effect. We demonstrate the detection of biotin-streptavidin ligand-receptor binding in 100 mM background ionic solution both in static and real-time flow conditions. Our results hold great promise for Point-of-Care (POC) nanoelectronic biosensors where detection needs to be carried out at patient site with limited sample processing capability.

In chapter 5, we applied the heterodyne sensing technique to demonstrate the first graphene heterodyne vapor sensors to achieve simultaneously rapid (~0.1 s) and

sensitive (~1 ppb) detection of a wide range of analytes, which is orders-of-magnitude better than state-of-art sensors. Conventional charge-detection based nanoelectronic vapor sensors suffer from slow response and recovery times of 10-100 seconds due to the slow dynamics of interface trapped states and defect-mediated charge-transfer processes. We demonstrated rapid and sensitive detection of 15 volatile organic compounds with a minimum detection limit of 0.64 ppb, which is the lowest for any pristine, uncoated nanoelectronic sensor. These results signify the ability to integrate graphene nanoelectronic heterodyne vapor sensors with on-field micro gas chromatography applications.

Finally, in chapter 6 we demonstrated how heterodyne detection can be used to study the rapid dynamics of molecule-graphene interaction. We quantified the non-covalent binding interactions of six polar molecules on a graphene FET in real-time by analyzing the heterodyne signal during molecular desorption process. More importantly, we demonstrated for the first time, electrical tuning of molecule-graphene binding kinetics by electrostatic control of graphene work function. Moreover, we studied the interaction of aromatic chlorobenzenes with graphene, revealing the complex interplay between dispersive and electrostatic Coulombic forces in π-π systems. These results point towards the ability to electrically tailor chemical interactions, which can help rational design of complex chemical processes for example in drug discovery and catalysis.

In conclusion, we proved heterodyne sensing is a versatile technology which is platform independent and can be implemented in liquid as well as gas phase. This technology can be extended to other nanoelectronic sensors based on nanowires and

metal dichalcogenides as well. Our work not only lays a foundation on which the next generation of rapid and sensitive point-of-use biological and chemical sensors will be developed, but also provides an insight into the fundamental interaction between molecules and graphene at high frequencies.

7.2 Future work

Heterodyne detection has great potential for applications both in fundamental science as well as technological advancement. Based on the work presented in this thesis, one of the most promising avenues of future work is integrating graphene nanoelectronic heterodyne sensors with micro gas chromatography components in order to replace the bulky flame-ionization-detector (FID). Applications like occupational and industrial safety require rapid and robust sensors which are light to carry around e.g. in oil and gas exploration, chemical industry etc. Moreover, graphene is an ideal material for this application because it can be synthesized on wafer-scale, is fully compatible with existing top-down fabrication technology and can be integrated with on-chip electronic circuitry to achieve badge-sized wearable sensors. Related to this application, an aspect of future work is to extend heterodyne sensors to detect non-polar molecules (zero dipole moment). One idea which can be explored is to functionalize the graphene surface with nanoparticles which interact with non-polar molecules to affect the heterodyne signal.

Another direction for future study is pushing the detection limits of heterodyne vapor sensors to single-molecule levels. Based on our results, this can be easily achieved by scaling down the graphene channel or by using carbon nanotube as the channel material. For example, the minimum detection limit for our graphene FET is ~ 10^4 molecules (chapter 5) and by replacing graphene (W = 1μm) with nanotube (1nm

diameter), we can achieve detection limits ~ 10s of molecules. Moreover, the ability to completely shut-off the channel in semiconducting nanotubes can provide extremely high sensitivities. This can open up a door to study individual molecular events with unprecedented precision which is both scientifically and technologically important.

On the fundamental side, an important focus area includes understanding the interaction of aromatic compounds and graphene. A detailed study of low temperature saturation observed in peak mixing currents for aromatic compounds and the lack of gate-dependent tuning in them can provide deep insight into π-π stacked systems. Here, a systematic study of substituted aromatic rings may help address some of the controversies in this field also. For example, by choosing benzene ring substituted with electron-withdrawing (-Cl, -NO_2) or electron-donating (-NH_2) groups, we can analyze how the substitution affects the interaction with graphene. Theoretically, an electron-donating group should increase the π-electron density and should lead to more repulsion. Similarly, multiple substituents can significantly enhance this effect. Can this make graphene insensitive to some substituted benzenes? How does low temperature affect this interaction with multi-substituted benzene? On the other hand, another question arises - can benzene multi-substituted with electron withdrawing groups lead to a change in the stacking on graphene from parallel-offset to sandwich structure, and whether this is reflected in the heterodyne mixing signal? All these are exciting avenues for further exploration since understanding π-π interactions is extremely important as they are not only the basis of most biological and cellular processes but also are part of pharmaceutical endeavors in drug discovery.

Appendices

Appendix A

Single walled carbon nanotube growth conditions

Carbon nanotube growth is carried out in First Nano EasyTube 3000 in two phases – anneal and growth. We have noticed that any photoresist residue left behind after the first lithography step of depositing Fe particles hampers nanotube growth. Hence, we carry out an anneal step in air at 880 °C for one hour to remove photoresist residue (Figure Ia). For nanotube growth, multiple samples are placed downstream (Figure Ic) and the chamber is purged with Argon for 5 min at 3 SLM (standard liter per minute). Then, a flow of 1 SLM of argon is maintained while the furnace is ramped up to 800 °C. In the next step, a flow of 0.2 SLM of hydrogen is maintained for 5 min to reduce the catalyst particles i.e. convert iron oxide to iron and then ethylene (C_2H_4) is introduced for 35 min to grow SWNTs. C_2H_4 flow is kept at 5.5 sccm (standard cubic centimeter per minute) of ethylene (C_2H_4) while maintaining a H_2 flow of 0.2 SLM throughout the growth process. The length of SWNTs obtained from this recipe is > 20 micron (μm). Then, the furnace is allowed to cool down to room temperature in a small argon flow. The growth phase is described in Figure Ib.

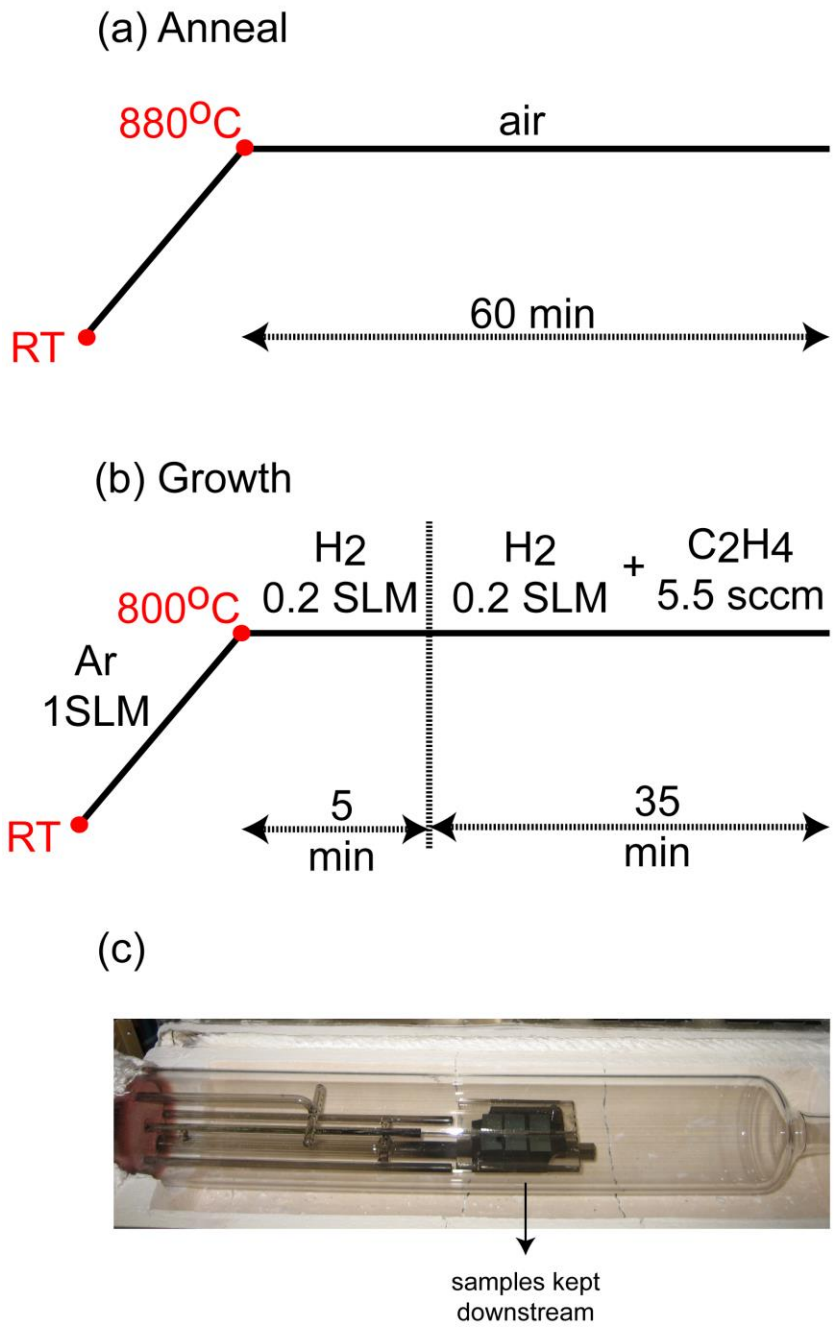

Figure I Carbon Nanotube growth. (a) Anneal step to remove photoresist residue, (b) growth step for CNT growth and (c) device placement in growth furnace.

Appendix B

Single layer graphene growth

First, 25μm thick copper foil (99.8%, Alfa Aesar) was loaded into an inner quartz tube inside a 3 inch horizontal tube furnace of a commercial CVD system (First Nano EasyTube 3000). The system was purged with argon gas and evacuated to a vacuum of 0.1 Torr. The sample was then heated to 1000°C in H_2 (100 sccm) environment with vacuum level of 0.35 Torr. When 1000°C is reached, 70 sccm of CH_4 is flowed for 15 minutes at vacuum level of 0.45 Torr. The sample is then cooled slowly to room temperature with a feedback loop to control the cooling rate. The vacuum level is maintained at 0.5 Torr with 100 sccm of argon flowing.

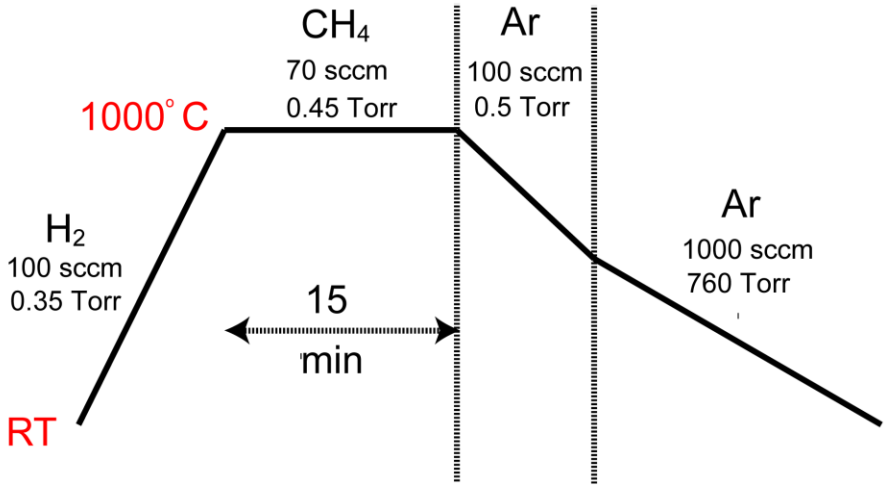

Figure I. Single layer graphene growth process flow.

Appendix C

DMMP low mass injection

The minimum quantity of liquid that can be injected using a GC syringe is 5nL, which amounts to 579pg of DMMP with a split of 10000. In order to inject lower quantities, we use a mixture of acetone and DMMP. Both being polar solvents, have a decent solubility, however to accurately determine the amount of DMMP in the mixture we use area under curve of FID response of 5nL injection of 1:1 acetone: DMMP and 5nL DMMP (579pg).

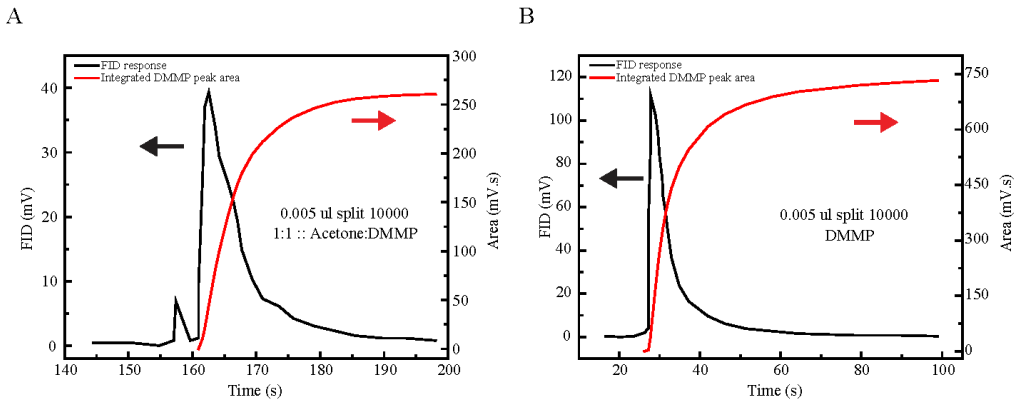

Figure I. Estimation of injected mass from the area under FID response curves. **(A)** FID response for 5 nL injection of 1:1 Acetone: DMMP mixture (black) and integrated area under the DMMP response (red). First peak in FID response corresponds to acetone and second peak corresponds to DMMP. **(B)** FID response for 5 nL (579 pg) injection of DMMP (red) and integrated area under the DMMP response (red).

A ratio of the area under DMMP response curves yields that the injected DMMP amount in Figure I-A is 205pg.

Appendix D

Estimating concentration of injected analytes

To measure the concentration equivalents of the injected mass for any given analyte we use the full-width-half-maximum ($\tau_{1/2}$), flow rate of carrier gas, analyte molar mass and density.

Measured helium flow rate = 8 ml/min

Amount of helium which flows over the device in $\tau_{1/2}$ seconds = $(8\tau_{1/2})/60$ mL

Now, we know that 24 Liters = 1mole at room temperature and standard pressure. Therefore, number of moles of Helium which pass over the device in $\tau_{1/2}$ seconds

$$= \frac{8\tau_{1/2}}{60} \times 10^{-3} \times \frac{1}{24} = 5.56 \times 10^{-6} \times \tau_{1/2} \text{ moles}$$

If the volume of analyte injected is x μL and density of analyte is ρ kg/m^3 (ρ µg/uL) then, amount of injected analyte = $x\rho$ μg = $\frac{x\rho \times 10^{-6}}{M}$ moles where M is molar mass of analyte in g/mol. Assuming, the entire quantity of injected analyte contributes to mixing current signal, then concentration of analyte on top of device is the ratio of moles of injected analyte to moles of helium which flows over the device in time, $\tau_{1/2}$.

Hence, analyte concentration is $c = \frac{\frac{x\rho \times 10^{-6}}{M}}{5.56 \times 10^{-6} \times \tau_{1/2}} \times 10^6 = \frac{x\rho}{5.56 M \tau_{1/2}} \times 10^6$ ppm.

Appendix E

Calculation of noise floor

In order to determine the minimum detection limit (MDL) of our sensors, we need to define the noise floor. We use the 3σ noise floor as our MDL value. For the device measured in Chapter 4, a time sweep capture during the measurement is show in Figure I. The calculated standard deviation is 42 pA, thereby defining our noise floor as 120 pA.

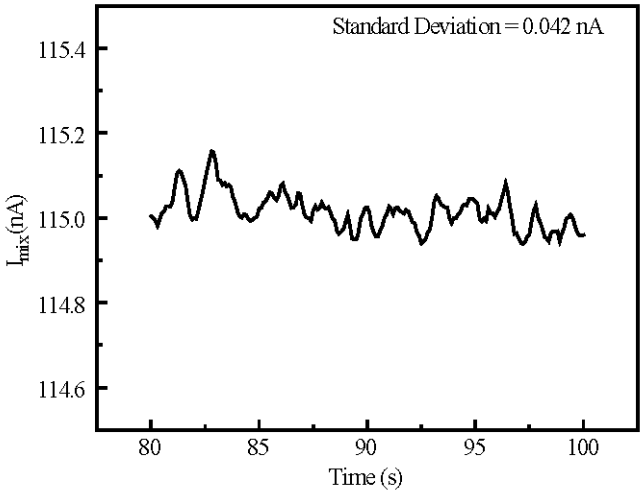

Figure I. Baseline mixing current sweep over a time period of 20 sec chosen randomly.

Appendix F

Graphene heterodyne sensor output dependence on drive voltage

The current-voltage relation in a graphene transistor discussed in chapter 3, reveals that frequency mixing terms can be obtained by (i) non-linearity associated with gate response and (ii) mixing of oscillating dipole field induced charge density modulation and the source drive. With a common ground for the source and gate, any excitation at the source is equivalent to an excitation at the gate, though with an opposite sign. We study the dependence of graphene mixer output on AC drive voltage in the presence of analytes. Figure I shows the dependence of baseline mixing current on drive voltage for pulsed injections of chloroform and ethanol. Clearly we can observe, that as the drive voltage increases not only the baseline mixing current increases, the mixing response to chloroform and ethanol also increases. These are further highlighted in Figure IIa, where we can see that the baseline I_{mix} has a quadratic dependence as expected and noise has a linear dependence. The mixing current change, ΔI_{mix} for presence of analytes is a linear function of the drive voltage, $v_{ac} = \tilde{V}^{\omega}$ as seen in chapter 5 (Figure IIb). In our study, we generally apply v_{ac} between 10-30 mV. Interestingly, both the signal response ΔI_{mix} and noise go as linear functions of v_{ac}, which illustrates the need to have a very clean and low noise device for achieving high sensitivity detection, rather than pushing for high drive in voltages.

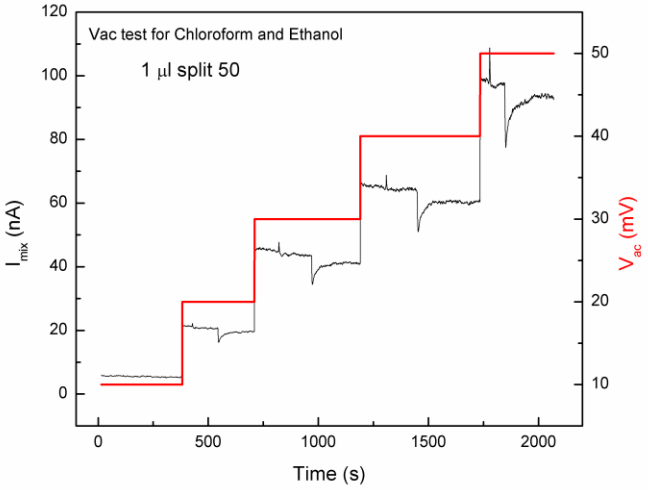

Figure I. Mixing current dependence of graphene FET on drive voltage $v_{ac} = \tilde{V}^{\omega}$. Along with baseline mixing current, we also monitor the response signal for chloroform (increase) and ethanol (fall).

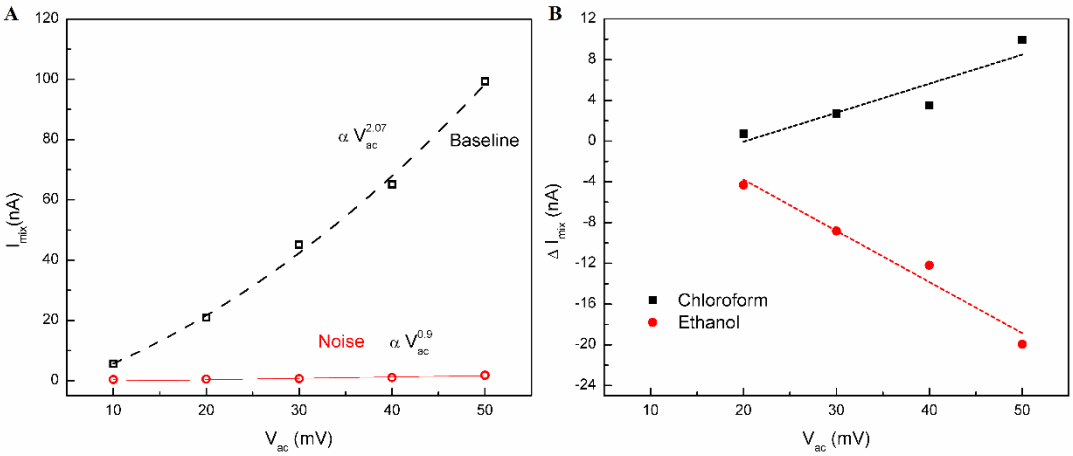

Figure II. (a) Baseline mixing current (□) and noise dependence (○) on drive voltage extracted from Figure I. The curves are fit using power function. (c) ΔI_{mix} for chloroform (■) and ethanol (●) at different drive voltage from Figure I, with corresponding linear fits.